

# Aeroacoustic Analysis of the SOFIA Telescope Cavity by Means of Flight Test Data

Study Thesis  
by  
cand. aer. Artem Seidenberg

*realized at the*  
Institut für Aerodynamik und Gasdynamik  
der Universität Stuttgart  
*and the subsidiary of the*  
Deutsches SOFIA Institut  
der Universität Stuttgart  
*at the*  
NASA Dryden Flight Research Center,  
Palmdale, California

Stuttgart, April 2011



# Abstract

The Stratospheric Observatory for Infrared Astronomy (SOFIA) is a joint project of the National Aeronautics and Space Administration (NASA) and the German Aerospace Center (DLR) in order to study the universe in the infrared spectrum. Being the largest airborne observatory in the world it consists of a modified Boeing 747SP operating at and above an altitude of 12 km. In particular, a 2.7 m reflecting telescope is integrated in a closable cavity in the rear part of the aircraft body. Once the cavity door is opened for skywatching during operational flights, the telescope is exposed to the free atmosphere and thus to flow-induced vibrations and acoustic fluctuations, which can impact its pointing stability and image quality.

The goal of this study thesis was to analyze the aeroacoustic behavior of the SOFIA telescope cavity by means of available flight test data. Therefore, an optimized postprocessing procedure with powerful graphical capabilities has been implemented in order to interpret the test results qualitatively and quantitatively as well as to compare them with previous theoretical findings and numerical simulations. In this way, this analysis provides further important insights as well as a deeper understanding of critical aeroacoustic behavior of the SOFIA configuration and thus contributes to the interdisciplinary telescope pointing optimization.

# Kurzfassung

Das Stratosphärenobservatorium für Infrarotastronomie (SOFIA) ist ein Gemeinschaftsprojekt der National Aeronautics and Space Administration (NASA) sowie des Deutschen Zentrums für Luft- und Raumfahrt (DLR) mit dem Ziel, das Universum im infraroten Lichtspektrum zu erforschen. Es ist die weltgrößte fliegende Sternwarte und besteht aus einer modifizierten Boeing 747SP, die in oder oberhalb von 12 km Höhe betrieben wird. Dabei ist im hinteren Rumpfsegment des Flugzeugs ein 2.7 m großes Spiegelteleskop in einem verschließbaren Schacht (Cavity) integriert. Sobald die Cavity-Tür während des Flugbetriebs für Himmelsbeobachtungen geöffnet wird, ist das Teleskop der freien Atmosphäre und somit strömungsinduzierten Vibrationen und akustischen Schwankungen ausgesetzt, welche seine Positioniergenauigkeit sowie die Bildqualität erheblich beeinträchtigen können.

Das Ziel dieser Studienarbeit war es, das aeroakustische Verhalten des SOFIA-Teleskopschachts mit Hilfe von verfügbaren Flugversuchsdaten zu analysieren. Hierfür wurde eine optimierte Datenprozesskette mit leistungsfähigen grafischen Funktionalitäten implementiert, um die Versuchsergebnisse qualitativ sowie quantitativ auszuwerten und sie mit bisherigen theoretischen Erkenntnissen und numerischen Simulationen zu vergleichen. Damit bietet diese Untersuchung weitere wichtige Erkenntnisse sowie ein tieferes Verständnis des kritischen aeroakustischen Verhaltens der SOFIA-Konfiguration und trägt somit zur interdisziplinären Optimierung der Teleskop-Positioniergenauigkeit bei.



# Acknowledgments

This study thesis would not have been possible without the guidance, help and inspiration of several individuals who in one way or another assisted me and contributed to the preparation as well as the successful completion of this work.

First and foremost, I would like to express my utmost gratitude to Dr. Thorsten Lutz, whose initiative and support enabled me to participate in this exciting project. He has been a highly competent and pleasant advisor within and beyond the scope of this thesis. I am also very grateful to Professor Dr. Ewald Krämer, who endorsed my intention by readily assuming the responsibility for this thesis as my supervising professor and by supporting my applications for scholarships. I would especially like to thank my direct supervisor Christian Engfer, who continuously provided valuable advice and assistance during my research although being exposed to a high work load himself. He exhibited a sincere interest in the success of my work at all times.

I will always keep in fond memory the unconditional professional support by my cubicle neighbor Stefan Teufel and our sophisticated discussions. Moreover, I will never forget the unique helpfulness and warmhearted amicability of the former team member Karsten Bosse. I owe my gratitude to Ms. Nicole Lampa, who took care of my passport and visa concerns quickly and efficiently and Dr. Thomas Keilig, who actively supported my administrative and project-related issues. It is also a pleasure to thank the rest of the SOFIA team, who warmly welcomed and fostered me throughout my stay: Dr. Holger Jakob, Ulrich Lampater, Marco Lentini, Simon Beckmann, Alexander Korosek, Andreas Reinacher, Rainer Strecker, Josef Trendelkamp, Mathias Mößner, Nadine Hanisch, Benjamin Greiner, Sören Süße, Susanne Haußmann and many others from NASA, DLR, USRA and DSI.

I greatly appreciate the financial aid by the *Erich-Becker-Stiftung - Eine Stiftung der Fraport AG zur Förderung von Wissenschaft und Forschung*, which has been granted immediately and in an unbureaucratic way.

Last but not least, I would like to thank my family and friends for their affection and emotional support.



# Contents

<b>Abstract</b>	<b>iii</b>
<b>Acknowledgments</b>	<b>v</b>
<b>Contents</b>	<b>vii</b>
<b>List of Figures</b>	<b>ix</b>
<b>List of Tables</b>	<b>xi</b>
<b>Nomenclature</b>	<b>xiii</b>
<b>1. Introduction</b>	<b>1</b>
1.1. Stratospheric Observatory for Infrared Astronomy . . . . .	1
1.2. SOFIA Project Overview . . . . .	2
1.3. Thesis Objectives and Outline . . . . .	2
<b>2. Flight Test Arrangement</b>	<b>3</b>
2.1. Relevant sensors and geometry . . . . .	3
2.2. Basic functionality of the configuration . . . . .	6
<b>3. Flight Tests for Envelope Expansion</b>	<b>7</b>
<b>4. Flight Test Data</b>	<b>9</b>
4.1. Test Data Acquisition . . . . .	9
4.2. Test Data Postprocessing . . . . .	10
4.3. SOFIA Acoustic Data Analyzer . . . . .	12
<b>5. Theoretical Background</b>	<b>15</b>
5.1. Acoustics . . . . .	15
5.2. Cavity Flow and Aeroacoustics . . . . .	16
5.2.1. Open and Closed Cavity Flow . . . . .	16
5.2.2. Feedback Process in Shear Layer Mode . . . . .	17
5.2.3. Cavity Modes and Acoustic Resonance . . . . .	18
5.3. Digital Signal Processing . . . . .	19
5.3.1. Discrete FOURIER Transform . . . . .	19
5.3.2. Power Spectral Density and WELCH's method . . . . .	19
<b>6. Flight Test Data Analysis</b>	<b>21</b>
6.1. Data Analysis Approach . . . . .	21
6.2. Telescope Assembly Aeroacoustics . . . . .	25
6.2.1. Critical Aperture Assembly Position . . . . .	25

6.2.2. Critical Telescope Assembly Spots . . . . .	26
6.3. Aeroacoustic Parameter Study . . . . .	33
6.3.1. Aperture Exposure Effect . . . . .	34
6.3.2. MACH Number Effect on Characteristic Frequencies . . . . .	41
6.3.3. Regression Analysis of Aeroacoustic Pressure Fluctuations . . . . .	42
6.4. Cavity Aeroacoustics . . . . .	48
<b>7. Summary</b>	<b>51</b>
7.1. Postprocessing Procedure Optimization . . . . .	51
7.2. Aeroacoustic Data Analysis . . . . .	51
<b>Bibliography</b>	<b>53</b>
<b>A. Operating Guidelines for the SOFIA Acoustic Data Analyzer</b>	<b>55</b>
A.1. Advanced GUI Functions . . . . .	55
A.1.1. Plot Matrix Panel . . . . .	55
A.1.2. 3D Geometry Specifications Panel . . . . .	57
A.2. Working Directory File System . . . . .	58
A.3. Internal SADA File System . . . . .	59
A.3.1. SADA Input Folder . . . . .	60
A.3.2. SADA Preparation Folder . . . . .	62
<b>B. Aeroacoustic Analysis Properties</b>	<b>65</b>
B.1. SADA Sessions Overview . . . . .	65
B.2. Pressure Sensors Overview . . . . .	67
<b>C. Additional Aeroacoustic Analysis Plots</b>	<b>83</b>



# List of Figures

1.1. SOFIA's first test flight with fully opened door. . . . .	1
2.1. SOFIA aircraft configuration. . . . .	3
2.2. SOFIA cavity components. . . . .	4
2.3. SOFIA telescope components. . . . .	5
2.4. Rotary parts of the SOFIA configuration. . . . .	6
3.1. SOFIA flight envelope and relevant test points. . . . .	8
4.1. Flow chart of the conventional postprocessing procedure. . . . .	11
4.2. Flow chart of the enhanced postprocessing procedure. . . . .	13
4.3. Screenshot of the reworked SOFIA Acoustic Data Analyzer GUI. . . . .	14
5.1. Scheme of the open and closed cavity flow. . . . .	16
5.2. Scheme of the feedback process during open cavity flow. . . . .	17
5.3. Coupling between ROSSITER modes and depth-wise acoustic cavity modes. . . . .	18
6.1. Selection of time windows for the aeroacoustic analysis. . . . .	23
6.2. PSD( $f$ ) plot of the telescope average for different aperture positions in baseline configuration. . . . .	25
6.3. SPL bar chart of telescope sensors for different aperture positions in baseline configuration. . . . .	27
6.4. Telescope Assembly hot spots overview for baseline configuration. . . . .	28
6.5. Telescope Assembly CFD simulation results, revealing an asymmetrical flow downwash. . . . .	28
6.6. PSD( $f$ ) plot of hot spot sensors, featuring broadband and narrowband characteristic in baseline configuration. . . . .	29
6.7. SPL bar chart of telescope hot spots for different aperture positions in baseline configuration. . . . .	31
6.8. SPL bar chart of telescope hot spots for selected operational points. . . . .	31
6.9. Selected operational points of SOFIA during a science mission. . . . .	32
6.10. SPL bar chart of the averages of all sensor groups for different aperture exposures. . . . .	34
6.11. SPL bar chart of telescope hot spots for different aperture exposures. . . . .	35
6.12. SPL bar chart of cavity hot spots for different aperture exposures. . . . .	35
6.13. SPL contour plot of the cavity for different aperture exposures. . . . .	36
6.14. PSD( $f$ ) plot of the cavity aft bulkhead sensor PA8412 for different aperture exposures. . . . .	37
6.15. SPL bar chart of the TA sensors average for different aperture exposures. . . . .	38
6.16. SPL frequency spectra of all TA sensors for different aperture exposures. . . . .	40
6.17. PSD( $f$ ) plot of the cavity aft bulkhead microphone PA8583M for the altitude $h = 35\,000$ ft and different MACH numbers. . . . .	41
6.18. Comparison of the first four ROSSITER modes with observed peak frequencies of the microphone PA8583M for $h = 35\,000$ ft and different MACH numbers. . . . .	42

6.19. Scheme of the black box method. . . . .	43
6.20. Test point matrix of the regression analysis for $\gamma_{AA} = 40^\circ$ . . . . .	44
6.21. Effect function $p_{rms}(Ma_\infty, q_\infty, e_{AA} = 96.3\%)$ for selected response variables compared to measured flight test points. . . . .	46
6.22. PSD( $f$ ) plot of the average of narrowband cavity sensors. . . . .	48
6.23. Comparison of $c_{p,rms}$ contour plots derived from CFD simulations and flight tests for two observed acoustic peaks. . . . .	49
A.1. Screenshot of the reworked SOFIA Acoustic Data Analyzer workspace window. . . . .	56
A.2. Folder hierarchy in the SADA working directory. . . . .	58
A.3. Internal SADA file system. . . . .	59
B.1. Pressure sensor locations on the Telescope Assembly. . . . .	73
B.2. Pressure sensor locations on the cavity surface. . . . .	77
B.3. Pressure sensor locations on the Aperture Ramp and Sidewalls. . . . .	80
B.4. Pressure sensor locations on the Lower Flexible Door. . . . .	81
B.5. Pressure sensor locations on the Upper Rigid Door. . . . .	82
C.1. Comparison of the aperture exposures $e_{AA} = 95^\circ$ and $e_{AA} = 100^\circ$ for the TA hot spots in baseline configuration. . . . .	83
C.2. SPL plot of telescope sensor group averages for different aperture positions in baseline configuration. . . . .	84
C.3. PSD plot of hot spot sensors, featuring different spectral characteristics in baseline configuration. . . . .	85
C.4. Overview of cavity hot spots for baseline configuration. . . . .	87
C.5. Contour plot of $c_{p,rms}$ on the cavity surface for two observed acoustic peaks. . . . .	88

# List of Tables

4.1. Relevant global variables . . . . .	10
6.1. SADA plot types and nomenclature. . . . .	24
6.2. Regarded aperture exposures in CFD simulations and flight tests. . . . .	38
6.3. Solution of the regression model. . . . .	45
6.4. Verification of the regression formula. . . . .	45
A.1. Control variables in the <code>input.xlsx</code> file of SADA. . . . .	60
A.2. Sensor properties in the <code>senspos.xlsx</code> file of SADA. . . . .	63
B.1. SADA Session List. . . . .	65
B.2. Pressure Sensor List . . . . .	67



# Nomenclature

In the following, the units corresponding to the Greek and Roman symbols reflect the respective dimensions of the scalar, vector or matrix variables. Unit-free variables or variable components are denoted by the symbol “-”.

## Acronyms

Symbol	Meaning	
A/D	Analog-to-digital converter	p. 5
AA	Aperture Assembly	p. 6
AFB	(Edwards) Air Force Base	p. 3
ALP	Angle of Attack ( $\alpha$ ) (session nomenclature abbreviation)	p. 24
ALT	Flight Altitude ( $h$ ) (session nomenclature abbreviation)	p. 24
ARC	NASA Ames Research Center	p. 2
ASCII	American Standard Code for Information Interchange (file format)	p. 10
BET	Sideslip Angle ( $\beta$ ) (session nomenclature abbreviation)	p. 24
CAA	Computational Aeroacoustics	p. 18
CFD	Computational Fluid Dynamics	p. 2
CMP4	Compressed 4 (file format)	p. 9
CSV	Comma-Separated Values (file format)	p. 11
DAOF	NASA Dryden Aircraft Operations Facility	p. 2
DFRC	NASA Dryden Flight Research Center	p. 2
DFT	Discrete FOURIER Transform	p. 19
DLR	Deutsches Zentrum für Luft- und Raumfahrt (German Aerospace Center)	p. 1
DSI	Deutsches SOFIA Institut (German SOFIA Institute)	p. 2
DSP	Digital Signal Processing	p. 19
EL	Elevation, elevation axis	p. 6
EXP	Aperture Exposure ( $e_{AA}$ ) (session nomenclature abbreviation)	p. 24
FAA	Federal Aviation Administration	p. 7
FL	Flap Deflection ( $d_{fl}$ ) (session nomenclature abbreviation)	p. 24
FLT	Flight (session nomenclature abbreviation)	p. 24
GUI	Graphical User Interface	p. 10

IAG	Institut für Aerodynamik und Gasdynamik (Institute for Aerodynamics and Gas Dynamics)	p. 2
ID	Identifier	p. 10
IR	Infrared	p. 1
ISA	International Standard Atmosphere	p. 43
KCAS	Knots Calibrated Airspeed	p. 8
LFD	Lower Flexible Door	p. 6
LOS	Line of Sight, line-of-sight axis	p. 6
MA	MACH Number ( $Ma$ ) (session nomenclature abbreviation)	p. 24
MAT	MATLAB <sup>®</sup> file format	p. 12
MCC	Mission Control Center	p. 3
n/a	not available	p. 67
NASA	National Aeronautics and Space Administration	p. 1
PM	Primary Mirror	p. 5
PMA	Primary Mirror Assembly	p. 5
PSD	Power Spectral Density	p. 19
PUPPO	Pull-Up-Push-Over (maneuver)	p. 7
PY	Python <sup>®</sup> data format	p. 10
RGB	Red-Green-Blue Color Model	p. 61
RMS	Root Mean Square	p. 15
SADA	SOFIA Acoustic Data Analyzer	p. 9
SM	Secondary Mirror	p. 5
SMM	Secondary Mirror Mechanism	p. 5
SOFIA	Stratospheric Observatory for Infrared Astronomy	p. 1
SPL	Sound pressure level	p. 5
SSC	SOFIA Science Center	p. 2
TA	Telescope Assembly	p. 2
TC	Test Card (session nomenclature abbreviation)	p. 24
URD	Upper Rigid Door	p. 6
USRA	Universities Space Research Association	p. 2
VER	SADA Session Version (session nomenclature abbreviation)	p. 24
XEL	Cross-Elevation, cross-elevation axis	p. 6
XLS, XLSX	Microsoft Excel <sup>®</sup> file format	p. 11

## Greek Symbols

Symbol	Unit	Meaning	
$\alpha$	[°]	Angle of attack	p. 7
$\beta$	[°]	Sideslip angle	p. 7
$\boldsymbol{\beta}$	[- ... -]	Vector of regression coefficients	p. 44
$\gamma$	[-]	Dimensionless phase shift of disturbances at cavity back wall	p. 17
$\gamma_{AA}$	[°]	Aperture Assembly elevation angle	p. 6
$\gamma_{TA}$	[°]	Telescope Assembly elevation angle	p. 6
$\Delta t$	[s]	Time interval	p. 15
$\Delta t_p$	[s]	Overall time window length for data analysis	p. 21
$\Delta t_{SPL}$	[s]	Time segment length for SPL calculation	p. 22
$\Delta t_{ts}$	[s]	Time window of trimmed flight (trim shot)	p. 22
$\epsilon$	[Pa ... Pa] <sup>T</sup>	Vector of residuals in the regression approach	p. 45
$\rho$	[m <sup>3</sup> /kg]	Static air density	p. 15
$\chi_{TA}$	[°]	Telescope Assembly cross-elevation angle	p. 10

## Roman Symbols

Symbol	Unit	Meaning	
$A$	[Pa]	Complex FOURIER coefficient (related to pressure signal)	p. 19
$a$	[psi], [Pa]	Sample of pressure signal	p. 19
$c$	[m/s]	Speed of sound	p. 34
$c_p$	[-]	Pressure coefficient	p. 20
$D$	[m]	Cavity depth	p. 16
$d_{fl}$	[°]	Flap deflection	p. 7
$e_{AA}$	[%]	Aperture exposure	p. 6
$f$	[Hz]	Frequency of a signal	p. 15
$f_{e,g}$	[Hz]	Sample extraction rate of global parameters	p. 23
$f_{Ross}$	[Hz]	Characteristic excitation frequency	p. 17
$f_{s,g}$	[Hz]	Sampling rate of a global parameter signal	p. 9
$f_{s,p}$	[Hz]	Sampling rate of a pressure sensor signal	p. 3
$h$	[ft]	Flight altitude	p. 7
$i = \sqrt{-1}$	[-]	Imaginary unit	p. 19
$j$	[-]	Index of sample in the time domain	p. 19
$K$	[-]	Ratio of disturbance convection velocity in the shear layer and free stream velocity ( $U_c/U_\infty$ )	p. 17

$k$	[-]	Index of complex FOURIER coefficient $A$	p. 19
$L$	[m]	Cavity length	p. 16
$L_p$	[dB]	Sound pressure level	p. 15
$m$	[-]	Mode number of periodic excitation	p. 17
$Ma$	[-]	MACH number	p. 7
$N$	[-]	Number of samples in a time window	p. 19
$n_x, n_y, n_z$	[-]	Mode numbers in corresponding axial directions $x, y, z$	p. 18
$\mathbf{p}$	[Pa ... Pa] <sup>T</sup>	Vector of output values in the regression approach	p. 45
$p$	[psi], [Pa]	Static air pressure	p. 15
$p_{ref}$	[Pa]	Threshold of human hearing at a frequency of 1000 Hz (reference root mean square value)	p. 15
$q$	[psf]	Dynamic pressure	p. 10
$\mathbf{r}$	[m m m] <sup>T</sup>	Position vector	p. 15
$R$	[-]	Number of WELCH blocks (time window segments)	p. 19
$Re$	[-]	REYNOLDS number	p. 16
$S$	[-]	Number of points in WELCH block (WELCH block length)	p. 19
$St$	[-]	STROUHAL number	p. 17
$t$	[s]	Time	p. 15
$t_{end,g}$	[s]	Upper limit of the global time window length	p. 65
$t_{end,p}$	[s]	Upper limit of the data analysis time window length ( $\Delta t_p$ )	p. 65
$t_{start,g}$	[s]	Lower limit of the global time window length	p. 65
$t_{start,p}$	[s]	Lower limit of the data analysis time window length ( $\Delta t_p$ )	p. 65
$U$	[m/s]	Airspeed	p. 7
$U_{KCAS}$	[kts]	Knots calibrated airspeed	p. 10
$U_c$	[m/s]	Convection velocity of disturbances in the shear layer	p. 17
$\mathbf{v}$	[m/s m/s m/s] <sup>T</sup>	Particle velocity vector	p. 15
$v_b$	[%]	WELCH block overlap	p. 19
$W$	[m]	Cavity width	p. 18
$w$	[-]	Window function for PSD analysis	p. 19
$(x, y, z)_{abs}$	[mm mm mm]	Absolute coordinate system of the SOFIA configuration	p. 67
$(x, y, z)_{rel}$	[mm mm mm]	Relative coordinate system of the SOFIA configuration	p. 67
$(x, y, z)$	[m m m]	Generic CARTESIAN coordinate system	p. 18



---

$\mathbf{X}$	$\begin{bmatrix} - & \cdots & \text{psf} \cdot \% \\ \vdots & \ddots & \vdots \\ - & \cdots & \text{psf} \cdot \% \end{bmatrix}$	Design matrix in the regression approach	p. 45
$\mathbf{x}$	$[- \cdots \text{psf} \cdot \%]$	Vector of predictor functions in the regression approach	p. 44

## Subscripts

Symbol	Meaning	
$\infty$	State at infinity, related to the undisturbed oncoming flow (free stream)	p. 7
0	Ambient value	p. 15
$i$	Index of response variables in the regression approach	p. 44
$rms$	Root mean square value	p. 15
$t$	Total/Stagnation value	p. 10

## Superscripts and Diacritics

Symbol	Meaning	
$\sim$	Deviation value	p. 15
T	Transpose vector/matrix	p. 44



# 1. Introduction

## 1.1. Stratospheric Observatory for Infrared Astronomy

Numerous astronomical objects like comets and planets in our solar system, but also extrasolar stars and far away galaxies predominantly emit light in the infrared spectrum (IR). Therefore, infrared astronomy provides a unique insight into the nature and phenomena of outer space which cannot be gained by means of visible light. However, Earth's atmosphere absorbs a big part of cosmic infrared radiation mainly due to water vapor, carbon dioxide and ozone. For this reason, observatories operating in this frequency range need to be located in very dry places at high altitudes. Besides the possibilities to install IR telescopes on high mountains (e.g. the *W. M. Keck Observatory* on Mauna Kea in Hawaii) or to put them in orbit (e.g. the *Herschel Space Observatory*), there is an option to integrate them into airborne observatories, which offers a very good compromise between the astronomical potential and the cost per utilizable photon [8, 12].



**Figure 1.1.:** SOFIA during its first test flight with fully opened door, December 2009.

© NASA Dryden

A prominent exemplar of the latter is the *Stratospheric Observatory for Infrared Astronomy (SOFIA)*, a joint project of the *National Aeronautics and Space Administration (NASA)* and the *Deutsches Zentrum für Luft- und Raumfahrt (German Aerospace Center, DLR)*. It consists of a modified Boeing 747SP accommodating a 2.7 m reflecting telescope in a closable cavity inside the rear section of the aircraft fuselage [8, 25] (see [Figure 1.1](#)).

## 1.2. SOFIA Project Overview

While the *Universities Space Research Association (USRA)* has developed and now operates the *SOFIA Science Center (SSC)* together with the *Deutsches SOFIA Institut (German SOFIA Institute, DSI)* at the *NASA Ames Research Center (ARC)* in Moffett Field, California, the SOFIA aircraft itself is located at the *NASA Dryden Aircraft Operations Facility (DAOF)* in Palmdale, California, which is a subsidiary of the *NASA Dryden Flight Research Center (DFRC)*. The DFRC is in charge of aircraft systems and flight operations, whereas the DSI maintains the SOFIA Telescope Assembly (TA) and manages its scientific operation [8]. The TA has been designed and built by a German consortium consisting of *Kayser-Threde GmbH* and *MAN Technologie AG* on behalf of the DLR [11].

Beyond its initial astronomical commitment SOFIA poses a wide range of big challenges in several disciplines of engineering, e. g. structural dynamics, control engineering, aerodynamics and aeroacoustics. The major common goal is to minimize disruptive effects of aircraft vibrations and flow-induced wind loads on the telescope structure, which is approached by close collaboration between experts of the respective scientific fields [10].

This study thesis constitutes a contribution to the research of the SOFIA aeroacoustic team on behalf of the DSI in cooperation with the *Institut für Aerodynamik und Gasdynamik der Universität Stuttgart (Institute for Aerodynamics and Gas Dynamics at the University of Stuttgart, IAG)*.

## 1.3. Thesis Objectives and Outline

During astronomic missions SOFIA operates at and above the altitude of 12 km with a fully opened cavity door. In case the door mechanism fails, the aircraft might be obliged to traverse also lower altitudes and land with a fully or partly opened door. In both scenarios the telescope is exposed to the free atmosphere. The highly transient flow over the cavity is known to cause acoustic fluctuations inside the opened port. Under unfavorable circumstances the characteristic frequencies of these fluctuations can match and excite TA structural modes having a significant impact on the telescope pointing stability as well as the quality of the final astronomical images [22].

Addressing this challenging problem former DSI member Dr. Sven Schmid studied the physical mechanisms of cavity flow and performed extensive numerical simulations of the flow field around the SOFIA configuration by means of *Computational Fluid Dynamics (CFD)* within the scope of a doctorate. In his substantial work [22] he has revealed informative findings and made predictions regarding the cavity aeroacoustics to be expected during open door flights.

The purpose of this study thesis is to analyze and evaluate the aeroacoustic behaviour of the real SOFIA telescope cavity based on flight test measurements and thus to validate major statements and predictions by Schmid [22] drawing own conclusions.

After introducing the SOFIA configuration and instrumentation in [Chapter 2](#) (p. 3 ff.), the performed flight tests are discussed in [Chapter 3](#) (p. 7 ff.). Thereafter, [Chapter 4](#) (p. 9 ff.) addresses the data acquisition and postprocessing procedure, which has been comprehensively improved by the author as the first core task of this thesis. Subsequently, essential theoretical aspects are highlighted in [Chapter 5](#) (p. 15 ff.) in order to prepare the reader for the aeroacoustic data analysis in [Chapter 6](#) (p. 21 ff.), which constitutes the second core task within the scope of this thesis. Finally, all results are summarized and a brief outlook is given in [Chapter 7](#) (p. 51 ff.). Important additional material can be found in the appendices (p. 55 ff.).

## 2. Flight Test Arrangement

A cutaway view of the SOFIA aircraft is displayed in [Figure 2.1](#). The TA is located inside the cavity in the rear section of the Boeing 747 SP. The remaining cabin is hermetically sealed by the forward and the aft pressure bulkhead in order to stay protected from atmospheric conditions prevailing inside the cavity while the door is open. In the middle section of the aircraft there are consoles for the flight engineers, telescope operators and scientists monitoring and controlling the technical equipment. During a SOFIA flight they can communicate via radio with the cockpit crew seated in the upper deck and with the DFRC *Mission Control Center (MCC)* room at the *Edwards Air Force Base (AFB)*.

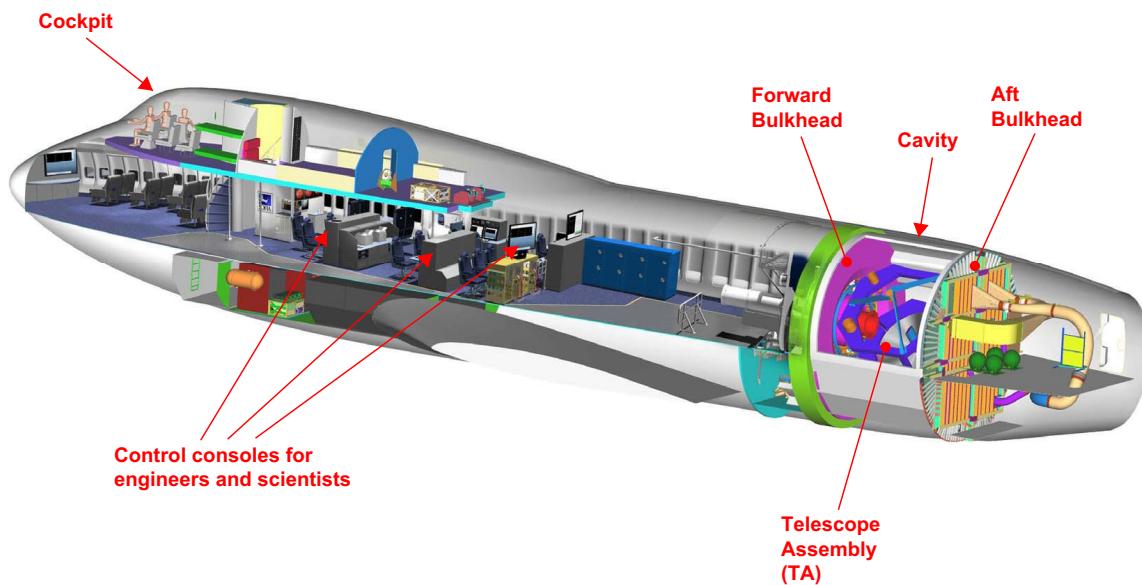
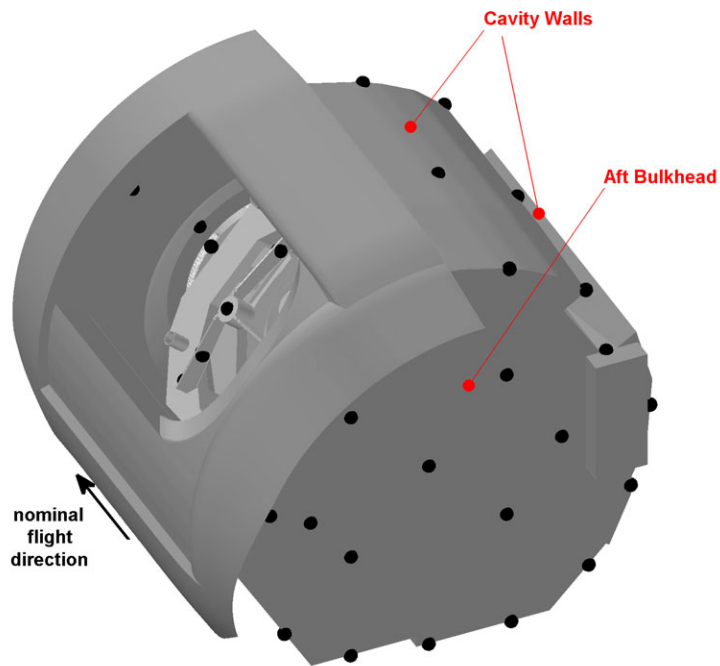


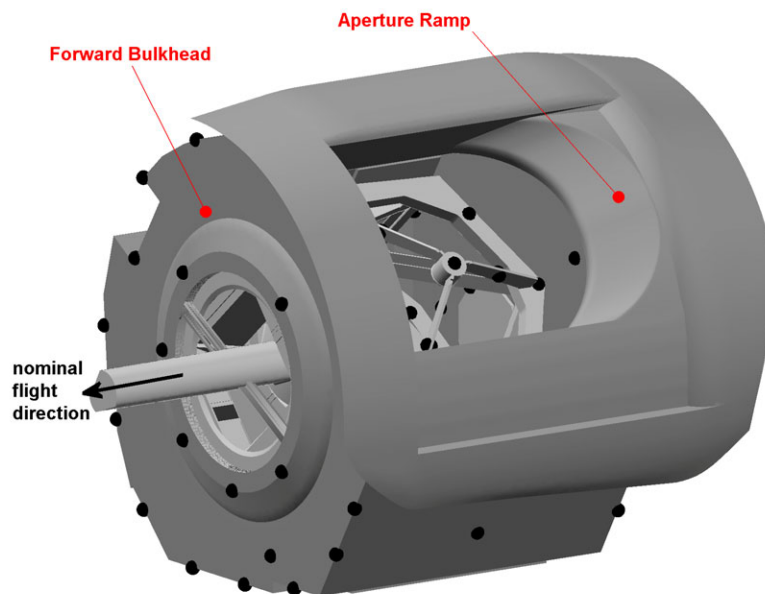
**Figure 2.1.:** SOFIA aircraft configuration. Parts of the hull to the left of the aircraft's symmetry plane have been made transparent in this 3D model in order to give an insight of the aircraft interior. © NASA

### 2.1. Relevant sensors and geometry

Both the inner cavity surface and the TA surface constitute the aeroacoustically relevant geometry for this thesis. As shown in [Figure 2.2](#) on p. 4 and in [Figure 2.3](#) on p. 5, the cavity and the telescope can be divided into subcomponents respectively and are equipped with 120 pressure sensors, which are representatively distributed on their surfaces and yield a sampling rate of  $f_{s,p} = 1000$  Hz. In order to ensure the highest informative value with the given amount of sensors, their optimal locations have been determined by means of wind tunnel tests and CFD simulations [22]. The aeroacoustic analysis of the telescope and cavity in [Chapter 6](#) is explicitly based upon these 120 sensors, whereas sensors



(a) View on Aft Bulkhead and Cavity Walls.



(b) View on Forward Bulkhead and Aperture Ramp.

**Figure 2.2.:** SOFIA cavity components. In this 3D model, the inner surface of the cavity is shown from outside. In both views, the TA is visible partly through the cavity opening. The *nominal* flight direction indicated by the black arrow corresponds to the longitudinal airplane axis or the elevation axis (see [Figure 2.4](#) on p.6). The black dots on the geometry surface represent the relevant 120 pressure sensors used for the aeroacoustic analysis in [Chapter 6](#) (p.21 ff.). The 59 cavity sensors are grouped according to their component affiliation (cp. [Table B.2](#) on p.67 ff.).

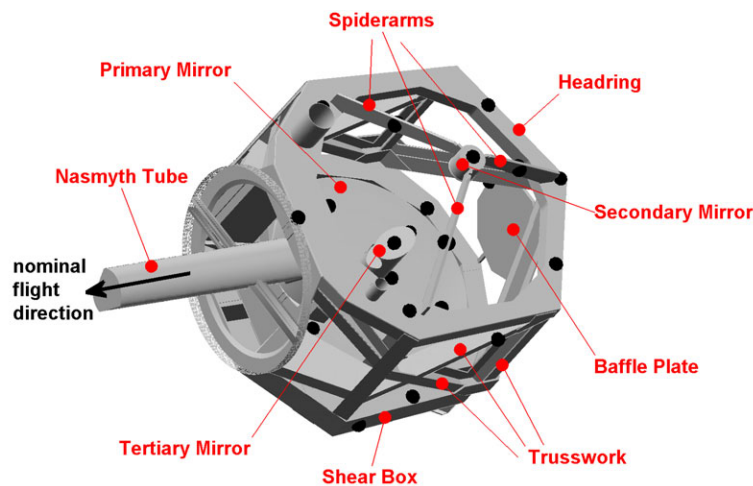


**Figure 2.3.:** SOFIA telescope components. In this 3D model, essential TA subassemblies accommodating pressure sensors are labeled. For a better overview, the 61 TA sensors are formally split up into local sensor groups analogously to the sensors on the cavity surface (cp. [Table B.2](#) on p. 67 ff.).

on other components (see [Figure 2.4](#) on p. 6) are not taken under consideration. A detailed overview of all 236 existing pressure sensors on the SOFIA configuration as well as their properties, locations and assigned sensor groups can be found in the appendix in [Section B.2](#) (p. 67 ff.).

Most of the installed pressure sensors are transducers which are able to measure the absolute static pressure in the range of 0–15 psi. In conjunction with the data system’s 12 bit analog-to-digital converter (A/D), they consequently feature an amplitude discretization of approximately  $15 \text{ psi} / 2^{12} = 0.0036 \text{ psi}$ . This means that a regular occurrence of random blips can already result in sound pressure levels<sup>1</sup> (SPL) around 120 dB [5]. In opposition to the pressure transducers, there are few installed microphones capturing the pressure fluctuations directly by taking the difference between the ambient pressure (measured via reference tube) and the absolute pressure (measured by the microphone itself). Resolving a relatively small amplitude range of 0–1 psi [7], the microphones are much more accurate and suitable for acoustic measurements. As a result, it can be observed that SPL<sup>1</sup> values from pressure transducers which are lower than 117–120 dB merely originate from basic noise and cannot be attributed to existing pressure fluctuations [5], i. e. even with a completely closed cavity door the transducers issue SPL<sup>1</sup> values in this high order of magnitude. In contrast, the installed microphones expectedly feature an essentially lower ground noise level of 100 dB [6].

Strictly speaking, the sensors commonly assigned to the Secondary Mirror (SM) are in fact installed on the Secondary Mirror Mechanism (SMM). No sensors are attached to the mirror surface itself. The same is true for the Primary Mirror (PM). It is a part of the Primary Mirror Assembly (PMA), which includes additional support structure components. The sensors assigned to the PM are in fact attached to the structure on the bottom of the PMA (see [Figure B.1](#) (e) and (f)).

During envelope expansion flight tests ([Chapter 3](#) on p. 7 f.) the primary mirror was protected by the so-called suncover, which consists of several segments circumferentially arranged on top of the mirror. The signals of the suncover sensors during a test flight can be considered representative for the acoustics on the primary mirror surface during an operational flight without the cover.

<sup>1</sup>Sound pressure level (SPL): for explanation, see [Section 5.1](#) on p. 15.

## 2.2. Basic functionality of the configuration

A closer look at the section view of the configuration in [Figure 2.4](#) reveals that there are basically four assemblies that can be rotated around the longitudinal airplane axis, which corresponds to the so-called *elevation axis (EL)*:

1. The *Telescope Assembly (TA)* can be rotated within the operational elevation range of  $\gamma_{TA} = 17\text{--}68^\circ$  independently from the other components. The TA pointing direction, i. e. the direction of the PM symmetry axis, determines the *line-of-sight axis (LOS)*. The so-called *cross-elevation axis (XEL)* completes the EL and LOS axes to a right-handed coordinate system.
2. The *Aperture Assembly (AA)* acts like an independently relocatable window, through which the TA can view the sky. It can only be moved within the range of approximately  $23^\circ < \gamma_{AA} < 57^\circ$ . In case the *AA elevation angle*  $\gamma_{AA}$  and the *TA elevation angle*  $\gamma_{TA}$  are not equal, as it is displayed in [Figure 2.4](#), the configuration is *misaligned*. In the opposite case it is *aligned*. Merely the latter is analyzed in this thesis. The nominal operational configuration is aligned with an elevation angle of approximately  $\gamma_{AA} = \gamma_{TA} = 40^\circ$ . From an aeroacoustic point of view the aperture's most important component is the *Aperture Ramp* (see [Figure 2.2.b](#) on p. 4), which stabilizes the shear layer and reduces interaction with the cavity by deflecting disturbances<sup>2</sup>.
3. The *Lower Flexible Door (LFD)* is attached to the bottom of the AA. It functions like a sectional garage door, which follows the movements of the AA and covers the cavity part between the AA bottom and the lower edge of the airplane hull.
4. The *Upper Rigid Door (URD)* can open or close the cavity by sliding up or down on lateral tracks independently from the TA and the AA. It can be opened to a certain degree in order to control the aperture exposure  $e_{AA}$  depending on the AA position.

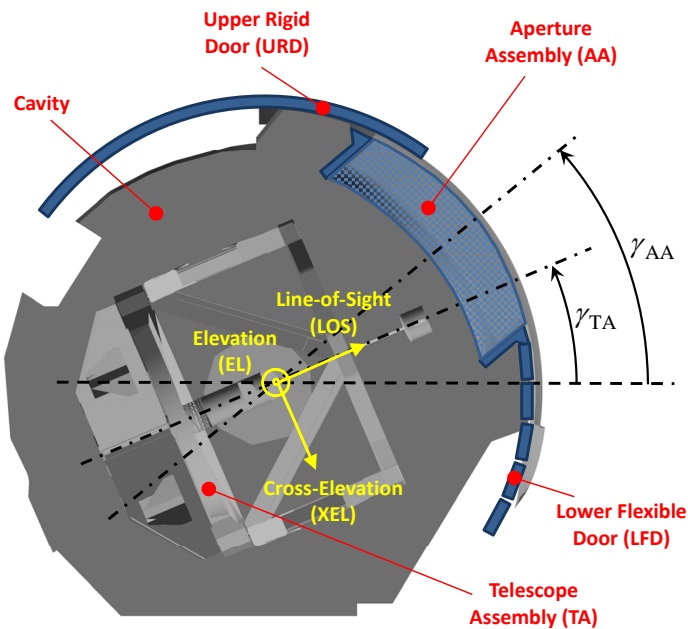


**Figure 2.4.:** Rotary parts of the SOFIA configuration (section view).

<sup>2</sup>For explanation, see [Section 5.2.2](#) (p. 17) and [Section 6.3.1](#) (p. 34 ff.).



### 3. Flight Tests for Envelope Expansion

Since SOFIA is a fundamentally *modified* airplane, it is necessary to analyze how it behaves during various flight phases and conditions with respect to dynamics, aerodynamics, aeroacoustics and other scientific and technical aspects. The question arises whether SOFIA is able to comply with the flight envelope of a conventional Boeing 747 SP and cope with the flight states designated to science missions<sup>1</sup>. In order for SOFIA to get certified by the *Federal Aviation Administration (FAA)*, the so-called envelope expansion flights have been performed between December 2009 and March 2011. During this extensive series of test flights SOFIA sequentially underwent various test points characterized by different combinations of altitude  $h$ , airspeed  $U_\infty$ , MACH number  $Ma_\infty$ , aperture exposure  $e_{AA}$ , AA elevation  $\gamma_{AA}$ , TA elevation  $\gamma_{TA}$ , angle of attack  $\alpha$ , sideslip angle  $\beta$ , flap deflection  $d_{fl}$  and so forth (see global parameters in [Section 4.1](#) on p. 9 f.).

Each test flight had been planned in advance and was framed by a crew brief before and after the event. The mission itself was guided and monitored by the staff in the control room at the Edwards Air Force Base in cooperation with the on board crew. In general, for each test point the following maneuvers have been performed to check the aircraft handling [24]:

- 1 minute trim shot
- 3 pitch doublets<sup>2</sup>
- 1 roll doublet<sup>2</sup>
- 1 yaw doublet<sup>2</sup>
- 3 yaw-roll doublets<sup>2</sup>
- 2 pull-up-push-overs (PUPO)
- 2 rudder sweeps

This thesis focuses merely on the so-called *trim shots*. During these short time segments, the aircraft achieves relatively steady flight conditions ( $p_\infty = \text{const.}$ ,  $Ma_\infty = \text{const.}$ , etc.) without any control inputs by the pilot. These flight attitudes are desirable for aeroacoustic studies because any variation of the mean pressure distorts the calculation of sound pressure levels<sup>3</sup> and power spectra<sup>3</sup> from the sensors' pressure signals (see [Section 6.1](#) on p. 22 f.).

In [Figure 3.1](#), the cleared SOFIA flight envelope (green) is plotted in an altitude-vs.-airspeed diagram. The blue dots indicate all relevant test points utilized for the aeroacoustic data analysis in [Chapter 6](#). The red dot represents the nominal operational point during a SOFIA science flight<sup>1</sup>, which is called the “baseline configuration”. It is characterized by the following properties [5]:

- $Ma_\infty = 0.85$
- $h = 35\,000\text{ ft}$

---

<sup>1</sup>*Science mission/flight*: mission flights during which astronomic observations are performed.

<sup>2</sup>*Doublet*: short and little deviation of the respective parameter below and above the starting value (full oscillation).

<sup>3</sup>For explanation, see [Chapter 5](#) (p. 15 ff.).

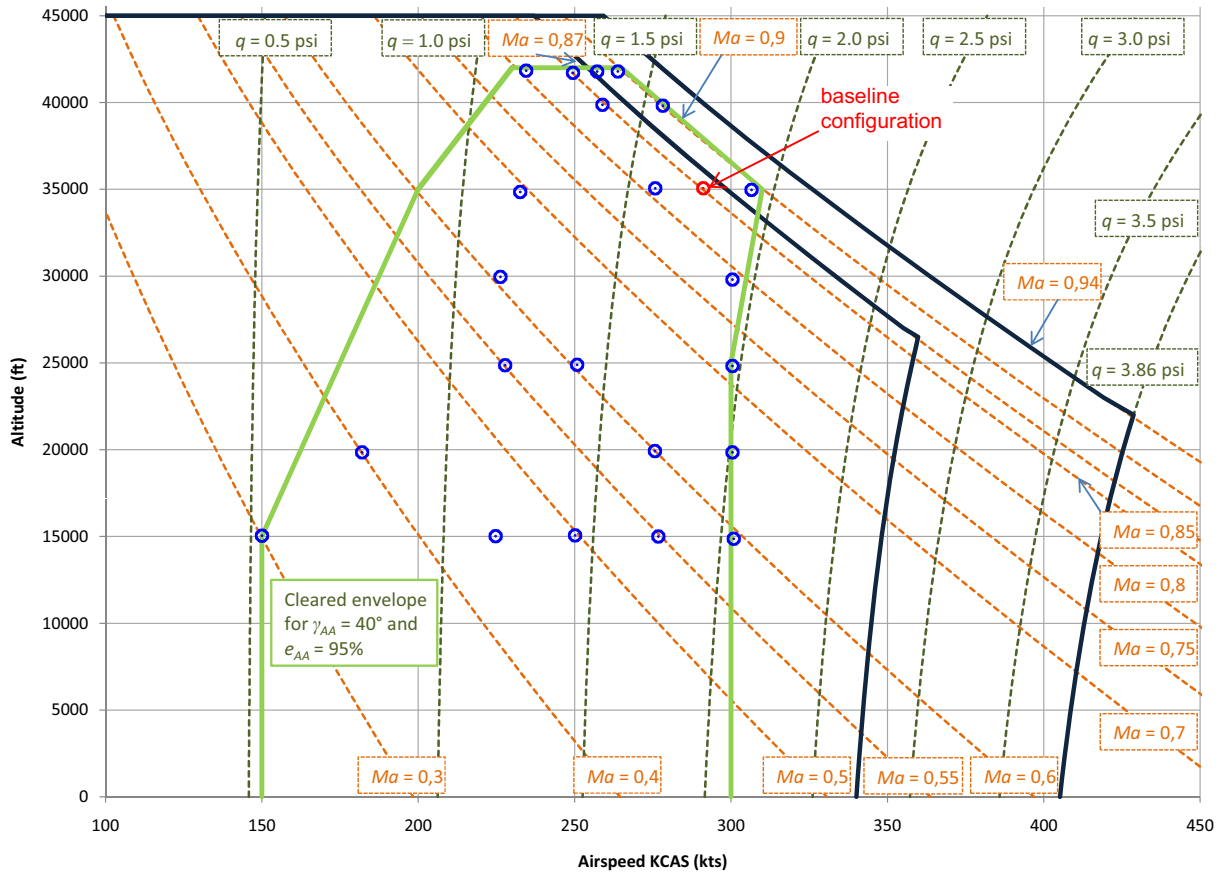


**Figure 3.1.:** Cleared SOFIA flight envelope (green) and relevant test points (blue) until February 2010. The altitude is on the ordinate and the knots calibrated airspeed (KCAS) on the abscissa. In addition, lines of constant MACH number and constant dynamic pressure are plotted. The two thick, dark-blue lines are theoretical operational limits, which are not further discussed in this thesis. The red point indicates the baseline configuration (nominal operational point of SOFIA during a scientific mission). © Engfer [5, 6]

- $\beta = 0^\circ$
- $e_{AA} = 100\%$

While the test points at and above  $h = 35\,000$  ft are relevant for the scientific operation of SOFIA, the points below are important inasmuch as they might be traversed with a fully or partly opened URD in case the door mechanism fails and the door is uncontrollable (open door landing).

For technical reasons, in order to decrease the AA elevation angle *in case of full aperture exposure* ( $e_{AA} = 100\%$ ), the URD has to be closed first. After the AA has been reset to its new position, the URD can be reopened again. In order to avoid this time-consuming procedure, most test points which were dedicated to a fully exposed aperture (elevated above the minimum of  $\gamma_{AA} = 23^\circ$ ) have been actually performed with a slightly lower aperture exposure ( $e_{AA} \approx 95\%$ ). For this reason, the flight test data set is not completely consistent. However, as it turns out in Figure C.1 on p. 83, the influence of this circumstance on the aeroacoustic behavior is insignificant so that  $e_{AA} \approx 95\%$  and  $e_{AA} = 100\%$  can be considered equivalent.

## 4. Flight Test Data

This chapter addresses the flight test data used for the aeroacoustic analysis in [Chapter 6](#) (p. 21 ff.) and gives a brief overview of data acquisition and processing. In particular, it points out the substantial optimization of the postprocessing procedure implemented by the author of this thesis, who has reworked and upgraded the *SOFIA Acoustic Data Analyzer (SADA)* for this purpose. Along with the flight data analysis, the planning and programming of an advanced postprocessing procedure was one of the core tasks of this study thesis.

### 4.1. Test Data Acquisition

The competence for the setup, operation and availability of the SOFIA instrumentation system including the pressure sensors introduced in [Section 2.1](#) (p. 3 ff.) is held by the NASA team. The flight data is distributed across five data streams, which are all recorded on board during a mission. In addition, streams 1 through 4 are also transmitted to the Mission Control Center at NASA Dryden so that selected data signals can be monitored in real-time.

After internal NASA preprocessing, the control room and onboard data are made available to the DSI team in the form of CMP4 files on external storage mediums. These compressed binary files contain the measurement data sorted by stream and sampling rate. Depending on the flight duration, the total amount of data can reach several hundred gigabytes [9]. Further general information on data acquisition and streams can be obtained from the *Control Room Guide* [23] and the thesis of Eger [4].

Two categories of sensor data are to be distinguished:

1. The *pressure data* contains the signals of all pressure sensors listed in [Section B.2](#) (p. 67 ff.). The previously discussed 120 relevant pressure sensors on the cavity and telescope with a sampling rate of  $f_{s,p} = 1000$  Hz provide the source for the later data analysis in [Chapter 6](#).
2. The *global data* comprises all parameters that characterize the flight conditions, e. g. MACH number, altitude, aperture position, elevation angles and so forth. The sampling rate  $f_{s,g}$  of these parameters is considerably lower since the data is merely used for orientation and is not subject to spectral analysis. All relevant global parameters are listed in [Table 4.1](#) on p. 10.

It is essential to pay close attention to characteristic and indicative acoustic events while monitoring both the pressure and global sensors in the MCC during flight. On the one hand, the exceedance of critical limits would require an immediate announcement (red phone calls) so that further measures can be taken to return to a safe flight state. On the other hand, it is important to promptly take notes of relevant observations on the so-called flight cards including the exact time and a short description. Later on, this information is necessary for data postprocessing and evaluation (see [Section 4.2](#))

Since the telemetry data usually contains regular nonphysical signal spikes, so called drop-outs, the onboard data is preferred. In any case, caution needs to be exercised while handling the data because erroneous sensor signals and certain preprocessing errors cannot be ruled out in both of them.

Parameter name	Parameter variable	Unit	Parameter ID	Stream №	Sampling rate $f_{s,g}$ [Hz]
MACH number	$Ma_\infty$	[-]	MINF_P	1	100
Knots calibrated airspeed	$U_{KCAS}$	[kts]	KCAS_P	1	100
Dynamic pressure	$q_\infty$	[psf]	QBAR	1	100
Static pressure	$p_\infty$	[psi]	PSPSI_P	1	100
Total pressure	$p_{t,\infty}$	[psi]	PTPSI_P	1	100
Flight altitude	$h$	[ft]	HP_P	1	100
TA elevation angle	$\gamma_{TA}$	[°]	TA03609	1	100
TA cross-elevation angle	$\chi_{TA}$	[°]	TA03612	1	100
Flap deflection	$d_{fl}$	[°]	FLAPPOS	1	100
Angle of attack	$\alpha$	[°]	ALPHA	4	100
Sideslip angle	$\beta$	[°]	BETA	4	100
AA exposure	$e_{AA}$	[%]	AA_OPENING	4	25
AA elevation angle	$\gamma_{AA}$	[°]	M09W06	4	25

**Table 4.1.:** Relevant global variables (extracted from [23]).

## 4.2. Test Data Postprocessing

After receiving the raw cmp4 data, further essential steps need to be taken in order to get meaningful results and draw conclusions:

1. The notes taken in the MCC highlight the few relevant sensor signals and serve to quickly find the time stamp position of the designated acoustic event. The exact time window considered for the assessment has to be chosen based on the smoothness of the flight conditions (see [Section 6.1](#) on p. 22 f.).
2. Once the time window and the signals are defined, the corresponding data has to be extracted and transformed into a readable format using a conversion tool.
3. Finally, depending on the user's needs, the readable material can be imported into programs that can perform calculations and are able to export or graphically present the results.

[Figure 4.1](#) on p. 11 outlines in further detail how this process chain used to be implemented in the early stages. It becomes obvious that a large, complex and partly iterative procedure was necessary in order to obtain useful information from a SOFIA flight. First, with the aid of flight card notes a global time window needed to be identified, i. e. the time span during which relevant flight tests took place. (The time on ground as well as during start, landing and taxiing is normally not of interest for the aeroacoustic analysis.) Next, the start and end point of this window, the time increment as well as the concerned data streams had to be entered into a global input text file (PY format). The Python<sup>®</sup> tool by Schmid [22] imported this input information and in turn called the NASA getdata converter in batch mode. The latter converted and exported the data to an ASCII file (American Standard Code for Information Interchange), which contains time stamps and their assigned numeric signal data.

In order to be able to perform a preliminary flight test analysis, a *Graphical User Interface (GUI)* named *SOFIA Acoustic Data Analyzer (SADA)* has been programmed by Schmid and Schwarz [24] by means of MATLAB<sup>®</sup>. It could be used to import the ASCII file and plot selected global parameters

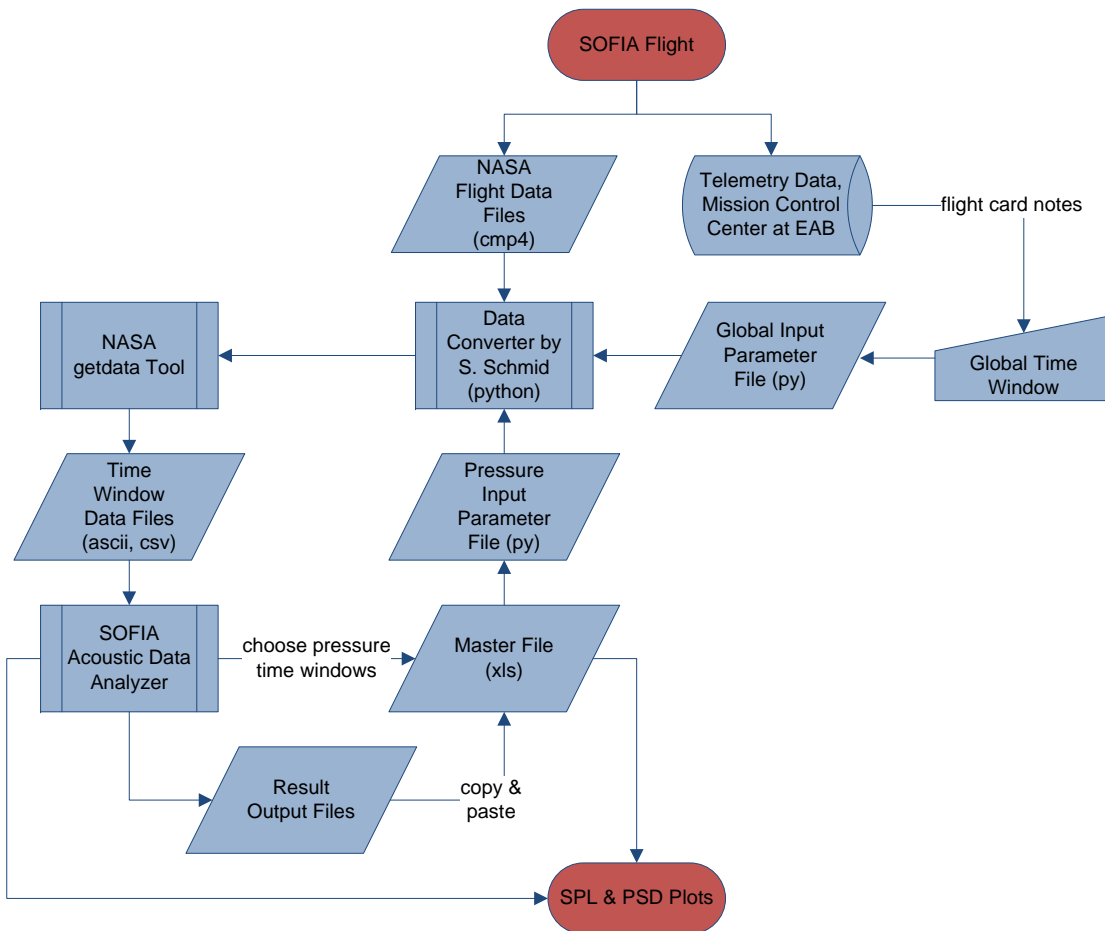


**Figure 4.1.:** Flow chart of the conventional postprocessing procedure. Large, complex and iterative process that used to be applied in the early stages.

giving the user an overview of the flight phases within the global time window. As a next step, on the basis of the plots it was possible to identify those short time windows which contained the desired test points previously marked on the flight cards. All start and end points of those windows along with the characteristic nomenclature and properties had to be manually entered into an Excel<sup>®</sup> master file (XLS or XLSX format) and saved as a comma-separated values (CSV) text file. The latter could be read by Schmid's Python<sup>®</sup> tool together with another input text file (PY format), where the desired time increment and the relevant data streams had to be manually adapted once again. By executing the tool a second data processing loop was started. The invoked NASA getdata converter transformed the selected time windows into ASCII files, which were automatically converted by Schmid's tool into the CSV format. The CSV files had a similar structure to their ASCII formatted counterparts, but they could be imported by SADA much quicker. At this point, SADA was able to display both global and pressure signals as well as computed acoustic values and characteristics in separate or single plots (cp. [Section 5.1](#) on p. 15 and [Section 5.3](#) on p. 19 f.). Notwithstanding, in order to be able to compare any parameters between different test points and to create user-defined graphs, these evaluation results used to be partly exported into the CSV format and manually copied and pasted into a new tab of the Excel<sup>®</sup> master file mentioned above. Apart from a set of plots, additional information and custom notes could be integrated in this file. Finally, the user's evaluation results

consisted of the master file and possibly additional MATLAB<sup>®</sup> plots generated by SADA. For more information on the discussed version of SADA, see the thesis of Schwarz [24]. The *reworked* and *upgraded* SADA is the subject-matter of Section 4.3.

### 4.3. SOFIA Acoustic Data Analyzer

This section is dedicated to the fundamental simplification and improvement of the conventional postprocessing procedure (Section 4.2 on p. 10 f.) as well as the implementation of comprehensive additional functionality. All this has been accomplished within the scope of this thesis by a complete revision and further enhancement of the SOFIA Acoustic Data Analyzer (SADA), which was a crucial prerequisite for the aeroacoustic analysis presented in Chapter 6 (p. 21 ff.).

Although being initially intended to operate as a part of the previously discussed intricate procedure, in the author's opinion SADA rather needed to act as the *central* chain link incorporating all the process-related subtasks autonomously and much more efficiently. It has been decided that the existing conventional process should be not only restructured, simplified and accelerated, but also extended by important additional program functions enabling the user to produce analysis plots of the same type as the CFD result plots of Schmid [22]. In this way, one could compare corresponding flight test results and CFD simulation predictions directly and vividly.

These goals have been achieved with the completion of the new SADA version in October 2010. Figure 4.2 shows the resulting optimized postprocessing procedure, in which SADA is the only, all-embracing interface that collects the user input, automatically performs all necessary computations and lets the user easily generate highly adaptable and exportable analysis plots of different types. It is obvious that the overall process has become significantly more manageable. Most subroutines illustrated in Figure 4.1 on p. 11 are now executed internally in SADA and due to their compatible interconnection a good portion of previously demanded user input can be derived automatically and does not need to be entered or copied and pasted any more. The only remaining external tool is the command line based NASA getdata converter which does not have a freely accessible source code. Nevertheless, the user does not have to deal with it neither because SADA supplies this tool with the required input information and subsequently utilizes its output by itself. An up-to-date screenshot of the SADA GUI can be found in Figure 4.3 on p. 14.

Apart from its role in the improvement and optimization of the overall process, SADA has been equipped with a wide range of additional features and advantages which were not present before:

- *The conversion and loading times have been drastically decreased.* Formerly time-consuming manual file inputs and operations are now handled by SADA subroutines automatically. In addition, a very fast algorithm is applied in SADA to convert the output of the NASA getdata tool to the MATLAB<sup>®</sup> file format (MAT). If an upgraded version of the NASA getdata converter (November 2010) is used, the CMP4 files can be converted directly to the CSV format instead of the undesirable ASCII format; in this case, the conversion algorithm is even faster by two orders of magnitude, e. g. it completes the job for a typical data set within 10 seconds instead of 10 minutes. Hence, an overall conversion process that used to last 1,5 hours can now be reduced by approximately 30 minutes.

Last but not least, the loading times in SADA have been decreased significantly. In fact, due to the superior storage format (MAT), they barely depend on the size of the data set. Even large data files can now be loaded within few seconds.

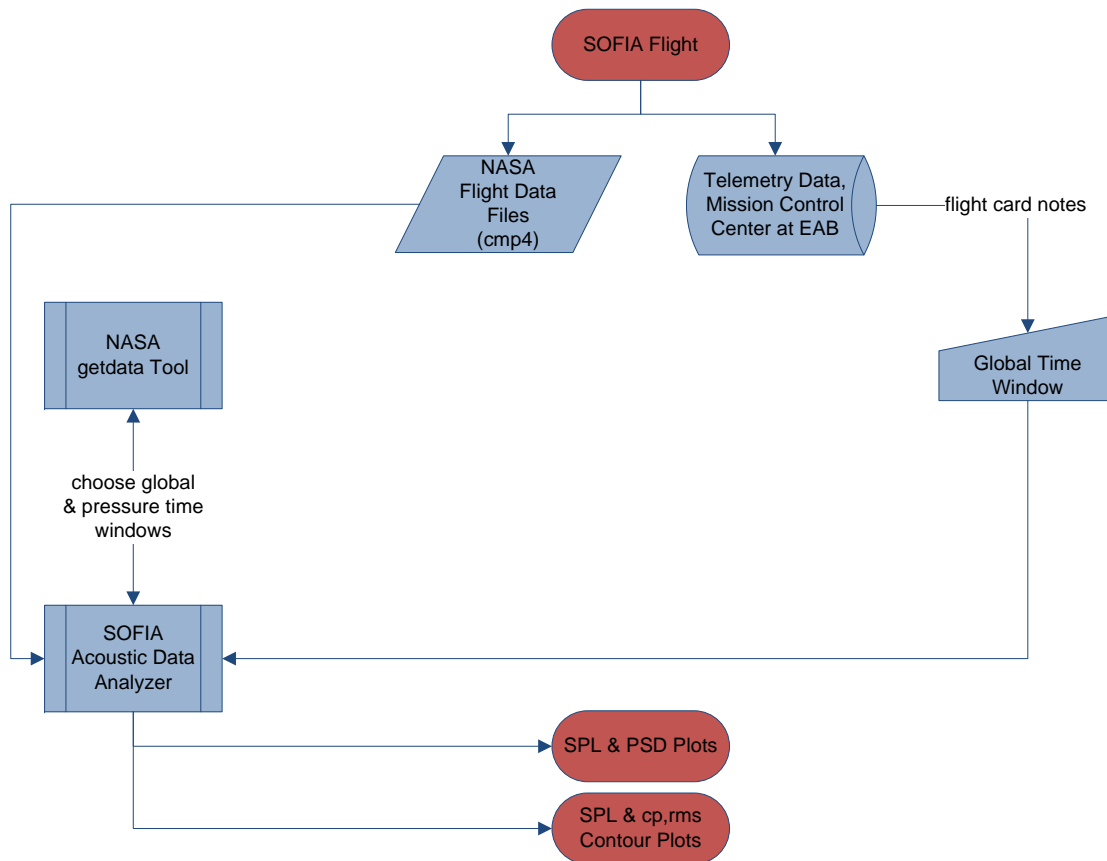


**Figure 4.2.:** Flow chart of the enhanced postprocessing procedure. This process is substantially simplified and more efficient. All missing elements displayed in Figure 4.1 on p. 11 are now implemented in SADA and do not need the user’s attention any more. Numerous internal and output features have been added.

- *A well-arranged session data base and session management system have been introduced.* All analysis operations related to a certain time window constitute a *session*. The specific files of each session are automatically stored in corresponding session directories with standardized and meaningful identifiers. Regardless of the amount of data the user never loses track and always can get quick access to previous analysis results via the GUI with no need to recalculate. An unlimited number of sessions can be loaded in SADA at the same time.
- *A complete and customizable sensor data base has been established.* All pressure sensors including their properties like sensor ID, location coordinates and sampling rates are stored in an editable spreadsheet table, which can be updated and compiled to a MAT formatted input file at any time. Within the GUI all loaded sensor signals are conveniently organized in groups for a faster selection/deselection and a better overview.
- *An interactive three-dimensional model of the relevant geometry and sensors has been linked to the workspace.* The view perspective, zoom factor and transparency of the configuration can be parametrically adjusted and sensors can be highlighted in color as “active” or “malfunctioning”.
- *Highly customizable plots can be created.* Due to the structured session management system, any parameters from any loaded session can be compared in single or separate plots. Moreover, the user can define specifications related to the figure windows, plot axes and plot contents.

#### 4. Flight Test Data

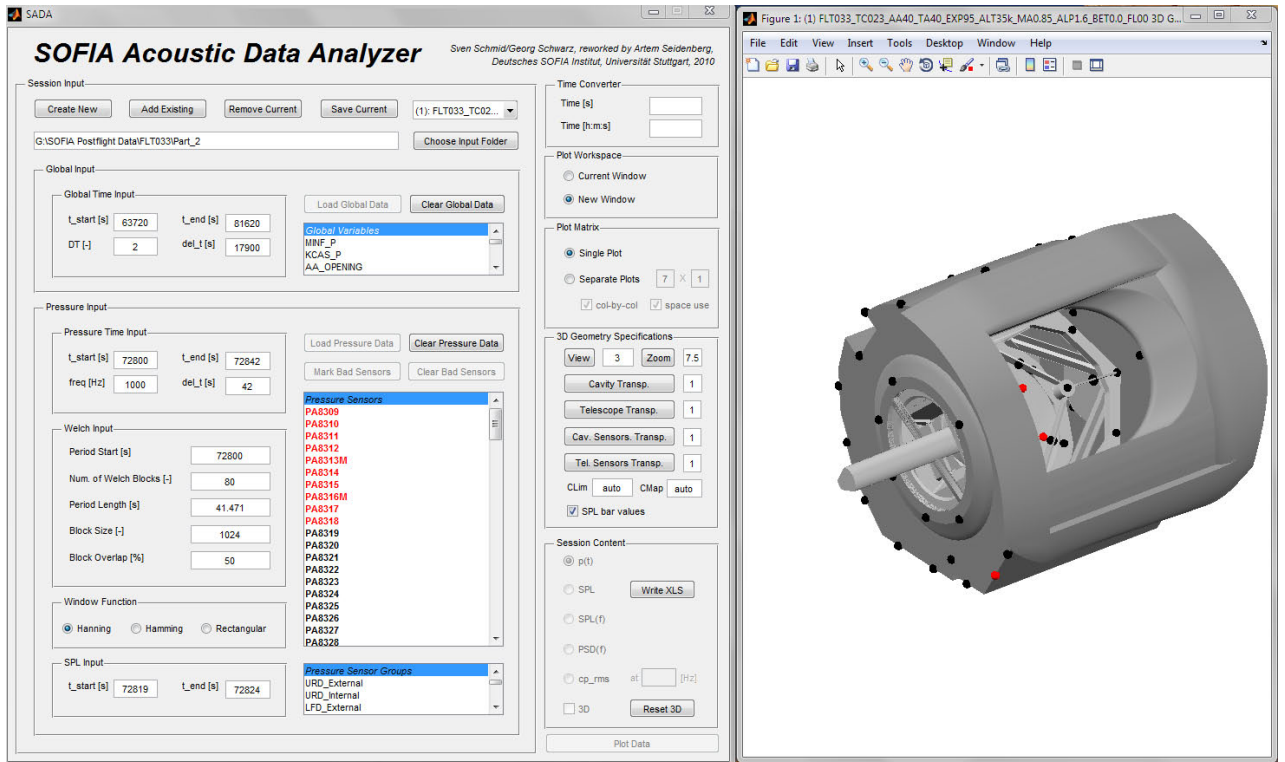


**Figure 4.3.:** Screenshot of the reworked SOFIA Acoustic Data Analyzer GUI, December 2010. The left window constitutes the workspace containing all controllers and user input fields, whereas the right window displays the interactive 3D model of the relevant SOFIA configuration in parallel. A bigger illustration of the workspace window can be found in [Figure A.1](#) on p. 56.

- *New computation routines and output plot types have been implemented.* Besides the ability to plot SPL spectra<sup>1</sup> in a two-dimensional graph, the most important additional feature is the three-dimensional *contour plot*, in which characteristic acoustic variables (SPL<sup>1</sup>,  $c_{p,rms}$ <sup>1</sup>) are represented by a color map, which is interpolated along the cavity surface using the computed values for every sensor as nodes.

In conclusion, it can be pointed out that the enhancements of SADA have made it a powerful, user-friendly stand-alone analysis tool, which offers increased efficiency and reduces working time and effort. Its customizability and new features significantly expand the range of possibilities and benefits for the user. Important operational guidelines for SADA are summarized in [Appendix A](#) (p. 55 ff.).

<sup>1</sup>SPL, SPL spectrum,  $c_{p,rms}$ : for explanation, see [Chapter 5](#) (p. 15 ff.).



# 5. Theoretical Background

## 5.1. Acoustics

*Acoustics* is a science field that commits to the study of *sound*, its origins and propagation, its generation and perception, its measuring and utilization. Sound is defined as mechanical waves in elastic mediums like gases, liquids or solids. *Aeroacoustics* is a subdiscipline of acoustics and deals with sound/noise generation that is *induced* by turbulent fluid flow and its interaction with solid surfaces [13, 16]. In case of a SOFIA flight, the atmospheric air flowing over and interacting with the fuselage, cavity and telescope is to be regarded.

Generally speaking, the sound field can be described by the absolute static values of pressure  $p$ , density  $\rho$  and particle velocity  $\mathbf{v}$  as the superposition of their ambient (subscript 0) and deviation (superscript  $\sim$ ) values,

$$p(\mathbf{r}, t) = p_0 + \tilde{p}(\mathbf{r}, t) \quad (5.1)$$

$$\rho(\mathbf{r}, t) = \rho_0 + \tilde{\rho}(\mathbf{r}, t) \quad (5.2)$$

$$\mathbf{v}(\mathbf{r}, t) = \mathbf{v}_0 + \tilde{\mathbf{v}}(\mathbf{r}, t), \quad (5.3)$$

where  $\mathbf{r}$  is the position vector and  $t$  is the time. The deviation  $\tilde{p}$  from  $p_0$  is called *sound pressure*, the deviation  $\tilde{\rho}$  from  $\rho_0$  is called *sound density* and the deviation  $\tilde{\mathbf{v}}$  from  $\mathbf{v}_0$  is called *sound particle velocity*. Acoustic fluctuations of field variables are characterized in that their amplitudes are much smaller than their ambient values (e.g.  $\tilde{p} \ll p_0$ ) and also than aerodynamic flow deviations [13].

A normal human ear can perceive sound pressures ranging from approximately  $2 \cdot 10^{-5}$  Pa to 20 Pa without difficulties. In order to be able to capture these six orders of magnitude and to make allowance for the non-linear human perception, it proved to be practicable to characterize sound pressure amplitudes via the so-called *sound pressure level*

$$L_p = 10 \log_{10} \left( \frac{p_{rms}^2}{p_{ref}^2} \right) = 20 \log_{10} \left( \frac{p_{rms}}{p_{ref}} \right). \quad (5.4)$$

It is a logarithmic measure of the root mean square (RMS) sound pressure

$$p_{rms} = \lim_{\Delta t \rightarrow \infty} \sqrt{\frac{1}{\Delta t} \int_0^{\Delta t} p^2(t) dt} \quad (5.5)$$

referred to  $p_{ref} = 2 \cdot 10^{-5}$  Pa = 20  $\mu$ Pa, the threshold of human hearing at a frequency of  $f = 1000$  Hz. The variable  $\Delta t$  constitutes the considered time interval.

## 5.2. Cavity Flow and Aeroacoustics

The air flow over a cavity is a complex physical occurrence that appears e. g. in aeronautics at open landing gear chambers, aircraft weapon bays or telescope cavities of airborne observatories like SOFIA. The understanding and prediction of cavity flow is important inasmuch as high-energy oscillations can lead to resonance in conjunction with acoustic cavity modes, generate significant pressure stresses and excite structural modes of interior objects.

### 5.2.1. Open and Closed Cavity Flow

In his work [22] Schmid distinguishes between two fundamentally different types of cavity flow using the length to depth ratio  $L/D$  as the differentiating and causal factor. If  $L/D \lesssim 7 - 8$ , the barely deformed outer flow completely covers the cavity and a big vortex inside the cavity evolves. Between the outer flow and the cavity interior a shear layer can be observed, the structure and properties of which are considerably influenced by the upstream boundary layer. This flow state is called *open cavity flow*. However, if  $L/D$  is further increased, the oncoming flow reattaches to the cavity base further upstream and two separate vortices in the cavity corners appear; in this case the so-called *closed cavity flow* prevails (see Figure 5.1).

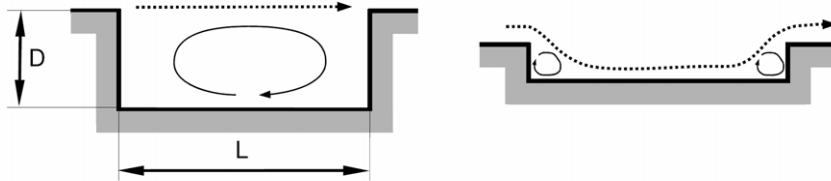


**Figure 5.1.:** Scheme of the open (left) and closed (right) cavity flow, using the example of a two-dimensional cavity. © Schmid [22]

The open cavity flow itself can be classified into three subcategories, which are characterized by different flow phenomena:

1. During *steady flow*, the cavity is overflowed as pictured in Figure 5.1 without any occurrence of time-dependent pressure fluctuations.
2. The *shear layer mode* is a flow state that is dominated by periodic pressure fluctuations. The so-called feedback process with characteristic oscillation frequencies takes place (see Section 5.2.2).
3. The *wake mode* features a highly transient flow with a chaotic character. The shear layer sheds large scale high-energy eddies.

The primary variables which determine the flow characteristic are the cavity geometry, the MACH number  $Ma_\infty$  and REYNOLDS number  $Re_\infty$  of the oncoming flow as well as the properties of the upstream boundary layer. Due to the complex interrelations between these parameters it is difficult to predict the flow state without numerical simulations. Finally, the research and extensive CFD simulations by Schmid revealed that the SOFIA configuration is subject to the open cavity flow in shear layer mode [22].

### 5.2.2. Feedback Process in Shear Layer Mode

Small disturbances within the shear layer convect downstream and due to its instability tend to increase. When impinging on the cavity back wall, they generate pressure waves (scattering), which travel back upstream inside and partly outside the cavity. These pressure fluctuations in turn excite the shear layer disturbances so that the feedback loop is complete (see Figure 5.2). As a result, a big recirculation flow with a pronounced primary vortex develops inside the cavity [22].

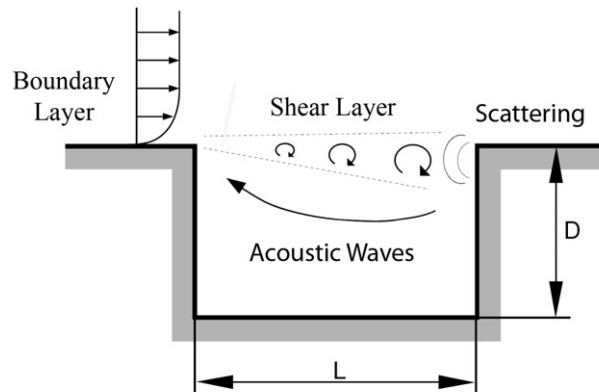


**Figure 5.2.:** Scheme of the feedback process during open cavity flow, using the example of a two-dimensional cavity. © Schmid [22]

Rossiter identified this feedback mechanism to be the cause of the periodic pressure fluctuations and established the simple semi-empiric formula

$$St = \frac{f_{Ross} \cdot L}{U_{\infty}} = \frac{m - \gamma}{Ma + \frac{1}{K}}, \quad m = 1, 2, 3, \dots \quad (5.6)$$

for two-dimensional, rectangular cavity configurations aiming to predict characteristic excitation frequencies [19]. The variables in the above formula have the following meanings:

- $St$**  STROUHAL number (dimensionless quantity characterizing the periodic behavior of the shear layer mode)
- $f_{Ross}$**  characteristic excitation frequency
- $L$**  cavity length
- $U_{\infty}$**  velocity of the oncoming flow (free stream velocity)
- $m$**  mode number
- $\gamma$**  dimensionless phase shift of acoustic waves with respect to the disturbance impingement at the cavity back wall
- $Ma$**  MACH number
- $K$**  ratio of the disturbance convection velocity  $U_c$  in the shear layer and the free stream velocity  $U_{\infty}$

### 5.2.3. Cavity Modes and Acoustic Resonance

If the characteristic frequencies of the feedback process are close or correspond to the purely acoustic cavity modes, the undesirable pressure fluctuations inside the cavity can increase drastically, which is known as *resonance*. Ahuja and Mendoza [1] provide a general relationship for such cavity modes in a motionless medium in the form of

$$St = \frac{L}{2 \cdot Ma} \cdot \sqrt{\left(\frac{n_x}{L}\right)^2 + \left(\frac{n_y}{2D}\right)^2 + \left(\frac{n_z}{W}\right)^2} \quad (5.7)$$

for a cuboid-shaped cavity with the length  $L$ , depth  $D$  and width  $W$ , where  $n_x = n_z = 0, 1, 2, 3, \dots$  and  $n_y = 0, 1, 3, 5, \dots$  denominate the mode numbers in the corresponding axial directions  $x, y, z$ . Whether these modes are excited and which of them are dominant, strongly depends on the acoustic damping that can be considered equivalent to the emissivity of acoustic energy into the far field [22]. A separated analysis including extensive *Computational Aeroacoustics (CAA)* simulations of cavity modes independently from occurring flow phenomena has been performed by Düring [3] and Schmid [22]. As Schmid states under reference to Plumblee et. al. [17], those acoustic modes dominate which correspond to the largest cavity dimension. Hence, regarding the SOFIA configuration the *depth-wise modes* can be expected to be most pronounced.

The diagram in Figure 5.3 expresses the relationship between the dimensionless frequencies of the first four ROSSITER excitation modes according to Equation 5.6 and the depth-wise cavity modes calculated by means of Equation 5.7 with  $n_x = 1$ ,  $n_y = 1, 3, 5, 7$  and  $n_z = 0$  (two-dimensional approach). The frequency lines coincide for certain MACH numbers (indicated by black dots), at which the system is particularly prone to resonance.

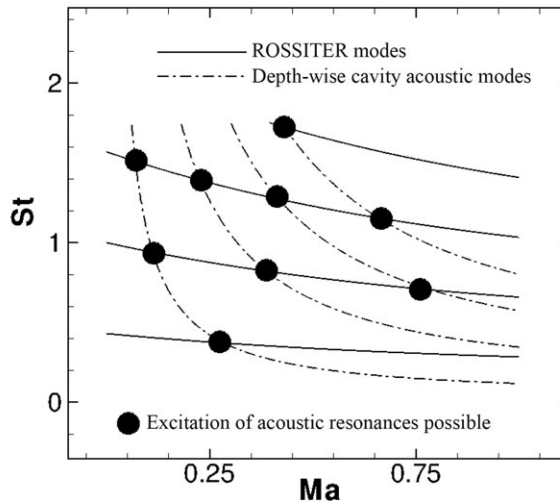


**Figure 5.3.:** Coupling between ROSSITER modes and depth-wise acoustic cavity modes. Resonance can occur for MACH numbers corresponding to intersection points (black dots). © Schmid [22]

It has to be pointed out that this section merely presents elementary physical mechanisms for a simplified theoretical cavity configuration, which cannot sufficiently reflect the real behavior of the highly complex SOFIA geometry. Therefore, numerical acoustic and flow simulations of the SOFIA configuration [3, 22] as well as a flight test analysis are indispensable.

## 5.3. Digital Signal Processing

Within the scope of this thesis, the pressure fluctuations at selected positions in the SOFIA cavity have been captured and transformed into time-discrete signals by the instrumentation described in [Section 2.1](#) (p. 3 ff.). The analysis and evaluation of these signals is based on certain methods of *Digital Signal Processing (DSP)*, which are described in this subsection.

According to the NYQUIST-SHANNON sampling theorem, a continuous signal has to be uniformly sampled with a sampling rate that is greater than twice its highest frequency in order to be able to reconstruct the original signal without any loss of information. However, an exact digital-to-analog back transformation would require an infinite number of samples [15]. Making use of a sufficiently high number of samples per analyzed time window (cp. [Section 6.1](#) on p. 21 ff.), the data analysis in this thesis focuses on sensor data with a sampling rate of  $f_{s,p} = 1000$  Hz. In this way, an adequate consideration of the signals' frequency band 0-200 Hz with at least five sampling points per oscillation can be assumed [7].

### 5.3.1. Discrete Fourier Transform

In order to transfer the time-discrete signals into the frequency domain, the so-called *Discrete FOURIER Transform (DFT)* is applied. The sequence of complex amplitudes  $A[k]$  (FOURIER coefficients) can be obtained from the sequence of  $N$  samples  $a[j]$  in the time domain via

$$A[k] = \sum_{j=0}^{N-1} a[j] \cdot e^{-i\frac{2\pi}{N}jk}, \quad k = 0, 1, \dots, N-1. \quad (5.8)$$

Since the input signal  $a[j]$  is *real* in the mathematical sense, the HERMITIAN symmetry of the output signal in the frequency domain can be utilized. Practically, this means that only  $\frac{N}{2}$  (if  $N$  is even) or  $\frac{N}{2} + 1$  (if  $N$  is odd) independent FOURIER coefficients  $A$  exist and need to be calculated [15].

### 5.3.2. Power Spectral Density and Welch's method

An important characteristic of a signal is its *Power Spectral Density (PSD)*, which describes how the power of this signal is distributed with frequency [15]. In order to accurately estimate the PSD of a finite time signal with a justifiable effort, the so-called *WELCH's method* [26] is used:

1. The original set of  $N$  data points (samples) is divided into  $R$  segments (WELCH blocks) containing  $S$  points overlapping to a certain degree  $v_b$  (preferably 50 %).
2. Each block is multiplied by a window function in order to suppress the leakage effect. Possible functions [15] may be for instance the HANNING window

$$w[j] = 0.54 - 0.46 \cdot \cos\left(\frac{2\pi j}{N-1}\right), \quad j = 0, 1, \dots, N-1, \quad (5.9)$$

the HANNING window

$$w[j] = \frac{1}{2} \left[ 1 - \cos\left(\frac{2\pi j}{N-1}\right) \right], \quad j = 0, 1, \dots, N-1 \quad (5.10)$$

or the BLACKMAN window

$$w[j] = 0.42 - 0.5 \cdot \cos\left(\frac{2\pi j}{N-1}\right) + 0.08 \cdot \cos\left(\frac{4\pi j}{N-1}\right), \quad j = 0, 1, \dots, N-1, \quad (5.11)$$

In accordance with Schmid's work [22], the popular HANNING window as per Equation 5.10 is preferred in this thesis.

3. Subsequently, the DFT is applied to each block and then the squared magnitude of the result is computed respectively. Finally, these so-called periodograms are time-averaged in order to reduce unfavorable signal noise.

The result is an array of PSD-frequency pairs, which can be plotted in a diagram. Once the power spectrum is present, the spectra of the SPL and the RMS pressure coefficient  $c_{p,rms}$  can be determined by simple algebraic rearrangements as well.

WELCH's method has been implemented in SADA within the MATLAB<sup>®</sup> environment (see Appendix A on p. 12 ff.).

# 6. Flight Test Data Analysis

Along with the implementation of the SOFIA Acoustic Data Analyzer (Section 4.3 on p. 12 f.), the current chapter constitutes the second core of this study thesis. It begins with a short introduction of the applied approach including the used conventions (Section 6.1) and continues with the three main parts of the aeroacoustic analysis: first, the most critical AA position and TA spots from an aeroacoustic point of view are examined by means of TA pressure sensor data (Section 6.2). In particular, this serves to establish an increased awareness of unfavorable aeroacoustic activity inside the cavity, which might lead to telescope pointing disturbances for certain operating points. Second, a parameter variation analysis (Section 6.3) is conducted and compared to simulation-based studies of Schmid [22], allowing to gain a vast overview of the dependencies between flight parameters and aeroacoustics of the SOFIA configuration. Finally, the spatial distribution of acoustic fluctuations on the cavity surfaces is evaluated and compared to analogous CFD simulation results by Schmid [22].

## 6.1. Data Analysis Approach

The data analysis in the following sections of this chapter is based on the digital pressure signals of selected sensors that are currently installed on the surfaces of the relevant SOFIA geometry (Section 2.1 on p. 3 f.). The raw pressure data serves as input for SPL calculations and WELCH analyses (see Chapter 5 on p. 15 ff.) based on certain characteristic time slots. This allows to draw meaningful conclusions about the aeroacoustic behavior of the SOFIA configuration being exposed to the free atmosphere. All data processing, ranging from data acquisition to resulting plot generation, has been performed by means of the SOFIA Acoustic Data Analyzer (Section 4.3 on p. 12 f.).

Within the scope of this thesis, the following conventions and limitations regarding the aeroacoustic analysis have been put into force:

### Time window length

Observations by Engfer [7] suggest that  $R = 80$  is an appropriate number of WELCH blocks for the spectral analysis of the regarded data signals by means of WELCH's method. In conjunction with the discussed sampling rate  $f_{s,p} = 1000$  Hz, the default block size of  $S = 1024$  samples and the default block overlap  $v_b = 50\%$ , it yields an overall number of

$$N = R \cdot S \cdot \left(1 - \frac{v_b}{100\%}\right) + S \cdot \frac{v_b}{100\%} = 41\,472 \quad (6.1)$$

samples and an overall time period length of

$$\Delta t_p = \frac{N - 1}{f_{s,p}} = 41.471 \text{ s}. \quad (6.2)$$

On the one hand, this time window is short enough to avoid long extraction and conversion times by the NASA getdata tool ([Chapter 4](#) on p. 9 ff.) as well as disproportionate deviations from the steady flight state; on the other hand, it is long enough to generate PSD plots with an adequate resolution of peaks [7].

Since the sound pressure is defined as the local pressure deviation from the ambient pressure ([Section 5.1](#) on p. 15), the SPL values shall be based on time segments which allow the assumption of a sufficiently steady ambient pressure. Hence, it has been decided to limit the time segment length for SPL calculations to  $\Delta t_{SPL} = 5$  s. Nevertheless, considering the regarded sampling rate  $f_{s,p} = 1000$  Hz, this time frame is still sufficient to capture a representative amount of acoustic oscillations.

### Window function for Welch analysis

SADA offers three different window functions that can be applied to the WELCH blocks in the time domain before the periodogram computations:

- Rectangular window according to 
$$w[j] = 1 \tag{6.3}$$
- HAMMING window according to [Equation 5.9](#) on p. 19
- HANNING window according to [Equation 5.10](#) on p. 19

Following the suggestion of Schmid [22], the popular HANNING window is used in this thesis.

### Time window location

This thesis is dedicated to the analysis of the aeroacoustic behavior under *steady* flight conditions. Therefore, only the trim shots  $\Delta t_{ts} \approx 1$  min, which were performed during the envelope expansion flights, are of importance (cp. [Chapter 3](#) on p. 7). Thus, the time window  $\Delta t_p$  is to be positioned within  $\Delta t_{ts}$  such that the steady state in terms of global parameters is preserved best, assuming that as a result the ambient pressure remains approximately constant either. Once the pressure data has been extracted, the time segment  $\Delta t_{SPL}$  shall be chosen within  $\Delta t_p$  accordingly where the most steady behavior of the ambient pressure can be observed (see [Figure 6.1](#) on p. 23). Since the trim shot is not perfectly steady, the computed SPL values might vary by  $\pm 1$  dB depending on the selected time window.

### Global parameters

The degree of constancy of the following selected global parameters<sup>1</sup> serves to detect the optimum time window location:

- Mach number  $Ma_\infty$  (MINF\_P)
- Knots calibrated airspeed  $v_{KCAS}$  (KCAS\_P)
- Aperture exposure  $e_{AA}$  (AA\_OPENING)
- Dynamic pressure  $q$  (QBAR)

---

<sup>1</sup>A list of relevant global parameters including their properties can be found in [Table 4.1](#) (p. 10 f.).



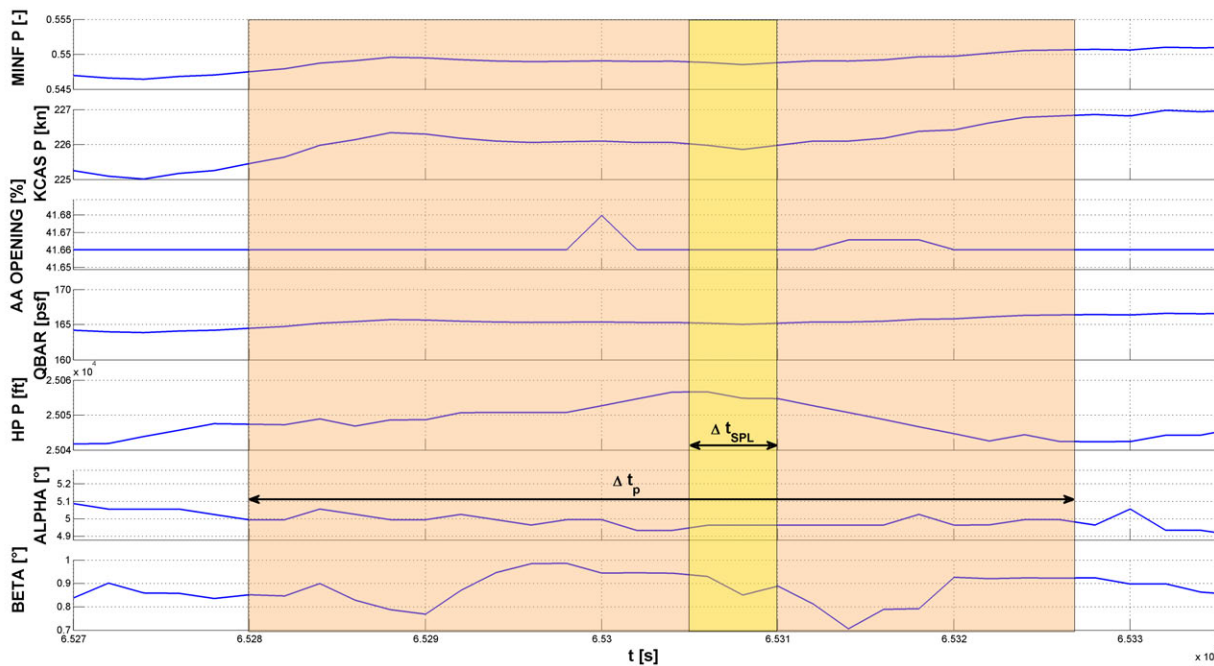


Figure 6.1.: Selection of time windows (using the example FLT033\_TC009\_AA40\_EXP40\_ALT25k\_Ma0.55).

- Flight altitude  $h$  (HP\_P)
- Angle of attack  $\alpha$  (ALPHA)
- Sideslip angle  $\beta$  (BETA)

In order to avoid unneeded data overload, samples are extracted every two seconds (i. e.  $f_{e,g} = 0.5$  Hz) for all global parameters regardless of their native sampling rates.

### Pressure sensors

The data analysis in this thesis uses 120 pressure sensors, which issue a sampling rate of  $f_{s,p} = 1000$  Hz. For clarity purposes, these sensors have been divided up into sensor groups according to their assembly affiliation<sup>2</sup>. In the following sections, sensor group *average* curves or values are utilized as simplified representative indicators for the aeroacoustic conditions at the respective structure assemblies.

As already mentioned, the conventional pressure transducers, constituting the majority of the available pressure sensors, exhibit a basic noise level of approximately 117-120 dB so that only SPL values above this limit can be interpreted as physical pressure fluctuations. In contrast, the few installed microphones have a much lower basic noise level of approximately 100 dB [6].

### Session nomenclature

On the one hand, every time window  $\Delta t_p$  is unambiguously determined by the flight number and the time window limits; on the other hand, it can be identified by the name of the corresponding

<sup>2</sup>In comparison to the work of Schwarz [24], a slightly different sensor group distribution according to Section B.2 on p. 67 ff. has been defined.

SADA session containing the flight state characteristics (see [Section B.1](#) on p. 65 ff.). The latter alternative is utilized by the author to refer to analyzed time segments in figure or table captions. The nomenclature for these session references has the following structure:

$$\underbrace{\text{FLT033}}_1 - \underbrace{\text{TC023}}_2 - \underbrace{\text{AA40}}_3 - \underbrace{\text{TA40}}_4 - \underbrace{\text{EXP95}}_5 - \underbrace{\text{ALT35k}}_6 - \underbrace{\text{MA0.85}}_7 - \underbrace{\text{ALP1.6}}_8 - \underbrace{\text{BET0.0}}_9 - \underbrace{\text{FL00}}_{10} - \underbrace{\text{VER2}}_{11}$$

1. Flight Number
2. Test card number
3. Aperture elevation  $\gamma_{AA}$  [°]
4. Telescope elevation  $\gamma_{TA}$  [°]
5. Aperture exposure  $e_{AA}$  [%]
6. Flight altitude  $h$  [ft]
7. Mach number  $Ma_{\infty,p}$  [-]
8. Angle of attack  $\alpha$  [°] (optional)
9. Sideslip angle  $\beta$  [°] (optional)
10. Flap position  $d_{fl}$  [°] (optional)
11. Session version number (in case if more than one redundant session exists)

A detailed listing of respective session characteristics including the location of  $\Delta t_p$ ,  $\Delta t_{SPL}$ , etc. can be found in [Section B.1](#) (p. 65 ff.).

As already mentioned in [Section 2.2](#) on p. 6 f., one should keep in mind that only *aligned* configurations of the AA and TA are taken into consideration. To simplify matters, the following sections might merely refer to  $\gamma_{AA}$ , but imply that  $\gamma_{AA} = \gamma_{TA}$ .

### Plot types and nomenclature

This chapter makes use of all five plot types which SADA is able to generate. In [Table 6.1](#), they are opposed to their default nomenclature.

Plot type	Nomenclature
SPL bar chart based on $\Delta t_{SPL}$	SPL bar chart
SPL plot versus frequency $f$ based on WELCH analysis ( $\Delta t_p$ )	SPL( $f$ ) plot
PSD plot versus frequency $f$ based on WELCH analysis ( $\Delta t_p$ )	PSD( $f$ ) plot
$c_{p,rms}$ contour plot for defined frequency $f$ based on WELCH analysis ( $\Delta t_p$ )	$c_{p,rms}$ contour plot
SPL contour plot based on $\Delta t_{SPL}$	SPL contour plot

**Table 6.1.:** SADA plot types and nomenclature.

The first three plot types are two-dimensional, whereas the last two plot types display a distribution of characteristic acoustic variables over the cavity surface by means of color map interpolation using the calculated sensor values as nodes (cp. [Section 4.3](#) on p. 12 ff.).

## 6.2. Telescope Assembly Aeroacoustics

In consideration of the enormous amount of available flight test data gained from numerous flights, it is imperative to narrow down the attention to those test points and locations on the TA which are characterized by the *most critical* aeroacoustic behavior. In the following, the word “critical” is solely used in an aeroacoustic sense.

In this section, the critical AA position as well as the critical TA spots (hot spots) are discussed in order to provide a qualitative understanding and awareness of unfavorable SOFIA flight conditions with respect to flight safety and pointing stability.

### 6.2.1. Critical Aperture Assembly Position

As it turned out during the flight tests, the AA elevation has a strong influence on the aeroacoustic behavior inside the cavity. In particular, this manifests itself in the TA sensor signals. The average PSD distribution of all TA sensors are compared in [Figure 6.2](#) for different AA positions in baseline configuration. It becomes obvious that the PSD curve corresponding to an AA position of  $\gamma_{AA} = 40^\circ$  dominates over almost the whole displayed frequency range. Since the area under the PSD curve is a measure for the overall acoustic power [15], it can be concluded that  $\gamma_{AA} = 40^\circ$  represents the most critical AA position from an aeroacoustic point of view, e. g. the AA position with the most energetic noise. The same conclusion can be drawn from the average SPL bar chart in [Figure C.2](#) (p. 84 ff.). Hence, future considerations will mainly focus on  $\gamma_{AA} = 40^\circ$ .

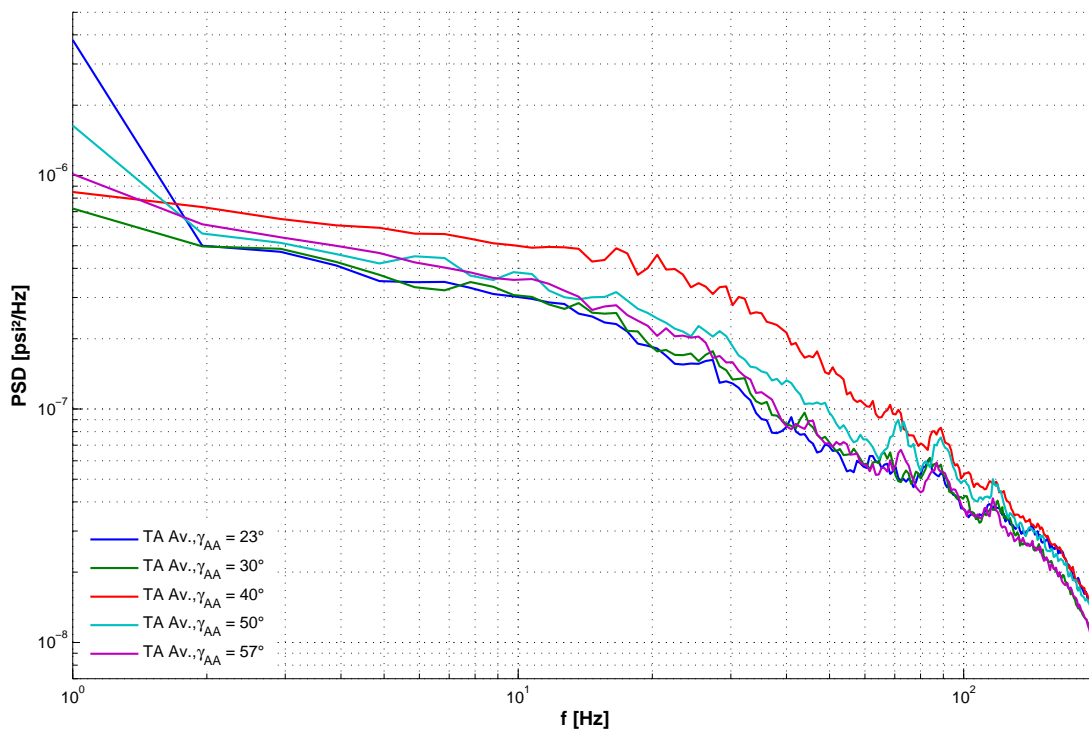


**Figure 6.2.:** PSD( $f$ ) plot of the telescope average for different aperture positions in baseline configuration. The PSD distribution for  $\gamma_{AA} = 40^\circ$  yields the highest values over almost the whole displayed frequency range. FLT026,35,35,41,41\_TC010,25,30,22,30\_AA23-57\_EXP95,100\_ALT35k\_MA0.85.

## 6.2.2. Critical Telescope Assembly Spots

### Hot Spot Identification

In order to identify the hot spots on the telescope, the SPL values of all TA sensors have been determined. In [Figure 6.3](#), they are presented in the form of an SPL bar chart split up into respective TA sensor groups. The red bars stand for the previously determined critical AA elevation  $\gamma_{AA} = 40^\circ$ , whereas the multicolored triangles represent the remaining AA positions tested during the envelope expansion flights. Those sensors of which the SPL values clearly exceed the basic noise level of approximately 120 dB for all AA elevations are denominated “hot spots”.

The locations of these critical sensors are highlighted in [Figure 6.4](#) on p. 28. It stands out that most of the TA hot spots are asymmetrically gathered on the rear upper part of the telescope. This becomes plausible considering the CFD simulation results by Schmid [22] in [Figure 6.5](#) on p. 28. Schmid discovered that a part of the linearly spreading shear layer is redirected inside the cavity after impingement on the aperture ramp. The resulting downward fluid jet has been called “downwash”. It enters the TA slightly above the rear spiderarm and impinges on the headring and primary mirror (marked in red and yellow). While flowing, it manifests itself in outstanding MACH numbers according to [Figure 6.5.a](#), whereas a particularly high overload pressure can be detected at the impingement areas ([Figure 6.5.b](#)). As one can easily comprehend, the high kinetic energy of the downwash and the small scale shear layer disturbances which it carries result in very high SPLs and broadband spectral characteristic yielded by the affected sensors.

Hence, the CFD simulation results of Schmid [22] can be related to the discovered hot spot sensors in the following way:

- Very prominent hot spots can be observed on the headring. Sensor PA8352<sup>3</sup> yields the highest SPL value and thus seems to be most exposed to the downwash impingement. The same phenomena is also noticeable in a weaker form by the headring sensor PA8368 and the suncover sensor PA8313M<sup>3</sup>. This indicates on the one hand that sensor PA8368 might be located in the periphery of the downwash and on the other hand that the downwash gets much weaker when arriving at the primary mirror (cp. [Figure 6.5](#)).
- Apparently, the sensors PA8349<sup>3</sup> and PA8350<sup>3</sup>, located on the Secondary Mirror Mechanism (SMM), are not exposed to the downwash. However, they issue quite high SPL values, which results from their proximity to the high-energy shear layer flow. The same is true for the sensors on the spiderarm at 11 o’clock (PA8363<sup>3</sup> and PA8366<sup>3</sup>) and on the rear spiderarm (PA8362<sup>3</sup> and PA8365<sup>3</sup>). The latter two seem to be additionally affected by the periphery of the downwash according to [Figure 6.5.a](#). This is also reflected by the fact that these two sensors yield higher SPL values than their counterparts. PA8365 even yields the TA maximum value of 137 dB.
- It is not very well understood, why the headring sensor PA8351<sup>3</sup> and the two shear box sensors PA8329 and PA8334 detect such a high noise level. This behavior is not reflected by the CFD results. As for the sensor PA8351, it can be supposed that the real downwash is more extended than suggested by the simulations and hence has an influence on this sensor as well. In contrast, the shear box sensors are completely shielded from the shear layer and downwash. However, one explanation for their high SPLs might be that, impinging on the primary mirror, the downward flow jet causes scattered pressure waves, of which a big part is channelized towards PA8329 and in a weaker form towards PA8334.

---

<sup>3</sup>These observed hot spots accord with those reported by Engfer [5, 6].

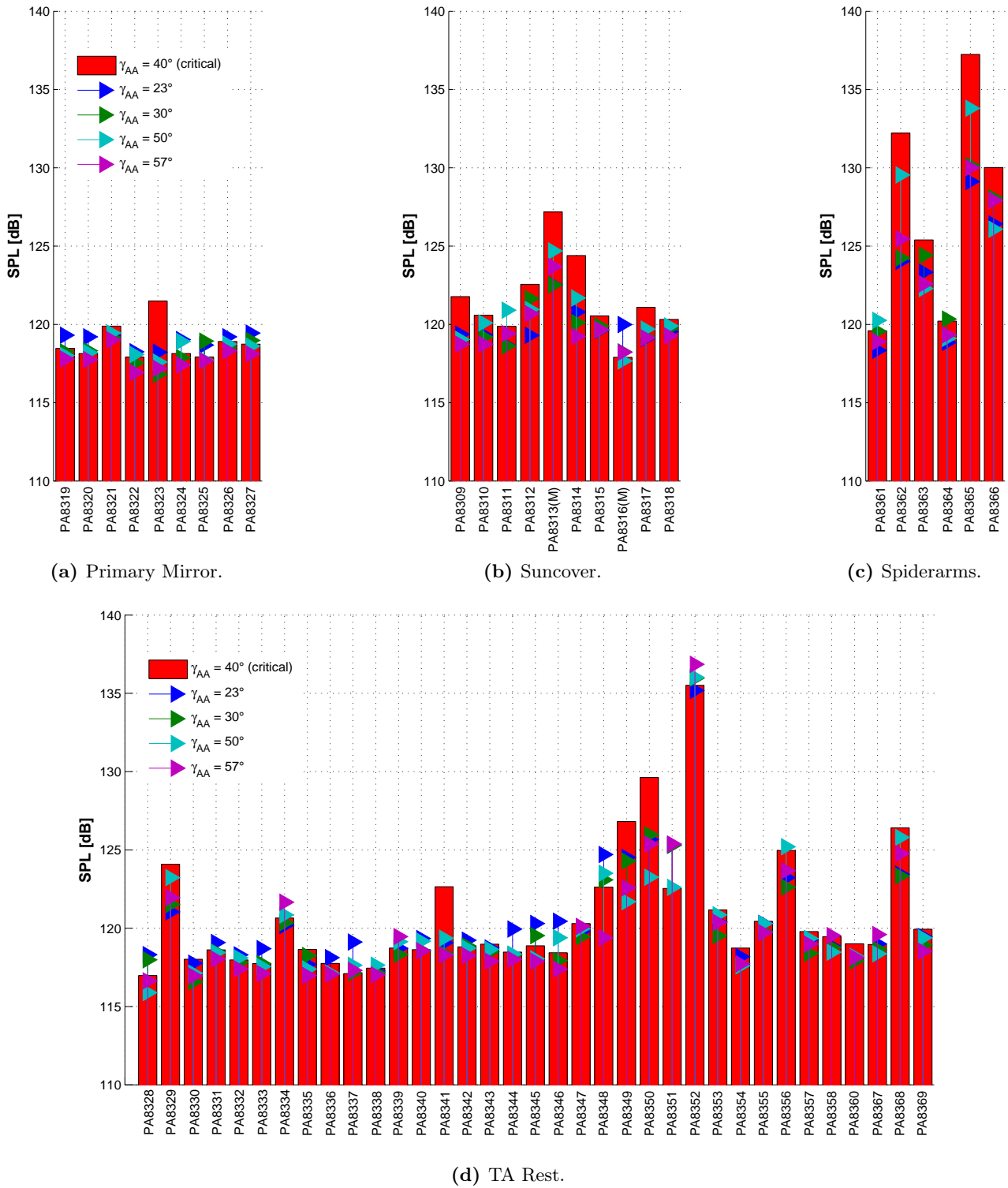
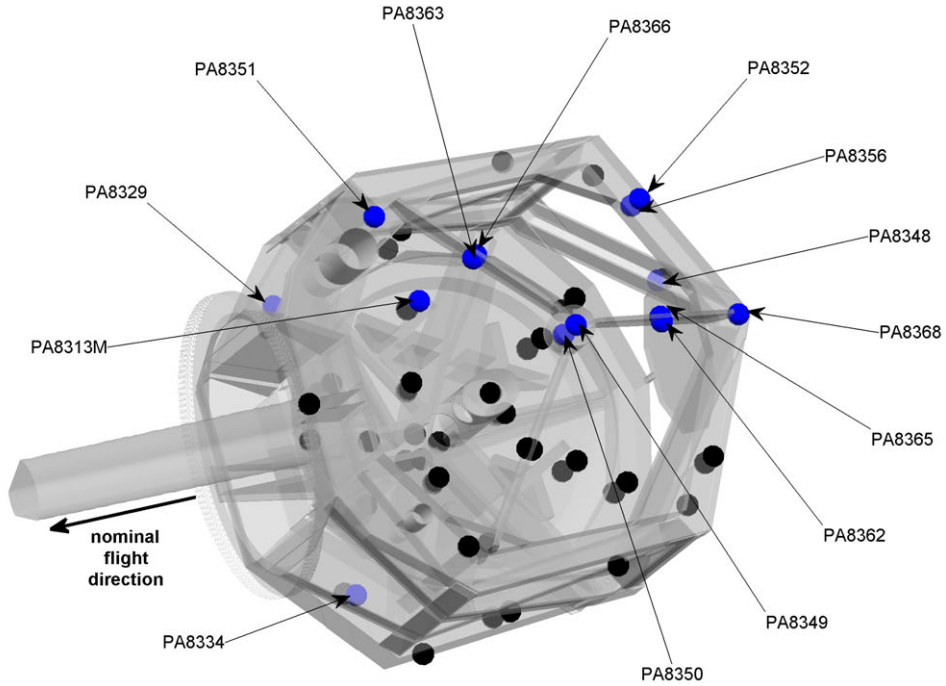
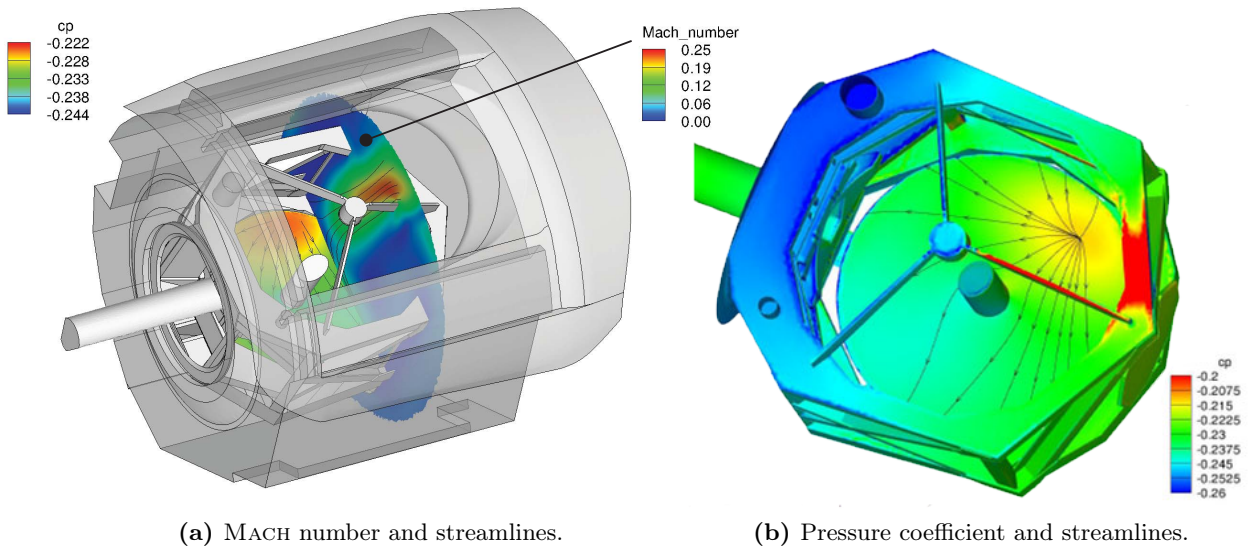


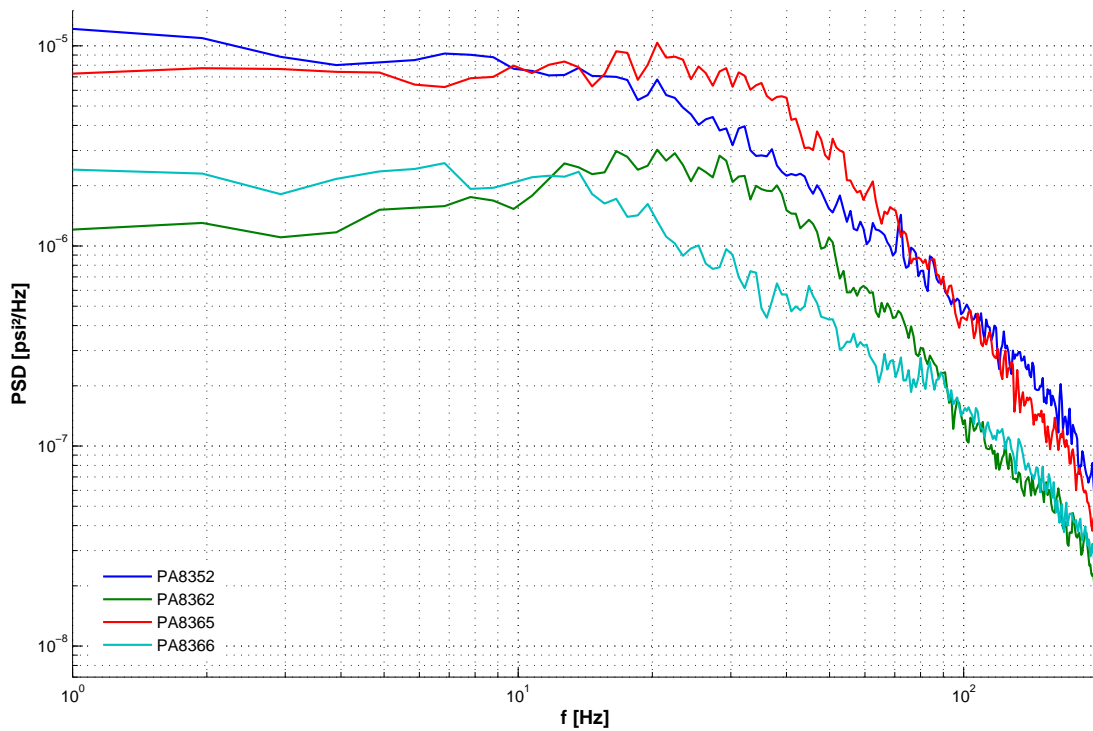
Figure 6.3.: SPL bar chart of telescope sensors for different aperture positions in baseline configuration. FLT026,35,35,41,41\_TC010,25,30,22,30\_AA23-57\_EXP95,100\_ALT35k\_MA0.85.



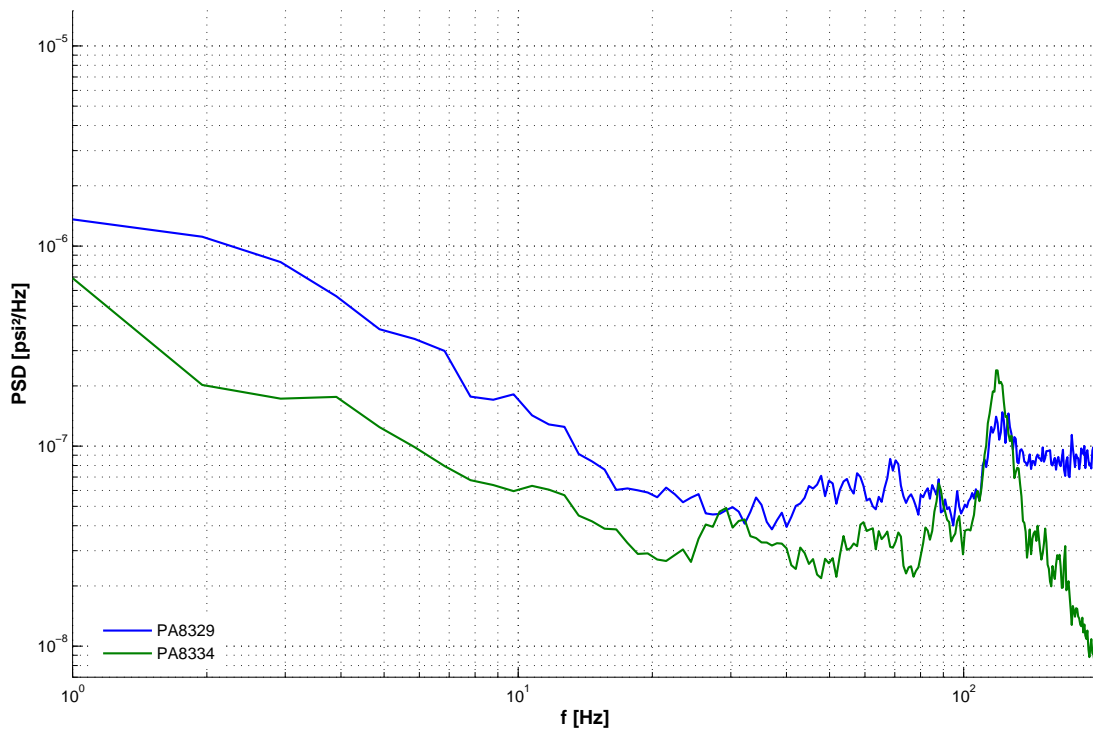
**Figure 6.4.:** Overview of telescope hot spots (blue) for baseline configuration.  
 FLT026,35,35,41,41\_TC010,25,30,22,30\_AA23-57\_EXP95,100\_ALT35k\_MA0.85.



**Figure 6.5.:** TA CFD simulation results, revealing an asymmetrical flow downwash and impingement on the upper right part of the headring and the primary mirror. The simulations have been performed by Schmid [22]. As Engfer mentions in his report [6], there are some discrepancies between the real conditions of the discussed flight test points and those conditions underlying the CFD simulations, which makes an adequate comparison difficult. However, in accordance with Engfer's conclusion, it can be stated that these differences are negligible with regard to *qualitative* considerations.



(a) Hot spots featuring broadband characteristic (PA8352, -62, -65, -66).



(b) Hot spots featuring narrowband characteristic (PA8329, -34).

**Figure 6.6.:** PSD( $f$ ) plot of hot spot sensors, featuring broadband (a) and narrowband (b) characteristic in baseline configuration. Sensors featuring intermediate spectral characteristic can be found in [Figure C.3](#) (p. 85 f.). FLT035\_TC030\_AA40\_TA40\_EXP100\_ALT35k\_MA0.85.

### Power Spectral Density Characteristic

The broadband characteristic of the sensors PA8352, PA8362, PA8365 and PA8366 in [Figure 6.6.a](#) on p. 29 is typical for the situation in which small scale, high energy flow effects supersede acoustic fluctuations. As Engfer [5] points out, using the example of the baffle plate sensors PA8347 and PA8348, fluctuations due to acoustics become obvious in the frequency spectrum only for those sensors which are shielded from flow effects like the downwash or shear layer disturbances. PA8319 and PA8334 belong to this group of sensors either; both of them feature a very prominent peak at approximately 120 Hz that would be invisible in case of superposition with strong, broadband flow effects ([Figure 6.6.b](#) on p. 29). This behavior supports the assumption that the downwash impingement on the primary mirror might be the cause for scattered pressure waves with a dominant frequency around 120 Hz, which are primarily spread towards the forward bulkhead.

The PSD characteristics of the residual hot spots are illustrated in [Figure C.3](#) on p. 85. Their PSD curves can be classified according to their spectral characteristic, ranging between predominantly broadband and predominantly narrowband. As a final conclusion from all PSD plots, the following relationship can be very well seen: the farther away a sensor is from the downwash or shear layer flow and the more shielded it is from their influence, the more narrowband the sensor's PSD characteristic gets so that more acoustic peaks become visible.

### Influence of the Aperture Position

The behavior of all gathered hot spots is vividly compared for different aperture positions in [Figure 6.7](#). Most of the hot spots expectedly issue maximal SPLs for  $\gamma_{AA} = 40^\circ$ , but there are exceptions like PA8334 and PA8352. In fact, no consistent regularity concerning the behavior of hot spots can be detected. In particular, the local acoustic characteristics for different AA positions cannot be derived from the general statement that  $\gamma_{AA} = 40^\circ$  is dominant from an aeroacoustic point of view. It can be merely manifested that, on the one hand, the overall influence of the shear layer and downwash on the telescope is most intense for  $\gamma_{AA} = 40^\circ$ ; however, on the other hand, the complexity of the real flow field, which obviously changes its structure for different AA elevations, cannot be reflected by the few installed sensors in detail. This makes adequate predictions and a full understanding of individual sensors' behavior very difficult.

### Influence of the Operational Point

In order to highlight SOFIA's aeroacoustic behavior for different flight phases, five possible operational points have been selected for comparison (see [Figure 6.9](#) on p. 32). Besides the already discussed baseline configuration, there are relevant points at  $h = 40\,000$  ft and  $h = 42\,000$  ft, which can be reached in an advanced phase of a SOFIA mission, after the aircraft has lost enough fuel. In addition, the points at  $h = 25\,000$  ft and  $h = 15\,000$  ft are important inasmuch as they might be traversed during an obligatory open door landing in case of a possible door mechanism failure.

Apparently, the higher SOFIA flies during nominal operation, the lower the dynamic pressure and thus the noise level gets. If SOFIA descends and must land with an open door, the SPLs clearly increase for several sensors near the shear layer, e.g. PA8362 and PA8365. Even in the worst case, the noise is far below the knock-it-off value of 145 dB, which itself never showed the potential to excite noticeable TA structure oscillations, according to observations in the mission control room [7]. This means that the SOFIA operation with an opened door is safe for all discussed flight points.



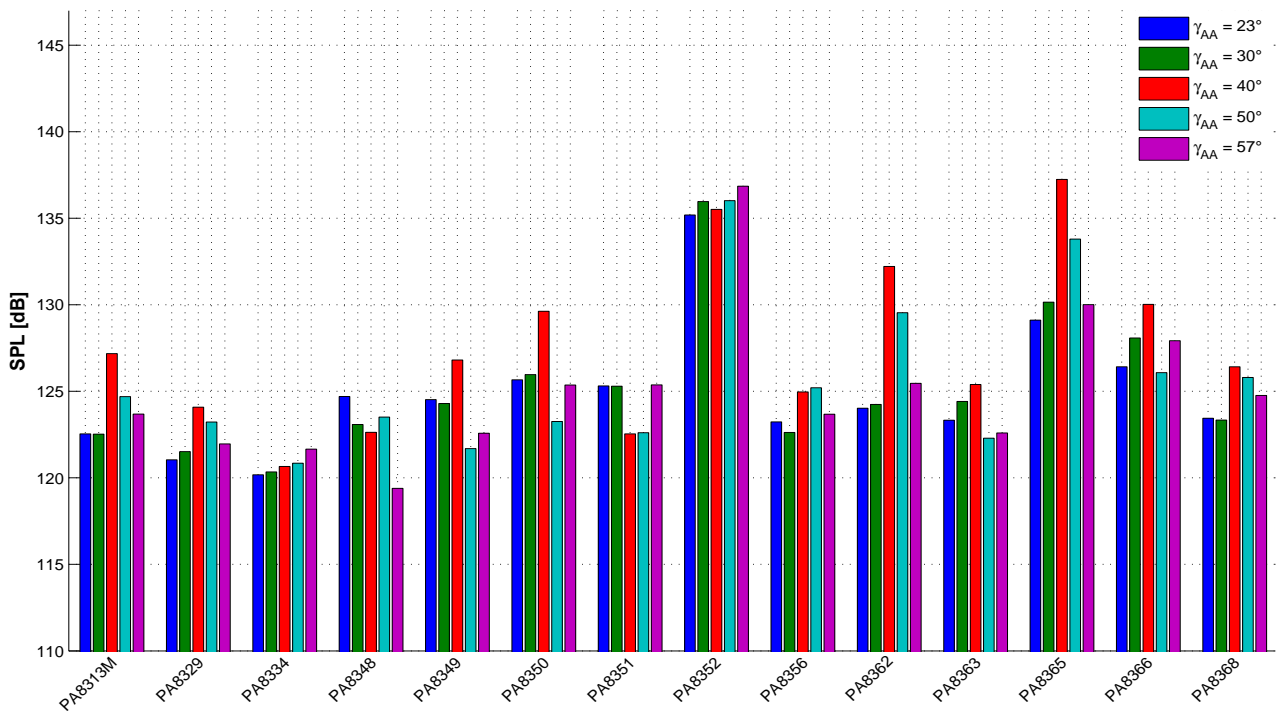


Figure 6.7.: SPL bar chart of TA hot spots (Figure 6.4 on p. 28) for different AA positions in baseline configuration. FLT026,35,35,41,41\_TC010,25,30,22,30\_AA23-57\_EXP95,100\_ALT35k\_MA0.85.

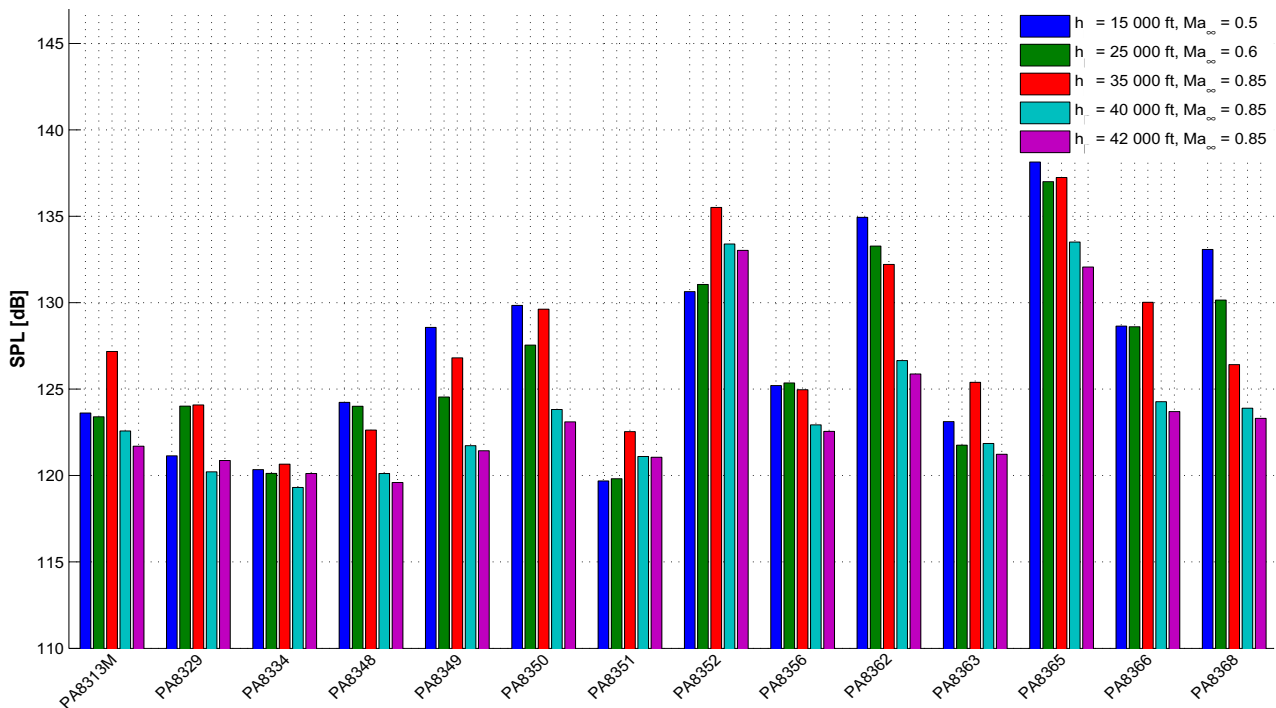
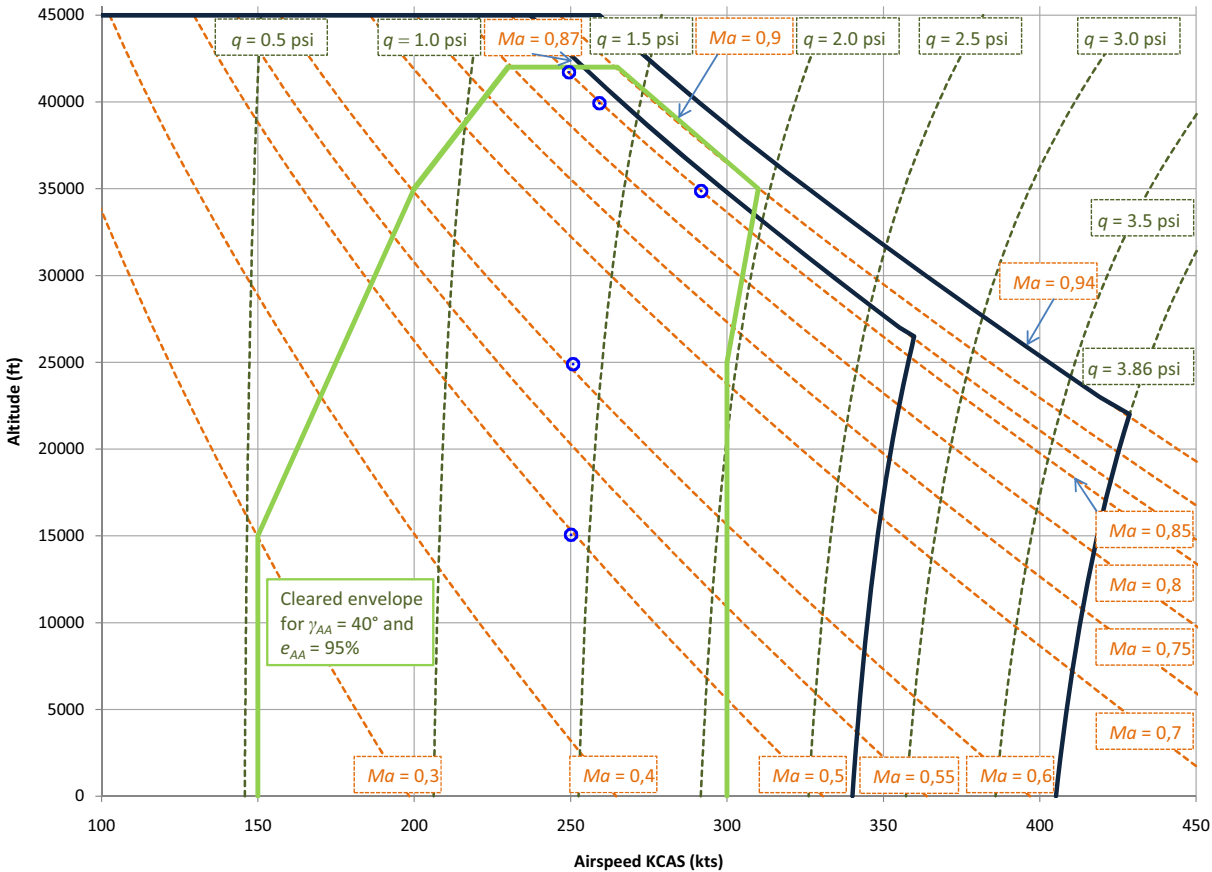


Figure 6.8.: SPL bar chart of TA hot spots (Figure 6.4 on p. 28) for the selected operational points displayed in Figure 6.9 on p. 32. FLT030,33,35,33,33\_TC025,14,30,30,35\_AA40\_EXP95,100\_ALT15k-42k\_MA0.5-0.85.



**Figure 6.9.:** Selected operational points of SOFIA during a science mission.  
 FLT030,33,35,33,33\_TC025,14,30,30,35\_AA40\_EXP95,100\_ALT15-35k\_MA0.5-0.85. © Engfer [5, 6]

### 6.3. Aeroacoustic Parameter Study

This section aims to depict basic dependencies between selected global parameters and the aeroacoustic behavior of the SOFIA configuration. This is done on the basis of the envelope expansion flight test results, which are compared to selected important statements and predictions by Schmid [22]. The latter can be summarized as follows:

- **Effect of decreasing the aperture exposure ( $e_{AA} \searrow$ ).** According to Schmid, there are three main mechanisms which arise from partly covering the telescope cavity:
  1. The effective area through which the kinetic energy can enter the cavity diminishes. A lower aperture exposure reduces the fraction of the kinetic energy that maintains the transient activities inside the cavity so that the pressure fluctuations get weaker.
  2. The aperture ramp has been designed for a nominal SOFIA operation with fully open door. By reducing the aperture exposure, significant deviations of the local flow conditions from the design state are generated. This reduces the efficiency of the mechanism that stabilizes the shear layer.
  3. The higher the ratio of cavity volume to aperture opening area is, the less acoustic energy is emitted into the far field and the more the acoustic damping decreases. Hence, a shrinking aperture exposure reduces the acoustic damping. This leads to rising fluctuation amplitudes and to decreasing peak band widths.

The latter counteracts the firstly mentioned mechanism.

- **Effect of increasing the free stream MACH number ( $Ma_\infty \nearrow$ ).** In particular, there are two MACH number effects that are examined in this section:
  - According to Equation 5.6 on p. 17, the dimensionful ROSSITER frequencies rise with increasing MACH numbers for constant external conditions. Moreover, the spectral characteristic gets more narrowband. In many cases, ROSSITER modes do not even occur below a certain minimal MACH number.
  - In general, rising MACH numbers tend to increase the pressure fluctuation amplitudes.
- **Effect of increasing the free stream dynamic pressure ( $q_\infty \nearrow$ ).** In his work, Schmid assumes that the RMS sound pressure is proportional to the dynamic pressure of the oncoming flow, i. e.

$$p_{rms} \sim q_\infty \quad (6.4)$$

with

$$p_{rms} = p_{ref} \cdot 10^{\frac{L_p}{20}}; \quad p_{ref} = 2 \cdot 10^{-5} \text{ Pa} \quad (6.5)$$

and

$$q_\infty = \rho \cdot c^2 \cdot Ma_\infty^2, \quad (6.6)$$

where  $L_p$  is the sound pressure level and  $c$  is the speed of sound. Schwarz [24] has already examined this assumption by means of the overall pressure sensor average for several selected flight test points with  $\gamma_{AA} = 23^\circ$ . He found that the relationship between  $p_{rms}$  and  $q_\infty$  is roughly linear, but does not constitute a line through origin. This section aims to verify and to extend these findings to almost the whole test point matrix, highlighting the behavior of individual hot spots as well.

An examination of various AA exposure effects and a detailed comparison with the predictions of Schmid [22] is conducted in Section 6.3.1 (p. 34 ff.). Subsequently, the MACH number effect on ROSSITER frequencies is analyzed in Section 6.3.2 (p. 41 ff.). Finally, a regression analysis is performed in Section 6.3.3 (p. 42 ff.) in order to capture the behavior of the RMS sound pressure  $p_{rms}$  for varying aperture exposure  $e_{AA}$ , MACH number  $Ma_\infty$  and dynamic pressure  $q_\infty$ . This section intends to give a profound overview of the situation for representative sensor signals within a big part of the SOFIA flight envelope.

### 6.3.1. Aperture Exposure Effect

The average SPLs of all telescope and cavity sensor groups as well as the overall SPL averages for different aperture exposures can be found in Figure 6.10. It is obvious that the sensors on the spiderarms and aft bulkhead generally detect the most energetic noise, being most exposed to the high energy flow. Both sensor groups show a clear upward trend for an increasing aperture exposure. This supports Schmid’s statement that a larger cavity opening boosts the kinetic energy transfer between the outer flow and the cavity interior. A similar behavior is exhibited by the suncover, indicating that the downwash, which originates from the shear layer, gains more kinetic energy due to higher aperture exposures as well.

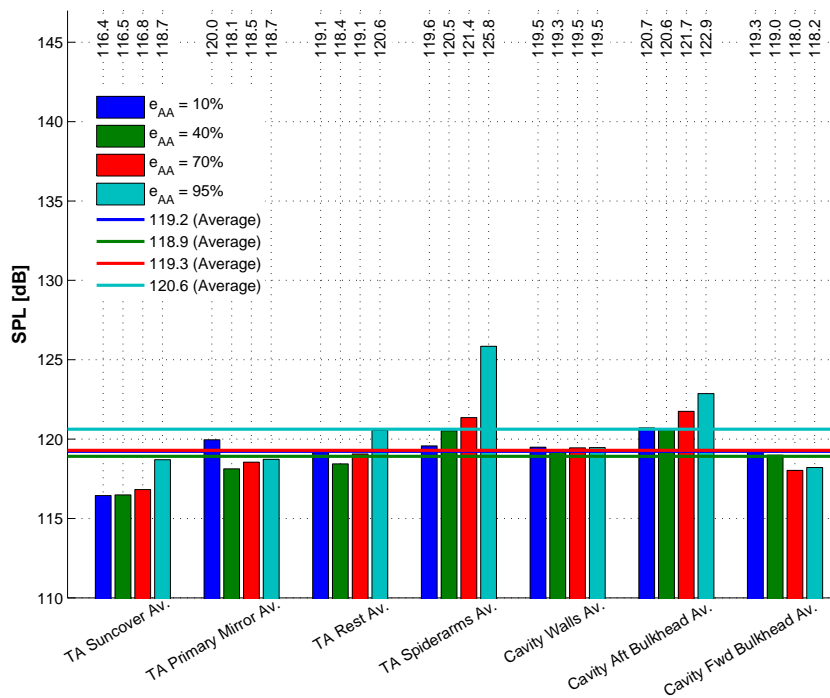


**Figure 6.10.:** SPL bar chart of the averages of all sensor groups for different aperture exposures. FLT033\_TC020-23\_AA40\_TA40\_EXP10-95\_ALT35k\_MA0.85.

A more detailed illustration of telescope and cavity hot spot<sup>4</sup> behavior can be found in Figure 6.11 and Figure 6.12 on p. 35 respectively. Almost all TA hot spots yield a consistent upward trend for increasing aperture exposure, whereas there are several exceptions in this regard among the cavity

<sup>4</sup>The locations of the TA hot spots are highlighted in Figure 6.4 on p. 28. An analogous illustration of the cavity hot spots can be found in Figure C.4 on p. 87.

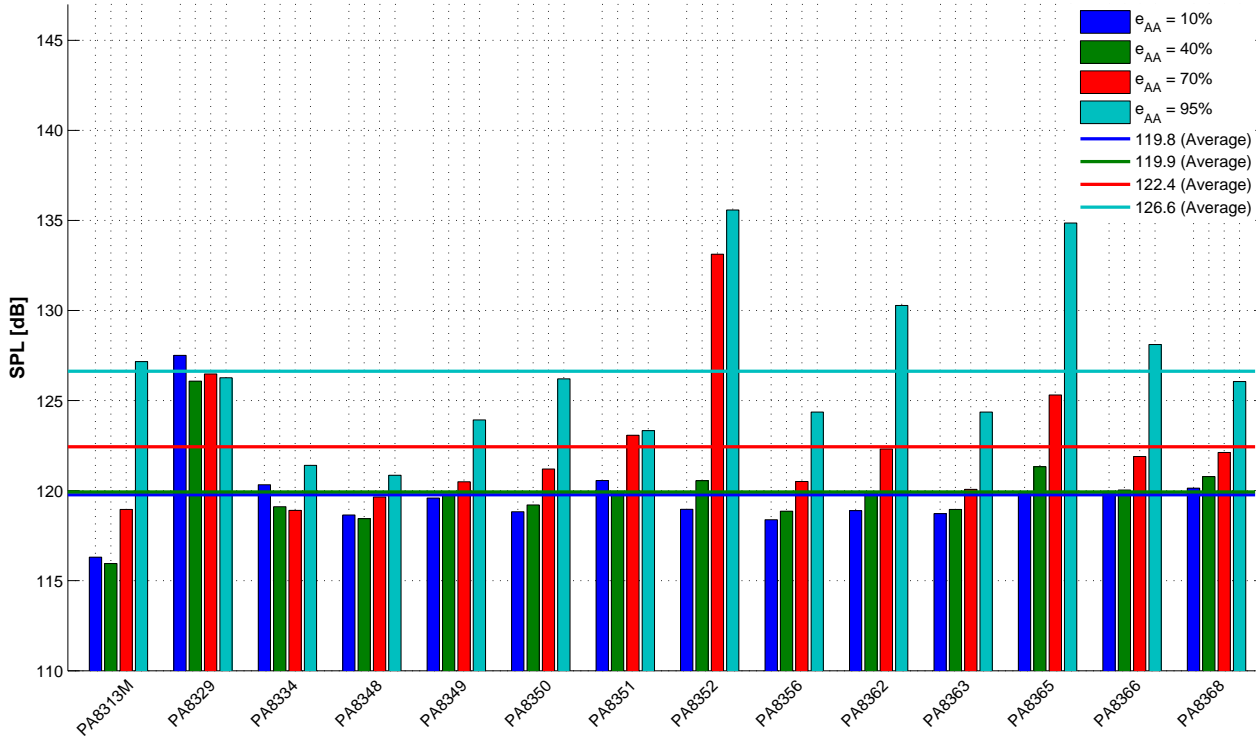


Figure 6.11.: SPL bar chart of TA hot spots (see Figure 6.4 on p. 28) for different aperture exposures. FLT033\_TC020-23\_AA40\_TA40\_EXP10-95\_ALT35k\_MA0.85.

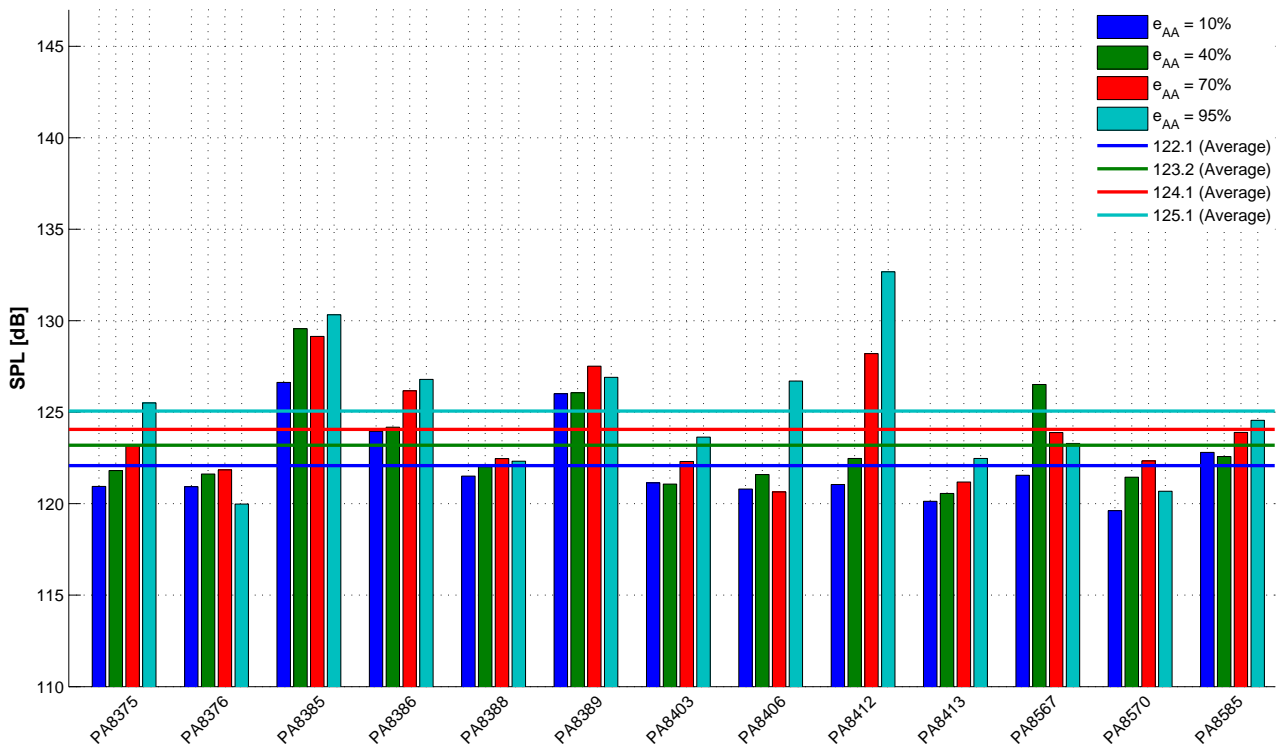
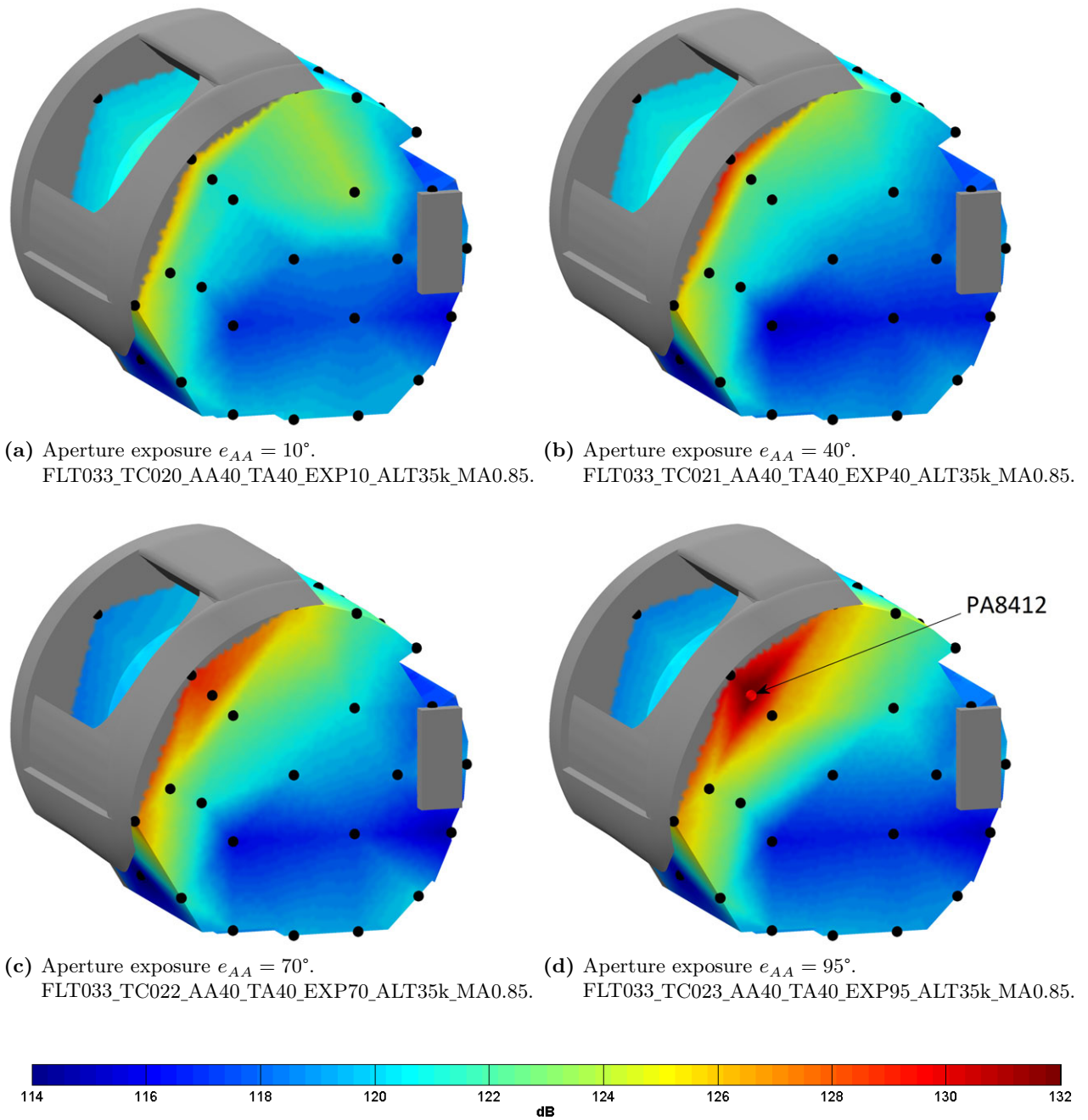


Figure 6.12.: SPL bar chart of cavity hot spots (see Figure C.4 on p. 87) for different aperture exposures. FLT033\_TC020-23\_AA40\_TA40\_EXP10-95\_ALT35k\_MA0.85.



**Figure 6.13.:** SPL contour plot of the cavity for different aperture exposures. The calculated SPL values of the pressure sensor signals are linearly interpolated along the cavity surface. The area around the sensor PA8412 is subject to the highest energy transfer in any regarded case and undergoes the most important noise level changes if the AA exposure is varied (mechanism № 1 on p.33). In contrast, the shielded parts of the cavity, e.g. the forward bulkhead, are not affected by the kinetic energy transfer itself; they register lower SPLs for higher AA exposures due to the increased acoustic damping (mechanism № 3).

hot spots. These exceptions show maximum values for minimal or intermediate aperture exposures. The most probable reason is that these sensors are more shielded behind structural components and thus react more sensitively to the reduction of the acoustic damping rather than to the weaker energy transfer in case of a partly closed cavity. In short, this means that in these cases the previously mentioned mechanism № 3<sup>5</sup> compensates or even outweighs the mechanism № 1<sup>5</sup>. However, the SPL values of these hot spots never reach a high level. Examples for the discussed behavior are given by the TA sensor PA8329 or the cavity sensors PA8376 and PA8567. In addition, it can be generally stated that the deviation of the highly complex flow field from the design state (mechanism № 2<sup>5</sup>) does not seem to cause serious shear layer destabilizations. Otherwise, significantly higher noise would be registered for intermediate or small aperture openings at least by few sensors. Holistically seen, the average SPL values suggest that the effect of kinetic energy transfer (mechanism № 1<sup>5</sup>) dominates for both the telescope and the cavity surfaces.

The contour plots in Figure 6.13 on p. 36 provide a vivid picture of how the SPL distribution along the cavity surface changes with the aperture exposure. The area on the aft bulkhead under the aperture ramp around the sensor PA8412 is particularly remarkable. Not only the most kinetic energy is transported here in any analyzed case, but also the strongest noise level augmentation is noticeable if the aperture is increasingly exposed to the outer flow. In contrast, a closer look at the forward bulkhead reveals that the opposite effect occurs here. This cavity surface is shielded from flow effects at all times and registers slightly lower noise levels for higher aperture exposures merely due to the stronger acoustic damping inside the cavity.

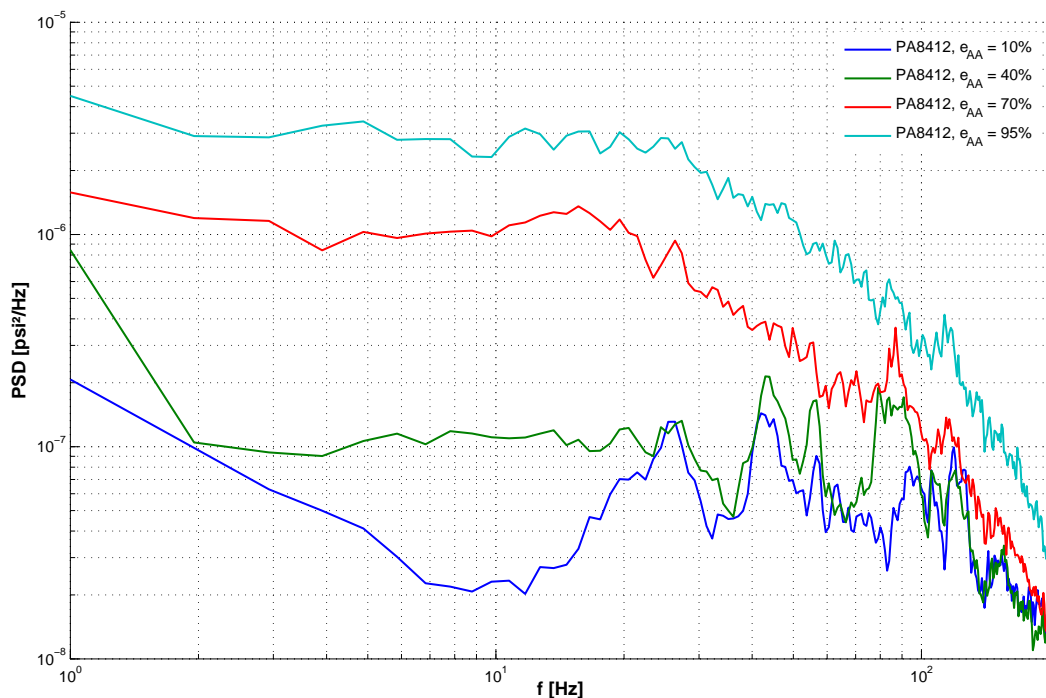


**Figure 6.14.:** PSD( $f$ ) plot of the cavity aft bulkhead sensor PA8412 for different aperture exposures. FLT033\_TC020-23\_AA40\_TA40\_EXP10-95\_ALT35k\_MA0.85.

Figure 6.14 demonstrates, how the signal of the sensor PA8412 behaves in the frequency spectrum. The PSD plots for the aperture exposures  $e_{AA} = 10\%$  and  $e_{AA} = 40\%$  exhibit prominent acoustic

<sup>5</sup>For explanation of the mechanisms, see “effect of decreasing aperture exposure” on p. 33.

peaks (e. g. 25 Hz, 42 Hz), which are dwarfed by the high energy flow effects if the aperture is exposed to a higher extent. In case of maximal exposure, the sensor’s characteristic is entirely broadband.

Having analyzed the baseline altitude  $h = 35\,000$  ft so far, it is now necessary to switch to a higher altitude in order to compare the flight test results with CFD simulation data of Schmid [22]. First, it needs to be pointed out that there are two main differences restraining the comparability:

1. The performed simulations focus on an operational altitude of  $h = 41\,000$  ft, whereas the closest available flight test point has been accomplished at  $h = 42\,000$  ft.
2. There are slight inconsistencies with regard to the analyzed aperture exposures:

	Analyzed aperture exposures $e_{AA}$ [%]			
CFD simulations [22]	10	50	70	100
SOFIA flight tests	10	40	70	95

**Table 6.2.:** Regarded aperture exposures in CFD simulations and flight tests.

Nevertheless, the differences can be considered negligible for a qualitative comparison. In 42 000 ft the turbulence level as well as the dynamic pressure are less important than in 41 000 ft so that the CFD simulation results are rather conservative (cp. Engfer [6]).

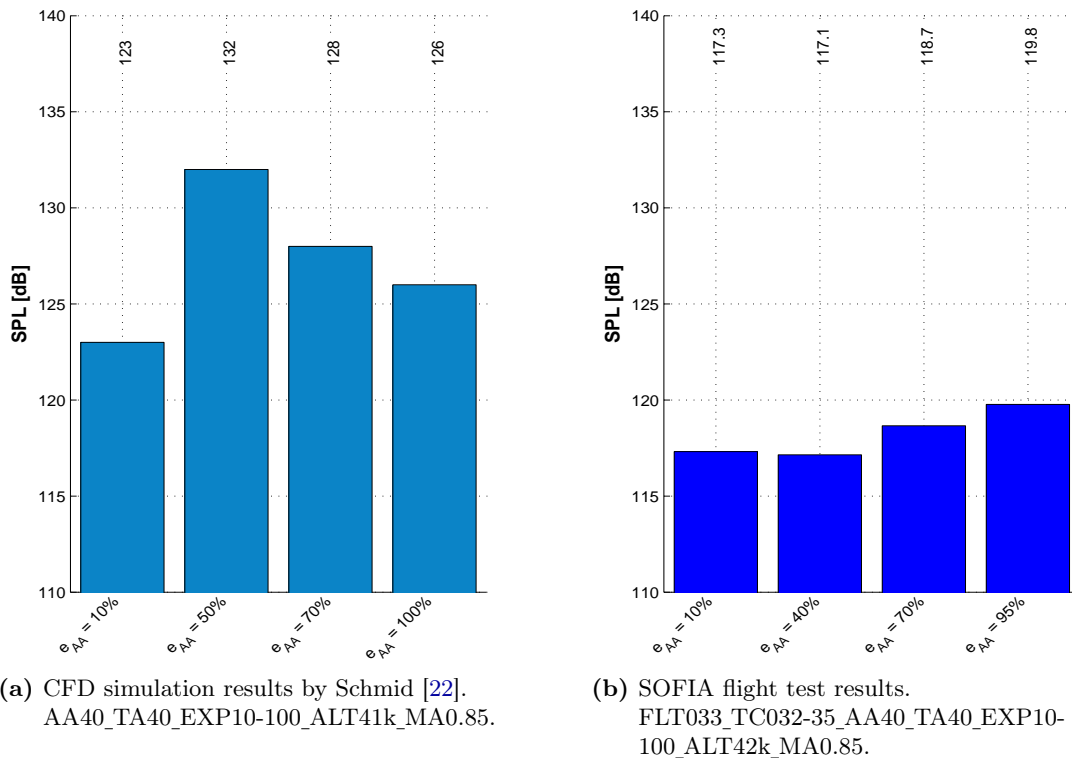


**Figure 6.15.:** SPL bar chart of the TA sensors average for different aperture exposures.

In Figure 6.15, the average SPLs for all TA sensors as per Schmid’s simulation results (left) are compared with the corresponding values derived from flight tests (right). According to Schmid, the

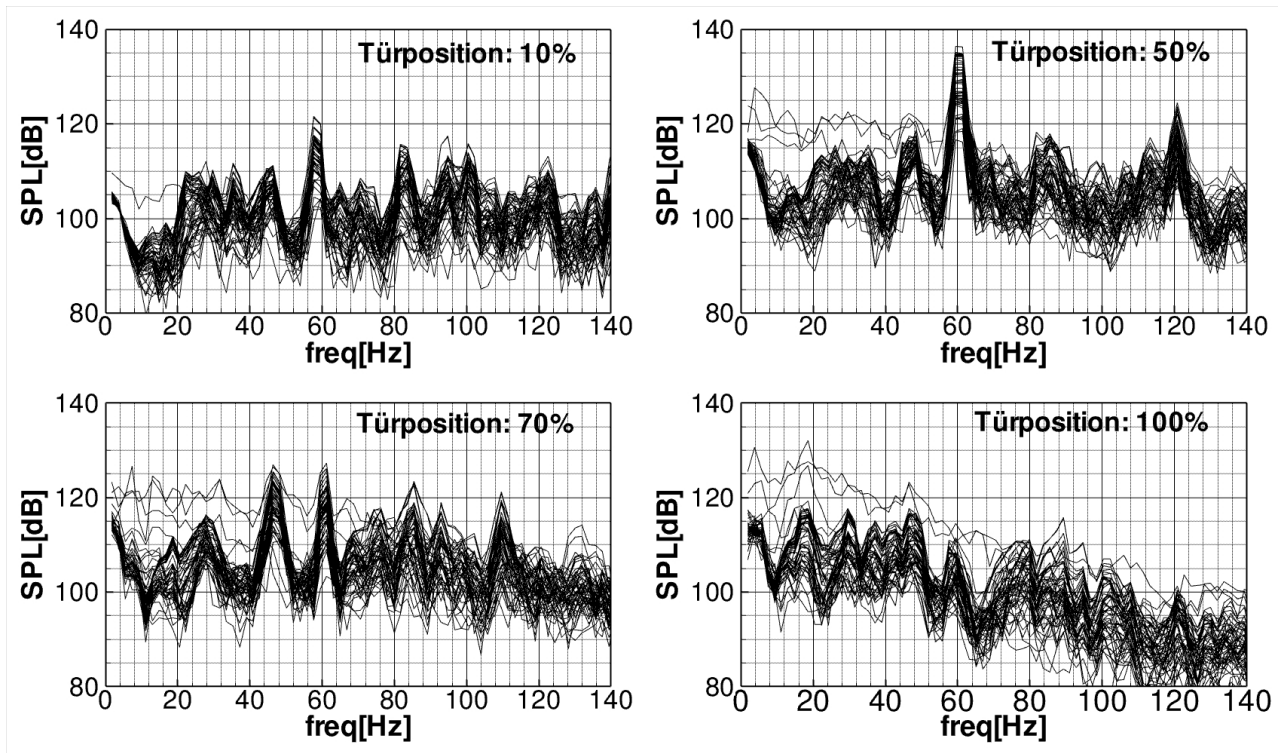


least important SPL value is reached for  $e_{AA} = 10\%$ , which is smaller than the value for full exposure by 3 dB. In this case, those effects dominate which result from the reduction of the effective area for kinetic energy transfer (mechanism № 1<sup>5</sup>). Furthermore, Schmid states that the intermediate aperture exposures lead to higher SPLs because the remaining two mechanisms<sup>5</sup> dominate.

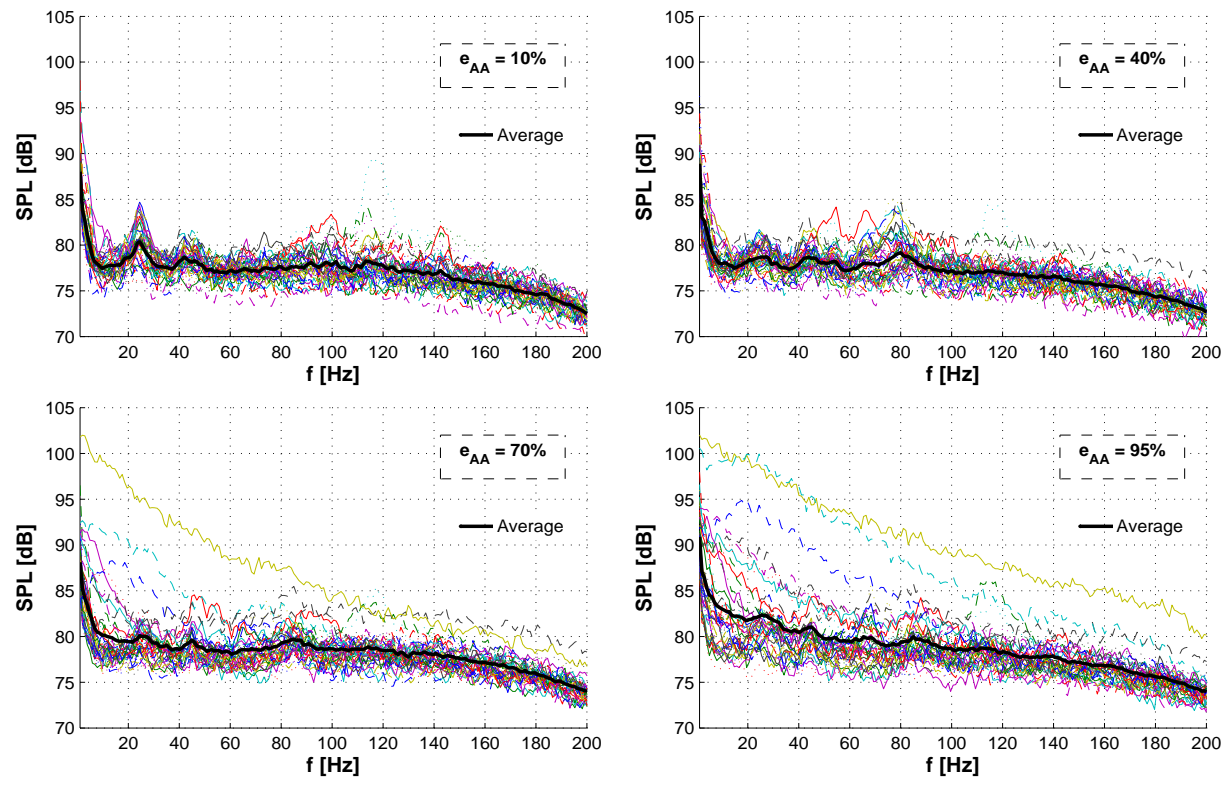
This behavior cannot be confirmed by the flight test results. First, a general upward tendency for an increasing aperture exposure can be observed during the real flight. As already demonstrated for  $h = 35\,000$  ft, there is some weak reverse influence due to acoustic damping variation, but the effect of kinetic energy transfer clearly prevails in any case. Second, all observed SPLs are considerably lower than predicted. These differences become more comprehensible considering the pressure spectra in [Figure 6.16](#) on p. 40. The CFD simulations predict numerous strong acoustic modes (e. g. 45 Hz, 60 Hz) for all analyzed aperture exposures in general and for the intermediate exposures in particular. In contrast, the flight test results yield a tiny peak around 25 Hz for  $e_{AA} = 10\%$  and barely noticeable acoustic events for higher aperture exposures due to the more energetic broadband noise. In addition, it stands out that the curves reflecting the flight tests go far below their simulation-based counterparts.

The reasons for these discrepancies are subject to extensive investigation by the aeroacoustic team of the DSI at this time (2011). On the one hand, it is attempted to refine the simulation model in order to capture previously unconsidered details of the cavity geometry that might essentially contribute to noise damping and absorption. For instance, the LFD is equipped with a perforated plate on the inside, which is suspected to be one of the main factors. On the other hand, possible reasons are also searched within the CFD approach itself. Various numerical parameters as well as new simulation-specific instruments like matrix dissipation or finer grids are examined [7].

Altogether, it can be stated that the simulation-based predictions are considerably more pessimistic than the flight test measurements. Evidently, the aperture ramp and the cavity have been well designed from an aeroacoustic point of view, since no serious acoustic resonances are excited in any regarded case during operational flight.



(a) CFD simulation results by Schmid [22]. AA40\_TA40\_EXP10-100\_ALT41k\_MA0.85.



(b) SOFIA flight test results. FLT033\_TC032-35\_AA40\_TA40\_EXP10-100\_ALT42k\_MA0.85.

Figure 6.16.: SPL frequency spectra of all TA sensors for different aperture exposures.

### 6.3.2. Mach Number Effect on Characteristic Frequencies

In order to analyze the influence of the flight MACH number on characteristic peaks in the frequency spectrum, the microphone PA8583M on the aft bulkhead has been examined at the altitude  $h = 35\,000$  ft. For the four tested MACH numbers  $Ma_\infty = 0.69, 0.81, 0.85, 0.89$  the lowest possible common aperture exposure of  $e_{AA} = 40^\circ$  has been selected to suppress unfavorable broadband noise (cp. Figure 6.14 on p. 37). The resulting PSD curves are shown in Figure 6.17.

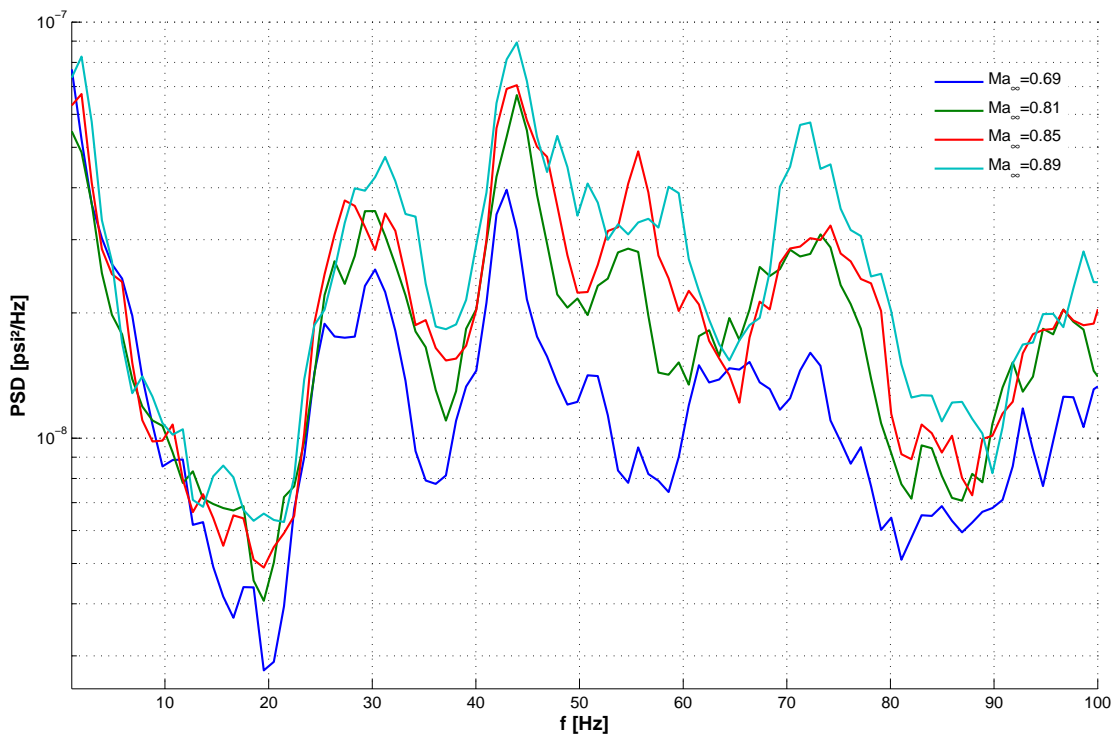


**Figure 6.17.:** PSD( $f$ ) plot of the cavity aft bulkhead microphone PA8583M for the altitude  $h = 35\,000$  ft and different MACH numbers.  
FLT033\_TC016,18,21,24\_AA40\_TA40\_EXP40\_ALT35k\_MA0.69-0.89.

As suggested by Schmid [22], the focus is on the frequency range 0-100 Hz, since higher frequent modes play a negligible role with regard to possible structural excitation. First, it can be confirmed for the displayed conditions that a rising MACH number increases the signal's PSD through almost the whole frequency range. This means that almost all harmonic oscillation components of the signal feature increased amplitudes.

Second, as it can be seen in Figure 6.18 on p. 42, the characteristic peaks apparently have a slight tendency to drift towards higher frequencies if the MACH number is augmented. This can be confirmed only qualitatively because the peaks in Figure 6.17 can be merely identified as *small frequency bands with high PSD values* rather than as discrete points in the diagram. Compared to the ROSSITER frequencies as per Equation 5.6 on p. 17 (blue curves in Figure 6.18), it becomes visible that the 4th peak seems to match the 3rd mode for all regarded MACH numbers, whereas the remaining peaks are mainly located apart from the ROSSITER curves. Moreover, the upward tendency of all peaks seems to be weaker than suggested by the ROSSITER formula.

These discrepancies can be explained by the fact that the ROSSITER equation 5.6 on p. 17 is merely

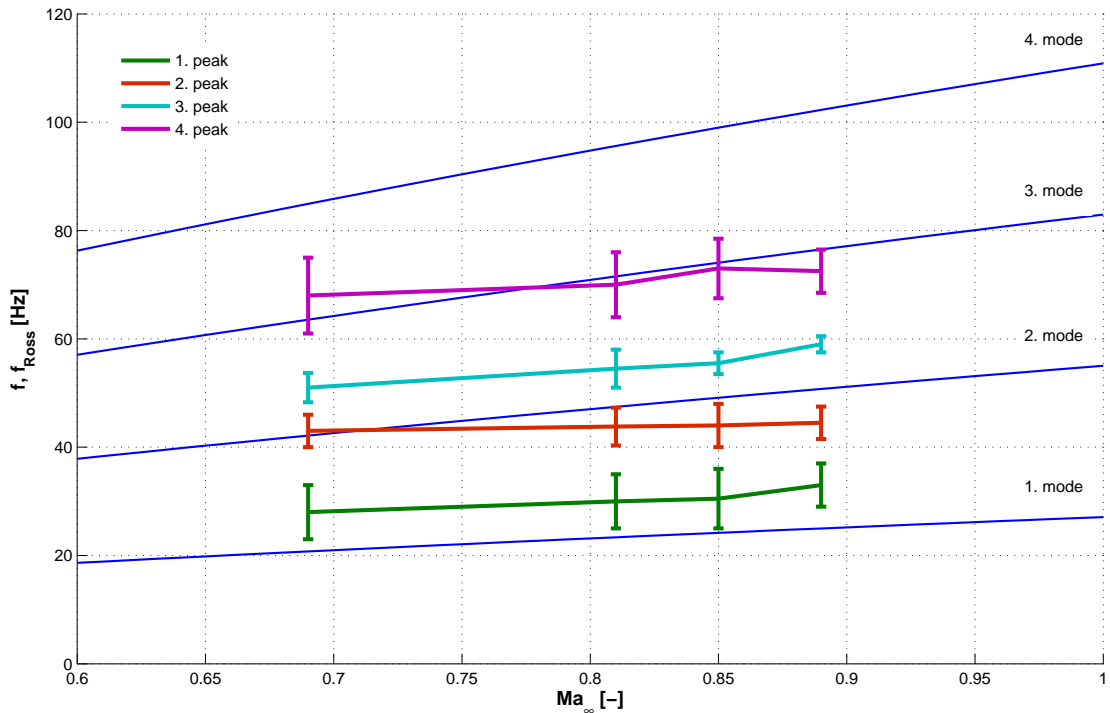


**Figure 6.18.:** Comparison of the first four ROSSITER modes (blue curves) with observed peak frequencies of the microphone PA8583M for  $h = 35\,000$  ft and the MACH numbers  $Ma_\infty = 0.69, 0.81, 0.85, 0.89$ . The ROSSITER modes are computed by means of Equation 5.6 on p. 17 for  $K = 0.47$ ,  $\gamma = 0.03$ ,  $L = 3.4$  m and the speed of sound  $c = 297$  m/s, as suggested in the *control room guide* [23]. The peaks are represented by small frequency bands read off from Figure 6.17 on p. 41. The center points of these bands are connected by straight lines to indicate the respective tendencies. FLT033\_TC016,18,21,24\_AA40\_TA40\_EXP40\_ALT35k\_MA0.69-0.89.

suitable for two-dimensional, rectangular cavities and does not make allowance for the complex three-dimensional SOFIA geometry. Furthermore, the utilized values  $K = 0.47$  and  $\gamma = 0.03$  are based on external empiric data and the use of the sound speed  $c = 297$  m/s assumes the *International Standard Atmosphere (ISA)* [23]. Both might be not well applicable to the SOFIA configuration during the flight FLT033. Besides that, the unavoidable unsteadiness of global parameters and the time window selection may have a disturbing influence as well.

Nevertheless, in accordance with Schmid's statement [22], the peak frequency bands in Figure 6.18 suggest that higher MACH numbers generally make the PSD characteristic more narrowband. This becomes obvious especially when comparing the peak band widths for  $Ma_\infty = 0.69$  and  $Ma_\infty = 0.89$ .

### 6.3.3. Regression Analysis of Aeroacoustic Pressure Fluctuations

In order to gain a vivid and all-embracing view of the dependency between aeroacoustic noise and important global parameters, a linear regression analysis has been performed for the critical aperture position  $\gamma = 40^\circ$ . This means that the relationship between selected output variables (response variables) and independent input variables (predictors) is approximated by means of statistical methods being applied to the flight test point matrix.

Instead of investigating the highly complex physical mechanisms and deriving mathematical models,

the so-called *black box method* is used (see Figure 6.19). It utilizes merely the empiric test data in order to find the *effect function* or *regression formula*, which describes the influence of the input variables on the behavior of the response variables by means of a simple algebraic formula. This formula also allows to approximately predict the value of the output variables for any input variable combination [2].

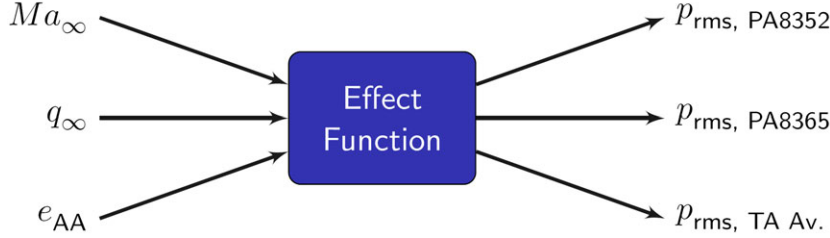


Figure 6.19.: Scheme of the black box method.

As it can be seen in Figure 6.19, this thesis regards the MACH number  $Ma_\infty$ , dynamic pressure  $q_\infty$  and aperture exposure  $e_{AA}$  as independent predictors, whereas the RMS sound pressure of the sensors PA8352, PA8365 and the TA average (TA Av.) serve as representative response variables.

For each response variable (index  $i$ ) the polynomial approach

$$p_{\text{rms},i} = \mathbf{x} \cdot \boldsymbol{\beta}_i^\top; \quad i \in \{\text{PA8352, PA8365, TA Av.}\} \quad (6.7)$$

is used as the sought regression formula, in which

$$\mathbf{x} = (1 \quad Ma_\infty \quad q_\infty \quad e_{AA} \quad Ma_\infty^2 \quad q_\infty^2 \quad e_{AA}^2 \quad Ma_\infty^3 \quad q_\infty^3 \quad e_{AA}^3 \quad \dots \quad Ma_\infty \cdot q_\infty \quad Ma_\infty \cdot e_{AA} \quad q_\infty \cdot e_{AA} \quad Ma_\infty \cdot q_\infty \cdot e_{AA}) \quad (6.8)$$

is a row vector of constant, linear, quadratic, cubic and mixed predictor functions, capturing the main and interaction effects, whereas

$$\boldsymbol{\beta}_i = (\beta_{i,1} \quad \beta_{i,2} \quad \beta_{i,3} \quad \dots \quad \beta_{i,14}) \quad (6.9)$$

represents the unknown vector of linear coefficients.

Important test points (observations) used to determine and verify the regression formula are displayed in Figure 6.20. Each red dot represents four test points with the same MACH number and altitude but different aperture openings according to Table 6.2 on p. 38. Each purple dot stands for two test points with different aperture openings (see legend). The four blue dots mark those single points which are not included in the regression analysis, but serve to verify the accuracy of the derived effect function (cp. Table 6.4 on p. 45).

Therefore, given a total number of 38 relevant observations  $(Ma_{\infty,1}, q_{\infty,1}, e_{AA,1}, p_{\text{rms},i,1}), \dots, (Ma_{\infty,38}, q_{\infty,38}, e_{AA,38}, p_{\text{rms},i,38})$ , the linear regression model becomes an overdetermined 38-by-14 system of equations for each of the three response signals PA8352, PA8365 and TA average respectively.

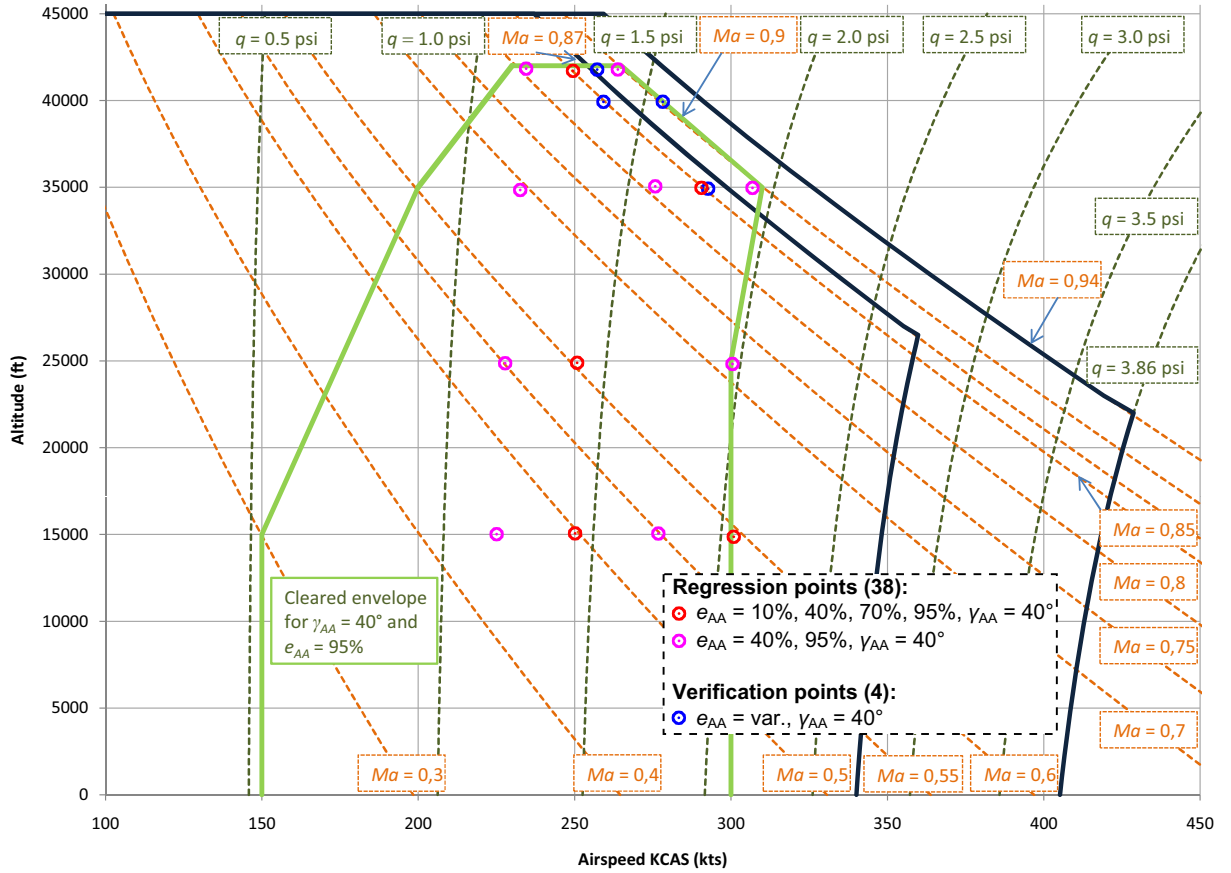


**Figure 6.20.:** Test point matrix of the regression analysis for  $\gamma_{AA} = 40^\circ$ . 38 test points are included in the regression analysis and 4 points serve to verify the accuracy of the determined effect function. © Engfer [5, 6]

$$\underbrace{\begin{pmatrix} p_{rms,i} \\ p_{rms,i,1} \\ p_{rms,i,2} \\ \vdots \\ p_{rms,i,38} \end{pmatrix}}_{\mathbf{p}_{rms,i}} = \underbrace{\begin{pmatrix} 1 & Ma_{\infty,1} & \cdots & Ma_{\infty,1} \cdot q_{\infty,1} \cdot e_{AA,1} \\ 1 & Ma_{\infty,2} & \cdots & Ma_{\infty,2} \cdot q_{\infty,2} \cdot e_{AA,2} \\ \vdots & \vdots & \ddots & \vdots \\ 1 & Ma_{\infty,38} & \cdots & Ma_{\infty,38} \cdot q_{\infty,38} \cdot e_{AA,38} \end{pmatrix}}_{\mathbf{X}} \cdot \underbrace{\begin{pmatrix} \beta_{i,1} \\ \beta_{i,2} \\ \vdots \\ \beta_{i,14} \end{pmatrix}}_{\boldsymbol{\beta}_i^T} + \underbrace{\begin{pmatrix} \epsilon_{i,1} \\ \epsilon_{i,2} \\ \vdots \\ \epsilon_{i,38} \end{pmatrix}}_{\boldsymbol{\epsilon}_i};$$

$i \in \{\text{PA8352, PA8365, TA Av.}\}$  (6.10)

$\mathbf{X}$  is the so-called *design matrix* of the system. The columns of  $\mathbf{X}$  are the terms of the model evaluated at the predictors. The mathematical challenge is to fit the model to the observation data by solving it for the coefficient vector  $\boldsymbol{\beta}_i$ . This has been performed with the aid of the `regress` function in MATLAB<sup>®</sup>, which minimizes the norm of the residual vector  $\boldsymbol{\epsilon}_i$  over all elements of  $\boldsymbol{\beta}_i$  [14].

If the input variables are inserted in the effect function 6.7 on p. 43 with the units

- $[Ma] = 1$
- $[q_\infty] = 10^5 \text{ Pa}$
- $[e_{AA}] = 100 \%$ ,

then the respective coefficient vectors  $\beta_i$  for the three regarded output variables are given in [Table 6.3](#). The unit of the resulting output values is  $[p_{rms,i}] = 100 \text{ Pa}$  respectively.

Output signal	constant	linear			quadratic		
	$\beta_{i,1}$	$\beta_{i,2}$	$\beta_{i,3}$	$\beta_{i,4}$	$\beta_{i,5}$	$\beta_{i,6}$	$\beta_{i,7}$
<b>PA8352</b>	-1.88	-9.24	120.65	-3.50	15.21	-1042.04	12.02
<b>PA8365</b>	-2.53	20.78	-39.01	0.56	-31.76	238.90	-5.37
<b>TA Av.</b>	1.13	-0.23	-26.05	-0.12	0.17	273.65	0.07

Output signal	cubic			mixed			
	$\beta_{i,8}$	$\beta_{i,9}$	$\beta_{i,10}$	$\beta_{i,11}$	$\beta_{i,12}$	$\beta_{i,13}$	$\beta_{i,14}$
<b>PA8352</b>	-7.67	3142.17	-7.38	-10.65	-1.95	-17.87	33.31
<b>PA8365</b>	16.14	-572.37	5.20	2.37	-1.70	26.37	-7.40
<b>TA Av.</b>	0.09	-865.69	0.04	-2.34	-0.05	0.37	0.62

( $[p_{rms,i}] = 100 \text{ Pa}$ ,  $[q_\infty] = 10^5 \text{ Pa}$ ,  $[e_{AA}] = 100 \%$ ,  $\beta_{i,1}, \dots, \beta_{i,14}$  accordingly)

**Table 6.3.:** Solution of the regression model.

As it turns out in [Table 6.4](#), this effect function is suitable to predict the aeroacoustic noise at intermediate points in the flight test matrix. The right four columns of [Table 6.4](#) stand for the previously mentioned verification points (see [Figure 6.20](#) on p. 44). A very good prediction accuracy is achieved for the RMS sound pressure of PA8365. Here, the deviation between measured and predicted values ranges from  $-4.1 \%$  to  $0.9 \%$ . In contrast, the relative deviations for PA8352 and the TA average are noticeably higher. The output values corresponding to PA8352 seem to be underestimated except for the test point FLT033\_TC030, whereas the output values of the TA average seem to be generally overestimated. However, if the  $p_{rms}$  values are transformed into SPLs as per [Equation 6.5](#) on p. 33, even in the worst case the absolute deviations do not exceed 0.8 dB. This error is smaller than the possible value variance of  $\pm 1 \text{ dB}$  which might occur due to alternative time window selection by the user (see [Section 6.1](#) on p. 21 ff.)

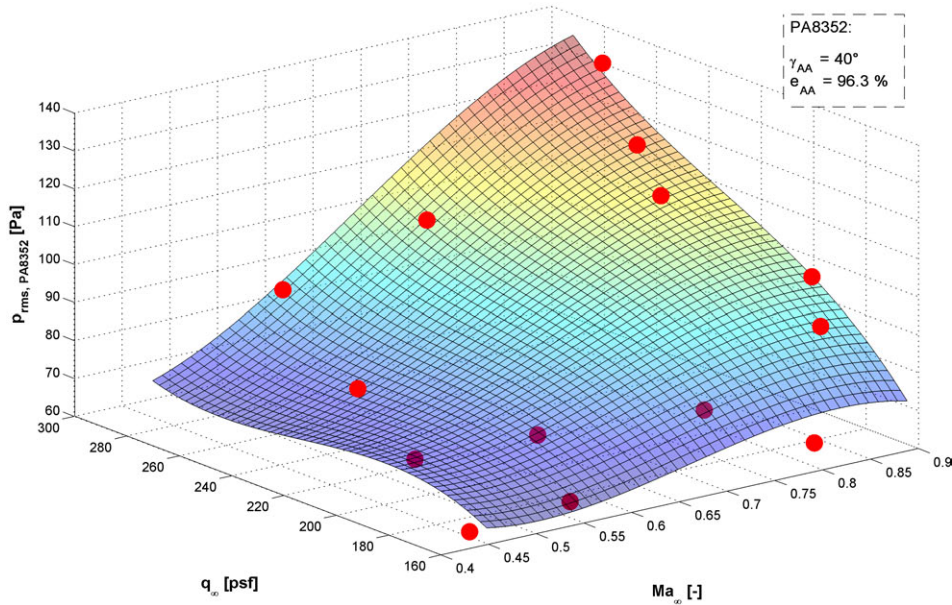
Test Point	FLT, TC	35, 30	33, 30	33, 31	33, 37
		$Ma_\infty [-]$	0.85	0.848	0.889
	$q_\infty [\text{psf}]$	250	198	216.5	187.5
	$e_{AA} [\%]$	100	96.5	96.5	96.6
PA8352	Measured $p_{rms}$ [Pa]	119.32	93.46	109.71	97.41
	Predicted $p_{rms}$ [Pa]	108.62	96.78	104.24	91.73
	Relative deviation [%]	-9.0	+3.6	-5.0	-5.8
PA8365	Measured $p_{rms}$ [Pa]	145.62	94.76	102.68	84.37
	Predicted $p_{rms}$ [Pa]	146.25	90.91	102.32	85.15
	Relative deviation [%]	+0.4	-4.1	-0.4	+0.9
TA Av.	Measured $p_{rms}$ [Pa]	23.11	18.31	19.40	18.77
	Predicted $p_{rms}$ [Pa]	24.02	19.54	21.00	19.01
	Relative deviation [%]	+3.9	+6.7	+8.2	+1.3

**Table 6.4.:** Verification of the regression formula.

Most of the test points have been performed with a nominal aperture exposure of  $e_{AA} = 95\%$ . In reality, they feature slight exposure fluctuations around the overall average of  $e_{AA} = 96.3\%$ . In order to visualize the regression formula, the aperture exposure is kept constant at this value, whereas the RMS sound pressure is plotted versus the MACH number and dynamic pressure for all regarded output variables in Figure 6.21. The red dots symbolize the real flight observations which the regression formula is based upon. Considering the headinging sensor PA8352 (Figure 6.21.a), neither for a constant minimal MACH number  $Ma_\infty$  nor for constant minimal dynamic pressure  $q_\infty$  a clear tendency of  $p_{rms}$  can be detected if the other respective parameter is varied. However, a steep increase of the output value is observable if both parameters are increased at the same time or if at least one of them is not close to the regarded range minimum. This means that  $Ma_\infty$  and  $q_\infty$  feature a strong interaction and amplify each others effects.

A completely different behavior is exhibited by the spiderarm sensor PA8365 (Figure 6.21.b). Indeed, an approximately linear relationship between  $q_\infty$  and  $p_{rms}$  can be observed, as assumed by Schmid [22]. However, the noise level does not rise with increasing MACH numbers; it rather diminishes in this case. This is a remarkable finding. The shear layer influence on PA8365 apparently decreases for higher MACH numbers, which might indicate that the disturbances originating from the shear layer are weaker or less focused on PA8365. In contrast, the downwash at PA8352 seems to gain additional energy if  $Ma_\infty$  is increased. A probable reason is that the part of the shear layer which turns into the downward jet has more kinetic energy and results in a stronger impingement on the headinging.

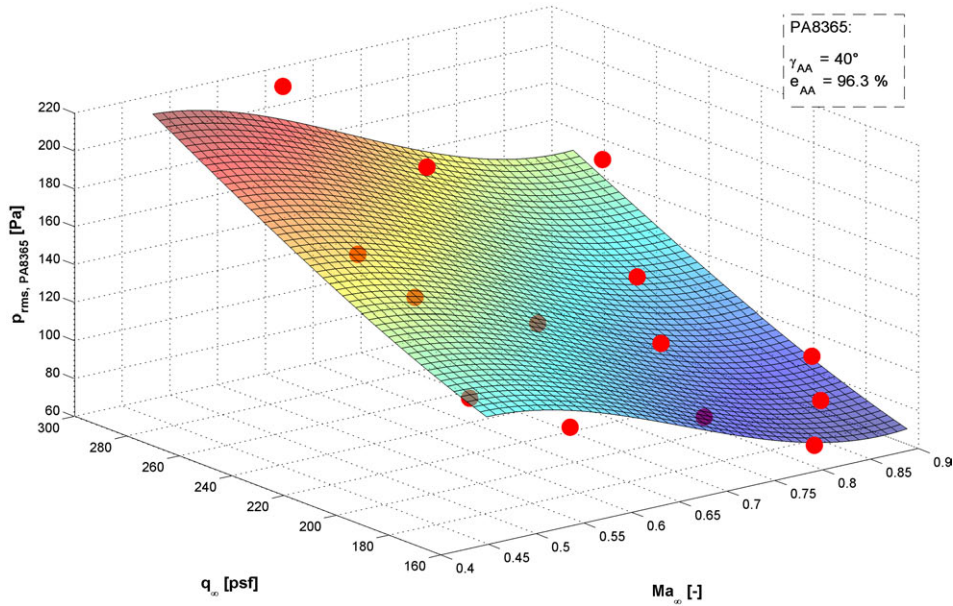
The TA average (Figure 6.21.c) features a qualitatively similar behavior to PA8365, but is slightly more curved and ranges on a significantly lower value level because of the numerous sensors shielded from the high energy outer flow. Those sensors issue SPL values around the ground noise level ( $\approx 120$  dB) particularly for a low  $Ma_\infty$  and  $q_\infty$ , which is the reason for higher uncertainties in the regression model of the TA average. In contrast, the values of PA8352 and PA8365 exceed the 120 dB threshold for the whole regarded input value range by far.



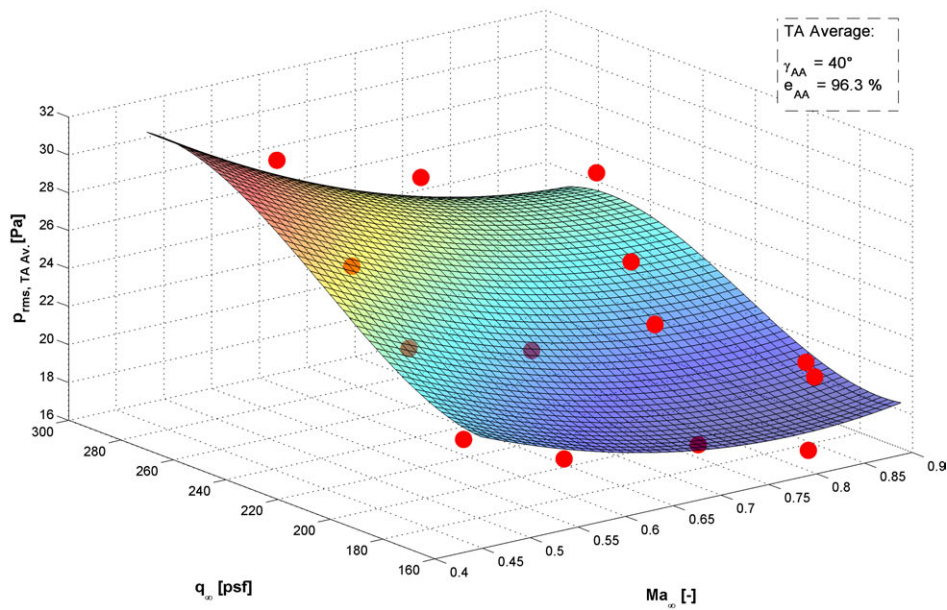
(a) Response of sensor PA8352.

**Figure 6.21.:** Effect function  $p_{rms}(Ma_\infty, q_\infty, e_{AA} = 96.3\%)$  for selected response variables compared to measured flight test points (red dots).





(b) Response of sensor PA8365.



(c) Response of TA average.

Figure 6.21.: Effect function  $p_{rms}(Ma_{\infty}, q_{\infty}, e_{AA} = 96.3\%)$  for selected response variables compared to measured flight test points (red dots).

## 6.4. Cavity Aeroacoustics

If the PSD average of all cavity sensors except for the hot spots is plotted for the lowest regarded aperture exposure  $e_{AA} = 10\%$  (see [Figure 6.22](#)), two pronounced peaks become visible at 24.5 Hz and 42 Hz. The same peaks have already been observed for the sensor PA8412 in [Figure 6.14](#) on p. 37.

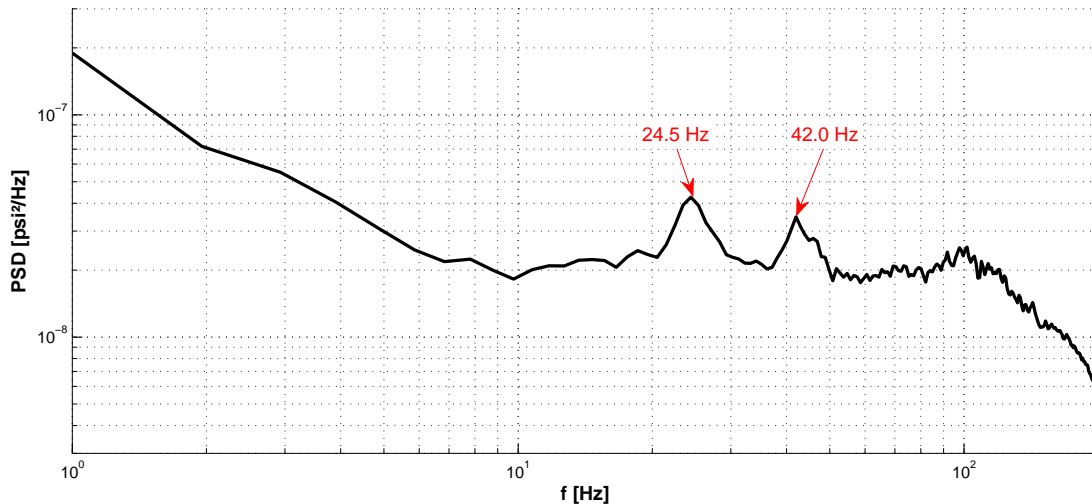


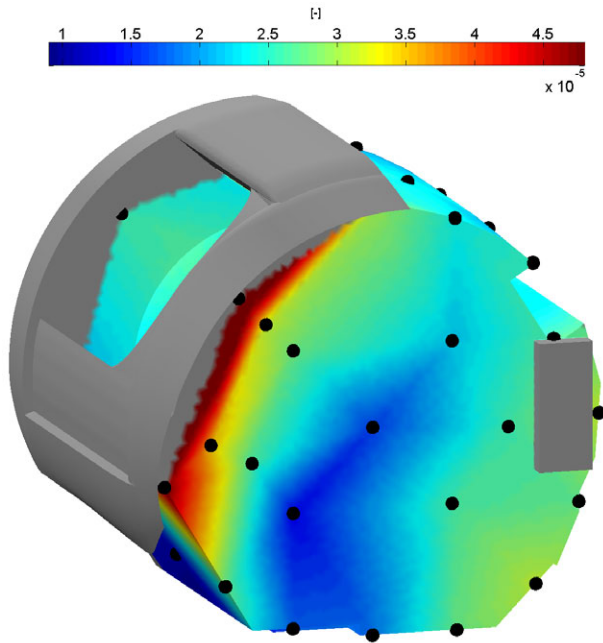
**Figure 6.22.:** PSD( $f$ ) plot of the average of narrowband cavity sensors, i. e. all cavity sensors which are not listed as hot spots in [Figure 6.12](#) on p. 35. FLT033\_TC032\_AA40\_TA40\_EXP10\_ALT42k\_MA0.85.

In [Figure 6.23.a](#) and [Figure 6.23.c](#) on p. 49, the spatial distribution of the spectral pressure coefficient  $c_p$  for these two modes is displayed, using the interpolation of flight test data along the cavity surface. The blue areas approximately represent acoustic nodal points, whereas the red zones indicate the antinodes, where strong acoustic pressure fluctuations occur. Additional views of the observed modes can be found in [Figure C.5](#) on p. 88.

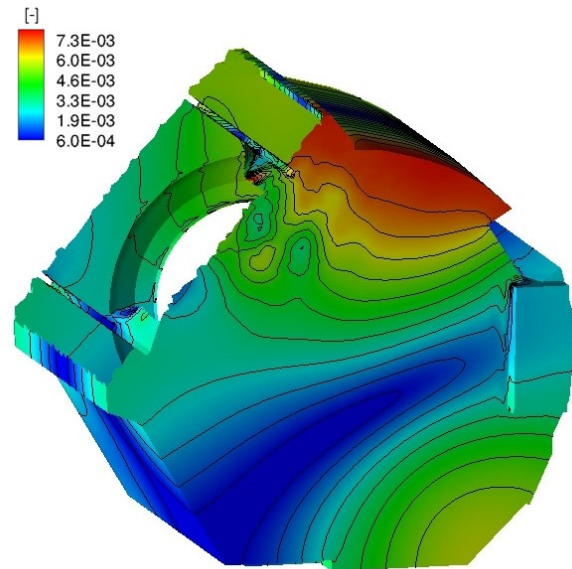
If these distributions are compared to the modes at 46 Hz and 58.5 Hz determined by CFD simulations of Schmid [22], a surprising resemblance can be discovered (cp. [Figure 6.23.b](#) and [Figure 6.23.d](#) on p. 49). Even with the little amount of available sensors, the stretched minimum on the cavity aft bulkhead for the peak at 24.5 Hz can be reproduced by means of flight test data. Apart from its longitudinal direction, this minimum is quite similar to the acoustic nodal area that has been identified by Schmid. Moreover, the pattern of radially aligned acoustic minima and maxima at 42 Hz on the forward bulkhead resembles the analogous simulation-based appearance of the mode at 58.5 Hz in Schmid's work.

The similarity of the respectively compared modes from the flight observations and CFD simulations suggests that those modes originate from the same acoustic phenomena. However, the fact that the simulation-derived modes are shifted by approximately 20 Hz relatively to the measured modes, is not very well understood and is subject of further investigations.

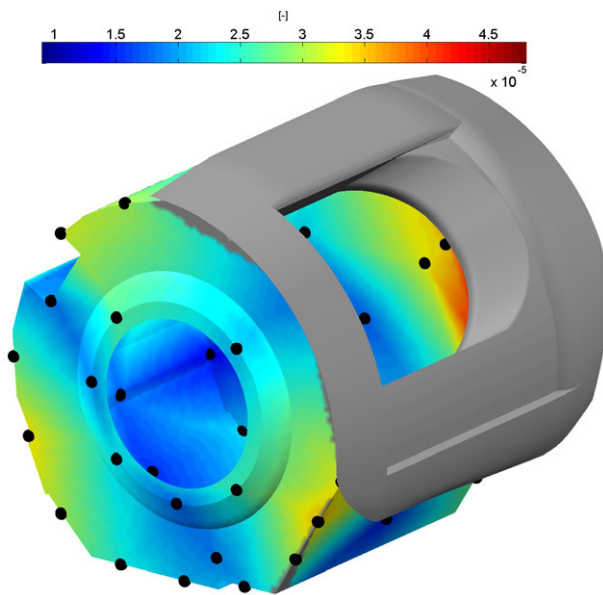
One main difference between the simulated and observed spatial  $c_p$  distribution is the location of the  $c_p$  maximum. In the simulation results, the highest values are reached on the upper part of the aft bulkhead, whereas the flight tests clearly show that the maximum is located right under the aperture ramp. Furthermore, in accordance to the findings of [Section 6.3.1](#) (p. 34 ff.), it stands out that the CFD results exceed the flight test measurement values by two orders of magnitude.



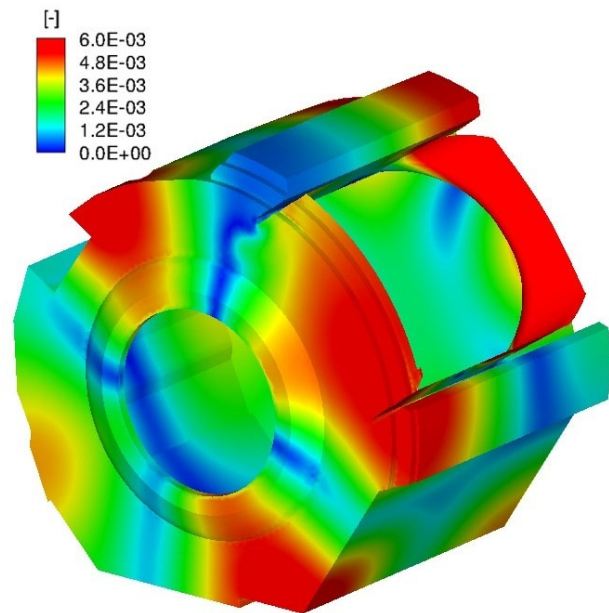
(a) Peak at the frequency  $f = 24.5$  Hz, based on flight test data.  
FLT033\_TC032\_AA40\_TA40\_EXP10\_ALT42k\_MA0.85.



(b) Peak at the frequency  $f = 46$  Hz, based on CFD simulations by Schmid [22].  
AA40\_TA40\_EXP100\_ALT41k\_MA0.85.



(c) Peak at the frequency  $f = 42.0$  Hz, based on flight test data.  
FLT033\_TC032\_AA40\_TA40\_EXP10\_ALT42k\_MA0.85.



(d) Peak at the frequency  $f = 58.5$  Hz, based on CFD simulations by Schmid [22].  
AA40\_TA40\_EXP10\_ALT41k\_MA0.85.

**Figure 6.23.:** Comparison of  $c_{p,rms}$  contour plots derived from CFD simulations and flight tests for two observed acoustic peaks (see Figure 6.22 on p. 48).



## 7. Summary

Two core tasks have been accomplished in this study thesis: as a first step, the complete data postprocessing procedure has been substantially reworked, optimized and equipped with numerous new powerful features. All this has been concentrated in the standalone software tool SADA (SOFIA Acoustic Data Analyzer) based on the groundwork of Schmid [22] and Schwarz [24]. Finally, having created an unobstructed and efficient process chain that way, the aeroacoustic behavior of the SOFIA telescope cavity has been representatively and comprehensively analyzed by means of available flight test data.

### 7.1. Postprocessing Procedure Optimization

In order to be able to perform the aeroacoustic analysis as presented in [Chapter 6](#) (p. 21 ff.), it has been decided that the whole data processing, starting from the raw flight test data files and finishing with the final evaluation plots, needs to be revised and significantly enhanced. For this purpose, it was necessary to get familiar with the existing postprocessing procedure first. Realizing the numerous separate tools and converters the procedure consisted of, it has been identified that the biggest optimization potential lies in combining the loosely connected process components. In addition, this opportunity was used to define new features that crucially increase the value of the process. As a result, the SOFIA Acoustic Data Analyzer (SADA) has been reprogrammed and extended such that it fulfilled all these requirements. It evolved into a very user-friendly, autonomous, flexible and highly efficient software tool. Compared to the previous process chain, it not only minimizes the working time and effort for the user, but also enables him to gain a vivid view and understanding of any imported configuration with regard to geometry, instrumentation and aeroacoustics. Furthermore, it makes the obtained test data comparable to CFD simulations by means of its advanced 2D and 3D plot features (e.g. contour plots). Due to SADA's integration into the MATLAB<sup>®</sup> environment, the full range of advantages of the numerical computing platform is available to the user. This includes the possibility to further process the evaluation results with internal MATLAB<sup>®</sup> functions or to expand the tool by adding new functionality with little effort.

### 7.2. Aeroacoustic Data Analysis

First and foremost, the aeroacoustic analysis showed that among all tested aperture elevation angles  $\gamma_{AA} = 40^\circ$  is critical from an aeroacoustic perspective. Next, the downwash predicted by the CFD simulations of Schmid [22] for a fully exposed aperture could be very well observed within the flight test data. Apparently, this downward flow jet asymmetrically impinges on the headring and in a weaker form on the primary mirror surface. Furthermore, the noise level detected on the identified TA hot spots proved to be uncritical for important SOFIA operational points. As expected, it also became obvious that those sensors which are exposed to the small scale shear layer or downwash instabilities, yield a broadband characteristic in the frequency spectrum as well as PSD values with a

high order of magnitude. In contrast, those sensors which are shielded from these flow effects by the TA structure, cavity geometry or the URD, reveal existing acoustic modes.

The relationship between the MACH number and excitation frequencies suggested by the ROSSITER formula 5.6 on p. 17 could not be fully confirmed. Indeed, a weaker upward trend of peak frequencies for increasing MACH numbers could be detected. However, the mismatch of predicted and observed frequencies as well as the different frequency gradients indicate that the utilized formula and/or its semi-empiric parameters  $K$  and  $\gamma$  have to be better adapted to the specific three-dimensional SOFIA configuration.

Another important finding for the project is the relatively low aeroacoustic activity and the absence of strong acoustic modes inside the cavity. Unlike the CFD predictions, the flight tests show that even in the worst case the shear layer is very stable and obviously no serious cavity resonance modes are excited. The cause of the discrepancy between the measured and predicted behavior is subject of further investigations by the DSI aeroacoustic team.

An essential contribution to the understanding of dependencies between pressure fluctuations and selected global parameters has been provided by the performed regression analysis. It has been shown that relevant sensors' behavior and trends can be captured by a simple effect function based on a polynomial approach. The regression formula proved to be suitable for relatively accurate predictions of the output variables at any intermediate position in the input domain.

The consideration of spatial pressure fluctuations along the cavity surface for obvious acoustic peaks revealed that there is a remarkable resemblance between certain observed and predicted modes, although the respectively compared cases exhibit a big frequency offset of about 20 Hz relatively to each other. This circumstance is not very well understood and needs to be further analyzed in the future.

# Bibliography

- [1] K. K. AHUJA AND J. MENDOZA: *Effects of Cavity Dimensions, Boundary Layer and Temperature on Cavity Noise with Emphasis on Benchmark Data To Validate Computational Aeroacoustic Codes*. NASA CR 3438, Georgia Institute of Technology, Atlanta, Georgia, Apr. 1995.
- [2] S. CHATTERJEE AND A. S. HADI: *Influential Observations, High Leverage Points, and Outliers in Linear Regression*. Statistical Science, Vol. 1, p. 379–416, 1986.
- [3] M. DÜRING: *Investigation of Methods to Influence Resonance Characteristics of the SOFIA Telescope Cavity*. Studienarbeit, Institut für Aerodynamik und Gasdynamik der Universität Stuttgart, NASA Ames Research Center, Moffett Field, California, 2009.
- [4] C. EGER: *Erstellung einer generischen Prozess-Software in MATLAB für die Auswertung der SOFIA Flugversuchsdaten sowie Charakterisierung des Verhaltens des Schwingungsisolations-Systems des Teleskops im Fluge*. Diplomarbeit, Institut für Flugzeugbau der Universität Stuttgart, NASA Dryden Flight Research Center, Palmdale, California, 2008.
- [5] C. ENGFER: *Comparison of the Flight Test ( $AA=23^\circ$ ) Results with CFD Simulations and Wind Tunnel Data*. Tech. Rep. I, Deutsches SOFIA Institut der Universität Stuttgart, NASA Dryden Flight Research Center, Palmdale, California, Jun. 2010.
- [6] C. ENGFER: *Comparison of the Flight Test ( $AA=40^\circ$ ) Results with CFD Simulations and Wind Tunnel Data*. Tech. Rep. II, Deutsches SOFIA Institut der Universität Stuttgart, NASA Dryden Flight Research Center, Palmdale, California, Jul. 2010.
- [7] C. ENGFER. Personal communication, 2010/2011.
- [8] R. GEHRZ ET AL.: *The Science Vision for the Stratospheric Observatory for Infrared Astronomy*. Tech. Rep., NASA Ames Research Center, Moffett Field, CA, Jun. 2009.
- [9] B. GREINER: *Operational Modal Analysis and its Application for SOFIA Telescope Assembly Vibration Measurements*. Studienarbeit, Institut für Raumfahrtssysteme der Universität Stuttgart, NASA Dryden Flight Research Center, Palmdale, California, 2009.
- [10] H. J. KÄRCHER: *Airborne Environment - a Challenge for Telescope Design*. Airborne Telescope Systems, p. 278–284, Jun. 2000.
- [11] L. KELLER AND J. WOLF: *NASA's New Airborne Observatory*. Sky and Telescope, p. 22–28, Oct. 2010.
- [12] A. KRABBE, R. TITZ AND H.-P. RÖSER: *SOFIA oder: Warum Astronomen in die Luft gehen*. Sterne und Weltraum, p. 1052–1063, Dec. 1999.
- [13] R. LERCH, G. M. SESSLER AND D. WOLF: *Technische Akustik - Grundlagen und Anwendungen*. Springer-Verlag Berlin Heidelberg, 2009.
- [14] THE MATHWORKS, INC.: *MATLAB® R2010b Documentation*, Natick, MA, USA.
- [15] M. MEYER: *Signalverarbeitung - Analoge und Digitale Signale, Systeme und Filter*. Vieweg +

- Teubner Verlag, Wiesbaden, 5. Auflage, 2009.
- [16] M. MÖSER: *Messtechnik der Akustik*. Springer-Verlag Berlin Heidelberg, 2010.
- [17] H. E. PLUMBLEE, J. GIBSON AND L. LASSITER: *A Theoretical and Experimental Investigation of the Acoustic Response of Cavities in an Aerodynamic Flow*. Tech. Rep. WADD-TR-61-75, US Air Force, Mar. 1962.
- [18] M. REAVES: *Parameter Identification List*, NASA Ames Research Center, NASA Dryden Flight Research Center, German Aerospace Center, Oct. 2008.
- [19] J. E. ROSSITER: *Wind-Tunnel Experiments on the Flow over Rectangular Cavities at Subsonic and Transonic Speed*. R&M 3438, Aeronautical Research Council, London, UK, Oct. 1964.
- [20] S. SCHMID: *Cavity Sensor Coordinates*. Technical Document.
- [21] S. SCHMID: *TA Sensor Coordinates*. Technical Document.
- [22] S. SCHMID: *Simulation der instationären Strömung um das Stratosphärenobservatorium SOFIA*. Dissertation, Institut für Aerodynamik und Gasdynamik der Universität Stuttgart, NASA Ames Research Center, Moffett Field, California and NASA Dryden Flight Research Center, Palmdale, California, 2009.
- [23] S. SCHMID AND C. ENGFER: *Control Room Guide - Aeroacoustics*, NASA Dryden Flight Research Center, Palmdale, California, Feb. 2010.
- [24] G. SCHWARZ: *Design and Development of a MATLAB based Test Flight Data Analyzer for SOFIA*. Diplomarbeit, Institut für Aerodynamik und Gasdynamik der Universität Stuttgart, NASA Ames Research Center, Moffett Field, California and NASA Dryden Flight Research Center, Palmdale, California, 2010.
- [25] J. STUTZKI: *SOFIA: The Stratospheric Observatory for Infrared Astronomy*. Reviews in Modern Astronomy, Vol. 19 (ed S. Röser), p. 293–314, Jan. 2008.
- [26] P. D. WELCH: *The Use of Fast Fourier Transform for the Estimation of Power Spectra: A Method Based on Time Averaging Over Short, Modified Periodograms*. IEEE Transactions on Audio and Electroacoustics, Vol. AU-15, p. 70–73, Jun. 1967.



# A. Operating Guidelines for the SOFIA Acoustic Data Analyzer

The SOFIA Acoustic Data Analyzer (SADA) is a MATLAB<sup>®</sup> based software tool serving to analyze and evaluate the flight test data of the SOFIA aircraft from an aeroacoustic point of view. After having been launched and equipped with a GUI by Schmid [22] and Schwarz [24], SADA has been fundamentally reworked and enhanced by the author of this thesis (see Section 4.3 on p. 12 ff.).

Since most of the SADA functions are intuitive and self-explanatory, this chapter is rather meant to support the user with *advanced* GUI functions as well as operations and adjustments *behind the scenes* of the tool.

## A.1. Advanced GUI Functions

As displayed in Figure A.1 on p. 56, the GUI workspace window is divided into several panels, each of which comprises GUI components dedicated to a certain subtask or aspect of an analysis session:

- The *Session Input* panel contains all important buttons, switches and input fields serving to define all significant input parameters of a custom session.
- The *Time Converter* panel is a small integrated tool that is able to convert time stamps between the two formats `hours:minutes:seconds` and `seconds`.
- The *Plot Workspace* panel lets the user choose the MATLAB<sup>®</sup> window in which the next plot will be displayed.
- In the *Plot Matrix* panel, one can determine the amount and arrangement of analysis plots within a window.
- The adjustments in the *3D Geometry Specifications* panel are applied to the interactive three-dimensional model of the SOFIA configuration.
- The *Session Content* panel mainly provides the possibility to define the plot type (cp. Table 6.1 on p. 24).

In the following, the functions of the *Plot Matrix* panel and the *3D Geometry Specifications* panel are explained in detail.

### A.1.1. Plot Matrix Panel

Having completed the session-specific operations and adjustments in the *Session Input* panel and having selected a *two-dimensional* plot type in the *Session Content* panel, the user can choose to generate the selected output either in a single or in separate plots (subplots) within a window. For this purpose, he/she should select the desired radio button in the *Plot Matrix* panel (see Figure A.1 on

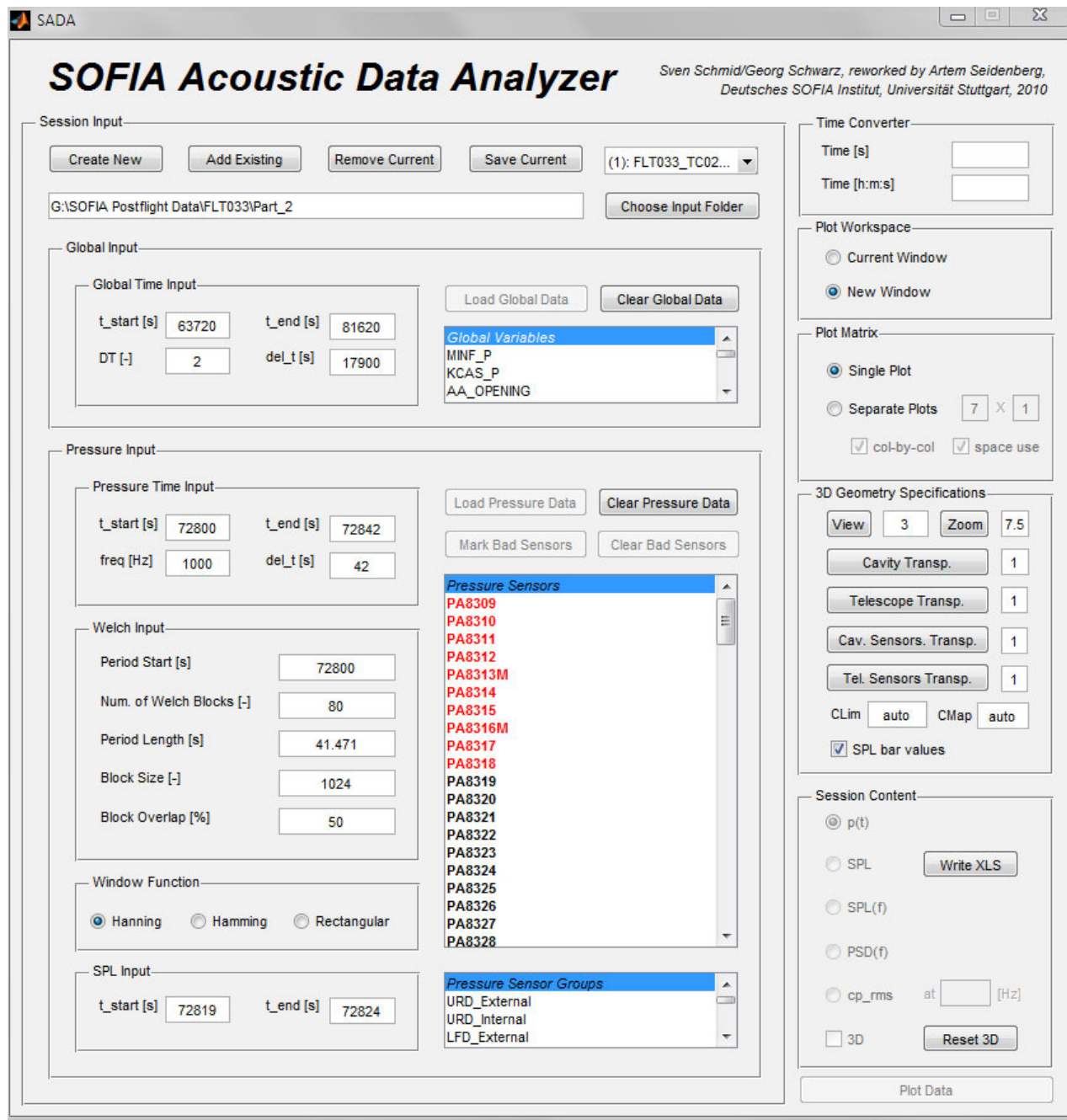


Figure A.1.: Screenshot of the reworked SOFIA Acoustic Data Analyzer workspace window, December 2010.

p. 56). In case of separate plots, it is necessary to specify the plot matrix dimensions, i. e. the number of rows (left field) and the number of columns (right field) formed by the subplots. If *col-by-col* is checked (default), the plot matrix is filled column by column and each column from top to bottom. However, if *col-by-col* is unchecked, the matrix is filled row by row and each row from left to right. In both cases, all selected output items (calculated outputs of selected sensors) are individually inserted in the order of their corresponding session number and their position in the sensor list. The number of the selected output items in all loaded sessions must not exceed the number of subplots. However, these numbers do not necessarily need to be equal. In case the number of selected output items is smaller than the number of plots, the matrix will not be complete; but the remaining slots can be filled later with other items if the considered window is active and the radio button *Current Window* in the *Plot Workspace* panel is selected.

By checking the option *space use*, the user can supersede the native plot distribution algorithm of MATLAB<sup>®</sup> and activate an advanced method, achieving a better utilization of available space.

### A.1.2. 3D Geometry Specifications Panel

The *3D Geometry Specifications* panel comprises main GUI components controlling the appearance of the three-dimensional TA and cavity model associated with the currently selected session. There are six buttons fulfilling the following tasks:

- The *View* button updates the current view perspective of the 3D geometry according to the entry in the adjacent input field. This field accepts the same arguments as the MATLAB<sup>®</sup> `view` command<sup>1</sup>. The most important syntax variants are
  - 2 for the default MATLAB<sup>®</sup> two-dimensional view,
  - 3 for the default MATLAB<sup>®</sup> three-dimensional view, and
  - `[az, el]`, where `az` and `el` respectively denote the azimuth and elevation angle of the viewpoint in degrees [°].
- The *Zoom* button updates the current zoom level of the 3D geometry according to the entry in the adjacent input field. This entry is passed to the MATLAB<sup>®</sup> `CameraViewAngle` axes property<sup>1</sup>. Therefore, it should be a scalar greater than 0 and less than or equal to 180 (angle in degrees [°]). The greater the angle, the larger the field of view, and the smaller objects appear in the scene.
- The four buttons *Cavity Transparency*, *Telescope Transparency*, *Cavity Sensors Transparency* and *Telescope Sensors Transparency* change the degree of transparency of the respective objects. Each of the corresponding input fields expects the same argument as the MATLAB<sup>®</sup> `FaceAlpha` patch property<sup>1</sup>: a scalar between 0 and 1, where 1 (default) means fully opaque and 0 means completely transparent (invisible).

Apart from these general 3D plot settings, there are two special adjustments for the contour plot generation (i. e. in case *3D* is checked in the *Session Content* panel):

- The *CLim* input field passes the user-defined arguments to the MATLAB<sup>®</sup> `CLim` axes property<sup>1</sup>. This property determines how the visualized data values are mapped to the color map of the current MATLAB<sup>®</sup> figure window. Therefore, the input field should contain either

<sup>1</sup>For further details, see the corresponding section in the MATLAB<sup>®</sup> documentation [14].

- `auto`, which assigns the color limits automatically to the minimum and maximum of the regarded data values, or
- `[climmin, climmax]`, where `climmin` is the value of the data mapped to the first color in the color map, and `climmax` represents the value of the data mapped to the last color in the color map.

For further information, see also the `caxis` command in the MATLAB<sup>®</sup> documentation [14].

- The `CMap` input field controls, which segment of the color map is used for the range of data values specified by `CLim`. `CMap` accepts the syntax `[cmapmin, cmapmax]`, where `cmapmin` and `cmapmax` should be scalar values between 0 and 1. They determine that the new limits of the color map are located at `cmapmin·100 %` and `cmapmax·100 %` of the original one.

Last but not least, one can find the `SPL bar values` check box, which provides an additional adjustment for 2D SPL plots. In case the check box is activated and `SPL` is selected in the `Session Content` panel, the resulting SPL bar chart will contain additional numeric values printed above the bars. For clarity reasons, this option should not be used in plots with a large amount of bars.

## A.2. Working Directory File System

In order to handle a large amount of data without losing track, SADA automatically maintains a certain organization structure in the working directory. An overview of the folder hierarchy is given in Figure A.2.

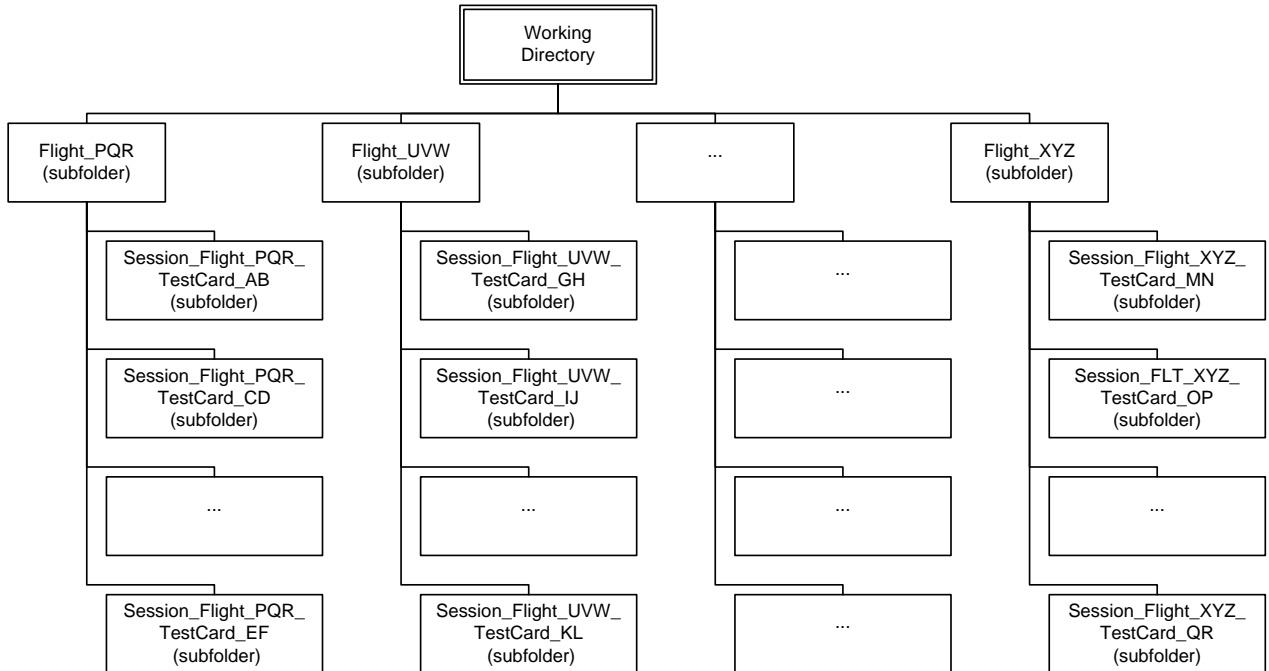


**Figure A.2.:** Folder hierarchy in the SADA working directory. Combinations of capital letters like “PQR” or “AB” stand for possible flight or test card numbers. The working directory may contain any number of flight subfolders, each of which may accommodate any number of session subfolders. A complete, hierarchically sorted list of SADA sessions used within this thesis can be found in Table B.1 (p. 65 f.).

Once a new session is generated via the GUI, SADA creates a session subfolder within the corresponding flight subfolder. If the latter does not exist yet, it is created as well. Each session subfolder serves as a container for session-specific files, which are generated throughout the user's session. One of them is the *session definition file* (or simply *session file*), which appears as `SessionInput.xlsx` by default. It is an Excel<sup>®</sup> spreadsheet accommodating a hash table, i. e. a list of identifying keys (first column) and their associated values (second column). The keys correspond to internal variable names in the SADA source code; the values contain numbers, arrays or other MATLAB<sup>®</sup> readable code. Every time a session is saved in the GUI, the associated session file is updated. Since this file contains a full representation of the GUI field inputs and control settings, a previously saved and closed session can be loaded and fully reconstructed at any time. The entries in the session file should not be modified manually, since this could lead to unexpected results when loading the file.

### A.3. Internal SADA File System

SADA has been designed with a certain internal file structure, which is illustrated in [Figure A.3](#) schematically. On the one hand, it contains essential, mandatory files allowing SADA to function properly in the first place. On the other hand, there are data files and additional scripts which do not directly contribute to regular SADA operations, but serve to generate important input files for SADA and thus provide the user with full flexibility in the long term.

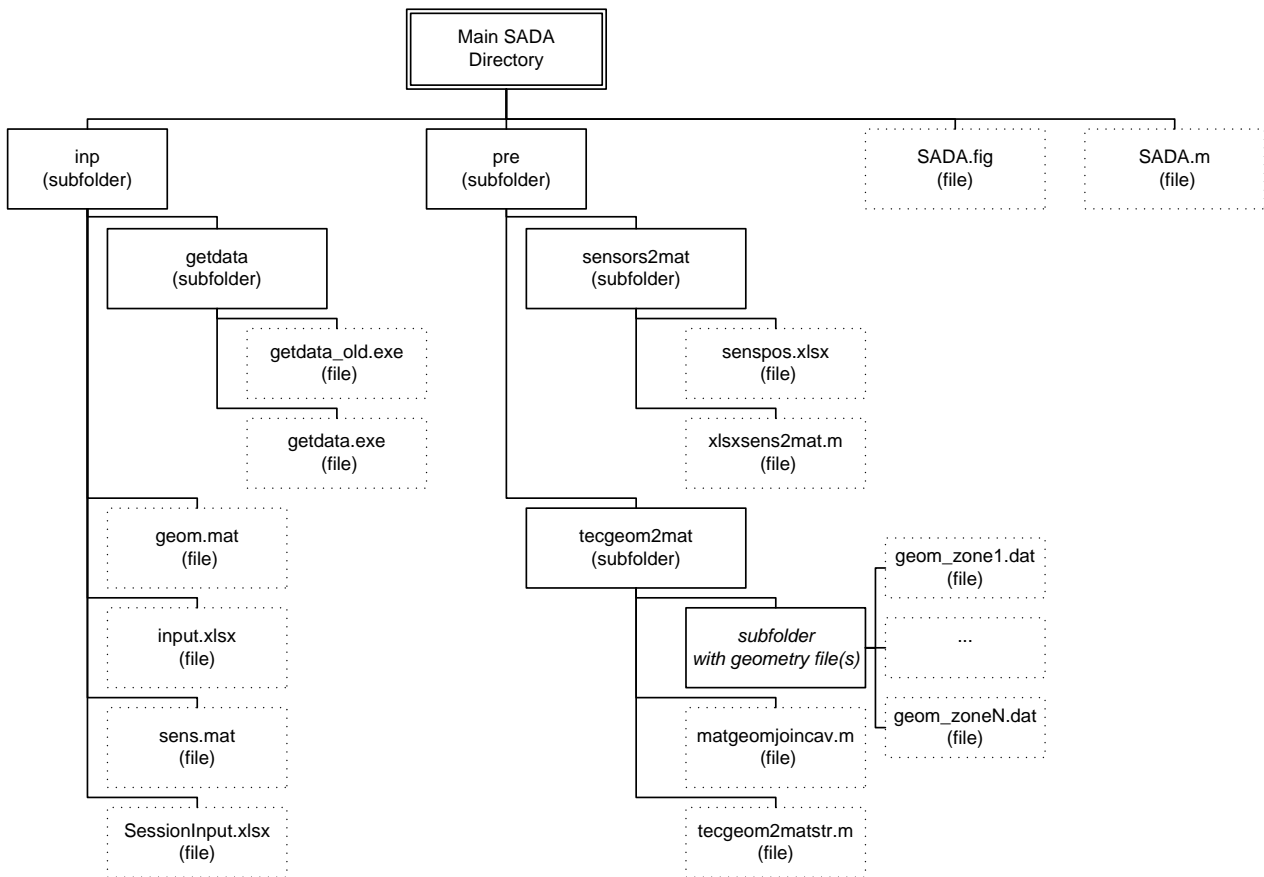


Figure A.3.: Internal SADA file system.

First and foremost, the file `SADA.m`, which is located in the main SADA directory, contains the tool’s source code with more than 6200 lines. The code is written in the proprietary programming language of MATLAB<sup>®</sup> and uses a series of its powerful function libraries. The second file in the main directory is `SADA.fig`. It is a binary MATLAB<sup>®</sup> figure file, in which the GUI layout is saved. This means that `SADA.fig` determines the appearance of the GUI, whereas `SADA.m` contains MATLAB<sup>®</sup> functions that control the GUI and interact with it. Both files are vital for the operation of SADA.

Furthermore, there are two folders in the main SADA directory: `inp` (input folder) and `pre` (preparation folder). The former accommodates necessary external tools and indispensable SADA input files, which are directly connected to the source code; the latter contains raw data files and small scripts in order to generate the input files for the `inp` folder.

### A.3.1. SADA Input Folder

On closer inspection, one can explain the purpose of the respective items in the `inp` folder as follows:

- The Excel<sup>®</sup> file `input.xlsx` contains a list of control switches in the form of a hash table. It is loaded upon invocation of `SADA.m` and controls some behavioral aspects of the tool, which are explained in [Table A.1](#). By editing this file, the user is given the possibility to make long term adjustments without modifying the source code itself. Advanced users might also want to add new entries, which will be automatically passed to SADA.
- The binary files `geom.mat` and `sens.mat` contain the geometry and sensor data of the SOFIA configuration. They are loaded by SADA just after `input.xlsx`. Both files can be generated using the corresponding scripts in the `pre` folder (see [Section A.3.2](#) on p. 62 ff.).
- The subfolder `getdata` contains different versions of the NASA `getdata` tool, which is invoked as a subroutine of SADA. Normally, the current version of the `getdata` tool should be used. However, if that version is unstable or defective, one can switch to the latest stable version. The corresponding adjustment can be made in the `input.xlsx` file (see [Table A.1](#)).
- The file `SessionInput.xlsx` is an empty template, which is used to create new session files within the working directory (cp. [Section A.2](#) on p. 58 ff.).

**Table A.1.:** Control variables in the `input.xlsx` file of SADA.

Variable ID (without prefix)	Type	Explanation
<code>units</code>	Structure array	Global parameter IDs (keys) and their associated units (values)
<code>BadSensors</code>	Cell array	Bad sensor IDs
<code>BlockOverlap</code>	Integer	Default WELCH block overlap
<code>BlockSize</code>	Integer	Default WELCH block length
<code>DefSession</code>	Cell array	Default session presettings according to the structure shown in <a href="#">Section 6.1</a> on p. 24
<code>GlobVarsDef</code>	Cell array	Default global parameters
<code>NumWelchBlocks</code>	Integer	Default number of WELCH blocks
<code>PressureSensorGroups</code>	Cell array	Default pressure sensor groups

---

PressureSensorMasterGroups	Cell array	Default pressure sensor master groups, i.e. groups containing smaller groups
rfOrigin	1D matrix	Absolute CARTESIAN coordinates of the origin of the relative reference frame [mm] (cp. [20], [21] and Section B.2 on p. 67)
sensSize	Integer	Size of the <i>displayed</i> sensors (sphere diameter) [mm]
TA	Integer	Default TA elevation angle of the available 3D geometry model
AverageLineStyle	String	Style of average lines in 2D plots (MATLAB <sup>®</sup> syntax)
AverageLineWidth	Integer	Width of average lines in 2D plots (MATLAB <sup>®</sup> syntax)
Cavity_Color	1D matrix	RGB color definition of the cavity surface
CMap	String	Default MATLAB <sup>®</sup> color map
DefPath	String	Default path of the SADA working directory
DefWindowFcn	String	Default window function ID; possible values: WinHann (Hanning), WinHamm (Hanning), WinRect (Rectangular)
getDataOld	Integer	Switch for the getdata tool version; possible values: 1 (older version), 0 (current version)
LineStyleOrder	Cell array	Sequence of line styles to be used in 2D plots (MATLAB <sup>®</sup> syntax)
Material	String	Reflectance property of the 3D geometry model (see MATLAB <sup>®</sup> material function)
MaxLinesSessionInput	Integer	Maximum amount of lines in a session file
RowCol	1D matrix	Default plot matrix dimensions
Sensor_Color	1D matrix	RGB color definition of the sensors
SPLYLim	1D matrix	Default <i>y</i> axis limits in SPL bar charts
subplotEdgeDist	1D matrix	Distances [% of window dimension] controlling the distribution of subplots within a window if the option <i>space use</i> in the <i>Plot Matrix</i> panel is checked: [ <i>left window margin</i> , <i>bottom window margin</i> , <i>horizontal subplot spacing</i> , <i>vertical subplot spacing</i> , <i>horizontal subplot offset</i> ]
TA_Color	1D matrix	RGB color definition of the TA

---

### A.3.2. SADA Preparation Folder

Unlike the `inp` folder, the `pre` folder and its contents are not directly linked to the processes of SADA. As already suggested by its name, the folder is rather meant to be the place for all preparation steps needed for SADA setup. Basically, it contains two main routines included in the two subfolders `sensors2mat` and `tecgeom2mat` respectively. Each of them accommodates original data files on the one hand and corresponding conversion scripts on the other hand, serving to generate the previously mentioned binary input files `sens.mat` and `geom.mat`.

The `tecgeom2mat` subfolder is in charge of the geometry model generation. The original geometry has been exported from Tecplot<sup>®</sup> to ASCII files, which are located in a subfolder within `tecgeom2mat` (see Figure A.3 on p. 59). Those files contain the geometry information in the form of vertices (Nodes) and faces (Elements) derived from vertex triangulation:

```
TITLE      = "Grid: MESH/Serie_D_gamma40_DES.cgns.cdf, ..."
VARIABLES = "X"
"Y"
"Z"
ZONE T="viscous_wall_telescope"
STRANDID=0, SOLUTIONTIME=0
Nodes=5, Elements=4, ZONETYPE=FETriangle
DATAPACKING=POINT
DT=(DOUBLE DOUBLE DOUBLE )
3.713749649E+04 -1.501024446E+03 7.373571789E+03
3.713856206E+04 -1.522844288E+03 7.392683905E+03
3.716993851E+04 -1.488984771E+03 7.387920115E+03
3.716887294E+04 -1.511595507E+03 7.406089680E+03
3.715371750E+04 -1.505523477E+03 7.389572330E+03
1 3 5
1 5 2
2 5 4
3 4 5
```

The above example of such an ASCII file exhibits five vertices (five lines with  $x_{abs}, y_{abs}, z_{abs}$  coordinates) and four faces (four lines with vertex indexes). In order to produce the binary file `geom.mat`, the name of the subfolder containing the ASCII files needs to be passed to the conversion script by printing

```
tecgeom2matstr(NameOfSubfolder)
```

This causes the TA and cavity geometry to be stored in a MATLAB<sup>®</sup> `struct` variable in the form of separate surface patches (former Tecplot<sup>®</sup> zones). However, for future contour plots of the cavity, it is important to join the cavity patches to a single entity. This is accomplished by the second script, which needs to receive the name of the binary geometry file:

```
matgeomjoincav(geom.mat)
```



In this way, the file `geom.mat` is updated and finally needs to be copied to the `inp` folder in order to be utilized by SADA. It is important that a copy remains in the `tecgeom2mat` subfolder, because it is needed for the sensor file generation, as explained in the following.

The subfolder `sensors2mat` includes an Excel<sup>®</sup> spreadsheet named `senspos.xlsx`, which contains a list of all known pressure sensors and their properties collected from different resources [7, 20, 21, 23]. Each line in the file corresponds to a sensor and each column represents a sensor's property (see Table A.2).

Sensor property	Explanation
<code>name</code>	Sensor ID
<code>name_alt</code>	Alternative sensor ID introduced by Schmid [22] (cp. Table B.2)
<code>x_abs</code>	$x$ coordinate of the sensor in the absolute reference frame
<code>y_abs</code>	$y$ coordinate of the sensor in the absolute reference frame
<code>z_abs</code>	$z$ coordinate of the sensor in the absolute reference frame
<code>x_rel</code>	$x$ coordinate of the sensor in the relative reference frame <sup>2</sup>
<code>y_rel</code>	$y$ coordinate of the sensor in the relative reference frame <sup>2</sup>
<code>z_rel</code>	$z$ coordinate of the sensor in the relative reference frame <sup>2</sup>
<code>sampling_rate</code>	Sampling rate of the sensor
<code>group</code>	Sensor group which the sensor belongs to
<code>priority</code>	Priority of the sensor (not used in this thesis)
<code>micro</code>	Flag indicating whether the sensor is a microphone (1) or not (0)
<code>plot3D</code>	Flag indicating whether the sensor is displayed in the 3D geometry model (1) or not (0)
<code>comment</code>	User-defined comment or note
<code>closestVertex</code>	Coordinates of the vertex that is closest to the sensor (computed afterwards by the script <code>xlxsens2mat.m</code> )
<code>x_ghost</code>	$x$ coordinate of the corresponding ghost sensor <sup>3</sup> (absolute reference frame)
<code>y_ghost</code>	$y$ coordinate of the corresponding ghost sensor <sup>3</sup> (absolute reference frame)
<code>z_ghost</code>	$z$ coordinate of the corresponding ghost sensor <sup>3</sup> (absolute reference frame)
<code>ghost</code>	Flag indicating whether the sensor has an associated ghost sensor (1) or not (0)
<code>first_flight</code>	Number of the first SOFIA flight performed with the sensor on board
<code>last_flight</code>	Number of the last SOFIA flight performed with the sensor on board

**Table A.2.:** Sensor properties in the `senspos.xlsx` file of SADA.

<sup>2</sup>*Relative reference frame:* for information, see [20], [21] and Section B.2 on p. 67.

<sup>3</sup>*Ghost sensor:* additional imaginary sensor that is assigned the same data values as the corresponding real sensor. Ghost sensors are needed to capture the cavity geometry *within* the convex hull of all considered sensors and thus to produce a completely colored contour plot without any left out spots.

The user can update the file `senspos.xlsx` at any time by editing existing entries or adding new ones. In order to make the sensor list available to SADA, it is necessary to run the MATLAB<sup>®</sup> script `xlxsens2mat.m` with the Excel<sup>®</sup> file as the argument:

```
xlxsens2mat(senspos.xlsx)
```

For a successful run of the script, it has to be also ensured that an updated copy of the file `geom.mat` is available in the `tecgeom2mat` subfolder. As a result, a new version of the file `sens.mat` is created and needs to be inserted in the `inp` folder, where it can be accessed by SADA.

# B. Aeroacoustic Analysis Properties

## B.1. SADA Sessions Overview

The following table lists all 63 SADA sessions utilized in this thesis. Each session is characterized by the flight number (FLT), the test card number (TC), the lower and the upper limit of the data analysis time window,  $t_{start,p}$  and  $t_{end,p}$ , the lower and the upper limit of the global time window,  $t_{start,g}$  and  $t_{end,g}$ , the aperture elevation angle  $\gamma_{AA}$ , the telescope elevation angle  $\gamma_{TA}$ , the aperture exposure  $e_{AA}$ , the flight altitude  $h$  and the MACH number  $Ma_{\infty}$ .

**Table B.1.:** SADA Session List.

FLT	TC	$t_{start,p}$ [s]	$t_{end,p}$ [s]	$t_{start,g}$ [s]	$t_{end,g}$ [s]	$\gamma_{AA}$ [°]	$\gamma_{TA}$ [°]	$e_{AA}$ [%]	$h$ [ft]	$Ma_{\infty}$ [-]
24	14	61513	61555	57600	77400	23	23	100	25000	0.6
24	17	63440	63482	57600	77400	23	23	100	30000	0.6
26	10	61335	61377	60120	74100	23	23	100	35000	0,85
26	20	66470	66512	60120	74100	23	23	100	30000	0.79
26	24	68876	68918	60120	74100	23	23	100	25000	0.72
26	31	71300	71342	60120	74100	23	23	100	20000	0.6
26	32	71550	71592	60120	74100	23	23	100	20000	0.65
27	24	65420	65462	58200	77928	23	23	100	15000	0.59
30	9	61310	61352	58080	72480	40	40	40	15000	0.45
30	10	61910	61952	58080	72480	40	40	95	15000	0.45
30	22	66863	66905	58080	72480	40	40	10	15000	0.5
30	23	67330	67372	58080	72480	40	40	40	15000	0.5
30	24	67940	67982	58080	72480	40	40	70	15000	0.5
30	25	68172	68214	58080	72480	40	40	95	15000	0,5
33	9	65285	65327	63720	81620	40	40	40	25000	0.55
33	10	65808	65850	63720	81620	40	40	95	25000	0.55
33	11	66118	66160	63720	81620	40	40	10	25000	0.6
33	12	66451	66493	63720	81620	40	40	40	25000	0.6
33	13	67207	67249	63720	81620	40	40	70	25000	0.6
33	14	67590	67632	63720	81620	40	40	95	25000	0.6
33	16	69148	69190	63720	81620	40	40	40	35000	0.69
33	17	69310	69352	63720	81620	40	40	95	35000	0.69
33	18	69878	69920	63720	81620	40	40	40	35000	0.81
33	19	70218	70260	63720	81620	40	40	95	35000	0.81
33	20	70640	70682	63720	81620	40	40	10	35000	0.85
33	21	71503	71545	63720	81620	40	40	40	35000	0.85
33	22	72155	72197	63720	81620	40	40	70	35000	0.85
33	23	72800	72842	63720	81620	40	40	95	35000	0.85

Table B.1.: SADA Session List (continued).

FLT	TC	$t_{start,p}$ [s]	$t_{end,p}$ [s]	$t_{start,g}$ [s]	$t_{end,g}$ [s]	$\gamma_{AA}$ [°]	$\gamma_{TA}$ [°]	$e_{AA}$ [%]	$h$ [ft]	$Ma_\infty$ [-]
33	24	73540	73582	63720	81620	40	40	40	35000	0.89
33	25	73710	73752	63720	81620	40	40	95	35000	0.89
33	30	77048	77090	63720	81620	40	40	95	40000	0.85
33	31	77282	77324	63720	81620	40	40	95	40000	0.9
33	32	77800	77842	63720	81620	40	40	10	42000	0.85
33	33	78043	78085	63720	81620	40	40	40	42000	0.85
33	34	78880	78922	63720	81620	40	40	70	42000	0.85
33	35	79052	79094	63720	81620	40	40	95	42000	0.85
33	37	80230	80272	63720	81620	40	40	95	42000	0.87
33	38	80390	80432	63720	81620	40	40	40	42000	0.89
33	39	80808	80850	63720	81620	40	40	95	42000	0.89
34	9	59543	59585	59420	79890	40	40	40	25000	0.72
34	10	60128	60170	59420	79890	40	40	95	25000	0.72
34	13	61775	61817	63720	81620	40	40	40	15000	0.55
34	14	62000	62042	63720	81620	40	40	95	15000	0.55
34	15	62260	62302	63720	81620	40	40	10	15000	0.59
34	16	62398	62440	63720	81620	40	40	40	15000	0.59
34	17	63358	63400	63720	81620	40	40	70	15000	0.59
34	18	63749	63791	63720	81620	40	40	95	15000	0.59
34	22	76055	76097	63720	81620	40	40	10	20000	0.4
34	23	75888	75930	63720	81620	40	40	95	20000	0.4
34	24	68880	68920	59420	79890	40	40	40	42000	0.81
34	25	69070	69112	59420	79890	40	40	95	42000	0.81
34	28	76468	76510	59420	79890	40	40	10	15000	0.3
34	29	76923	76925	59420	79890	40	40	40	15000	0.3
34	30	77480	77522	59420	79890	40	40	70	15000	0.3
34	31	77980	78022	59420	79890	40	40	95	15000	0.3
35	25	64560	64602	57120	79680	30	30	95	35000	0.85
35	30	68100	68142	57120	79680	40	40	100	35000	0.85
35	35	74010	74052	57120	79680	30	30	95	42000	0.85
38	10	59358	59400	56400	67800	23	23	100	42000	0.85
40	25	72320	72362	58050	75920	57	57	95	42000	0.85
41	22	60000	60042	53760	79200	50	50	95	35000	0.85
41	30	69030	69072	53760	79200	57	57	100	35000	0.85
41	35	67148	67190	53760	79200	50	50	95	42000	0.85

## B.2. Pressure Sensors Overview

All 236 available pressure sensors are listed in Table B.2 including their properties. The 120 sensors underlying the aeroacoustic analysis of this thesis in Chapter 6 on p. 21 are assigned to the sensor groups “Cavity Aft Bulkhead”, “Cavity Forward Bulkhead”, “Cavity Walls”, “TA Primary Mirror”, “TA Spiderarms”, “TA Suncover”, and “TA Rest”. The sensors of the latter four groups are marked with an alternative sensor ID, which has been introduced in the work of Schmid [22].

The *absolute* CARTESIAN coordinates  $x_{abs}$ ,  $y_{abs}$  and  $z_{abs}$  originate from the three-dimensional model of the SOFIA configuration provided by Schmid [22]. The *relative* CARTESIAN reference frame ( $x_{rel}$ ,  $y_{rel}$ ,  $z_{rel}$ ) with the origin [37 268.0 mm, 0.0 mm, 5867.4 mm] corresponds to the TA coordinate system (EL, XEL, LOS) in Figure 2.4 on p. 6 if the TA is elevated by  $\gamma_{AA} = 90^\circ$  [20, 21].

Table B.2.: Pressure Sensor List

	Sensor ID	$(x_{abs}, y_{abs}, z_{abs})$ [mm, mm, mm]	$(x_{rel}, y_{rel}, z_{rel})$ [mm, mm, mm]	$f_s$ [Hz]
<b>Aperture Ramp</b>	PA8279	n/a	n/a	5000
	PA8280	n/a	n/a	1000
	PA8281	n/a	n/a	1000
	PA8282	n/a	n/a	1000
	PA8283	n/a	n/a	5000
	PA8284	n/a	n/a	1000
	PA8285	n/a	n/a	5000
	PA8286	n/a	n/a	1000
	PA8287	n/a	n/a	1000
	PA8288	n/a	n/a	1000
	PA8289	n/a	n/a	5000
	PA8290	n/a	n/a	5000
	PA8291	n/a	n/a	1000
	PA8292	n/a	n/a	1000
	PA8293	n/a	n/a	1000
	PA8294	n/a	n/a	1000
	PA8295	n/a	n/a	1000
	PA8296	n/a	n/a	5000
	PA8297	n/a	n/a	1000
	PA8298	n/a	n/a	1000
PA8299	n/a	n/a	5000	
PA8300	n/a	n/a	5000	
<b>Aperture Sidewalls</b>	PA8301	n/a	n/a	1000
	PA8302	n/a	n/a	1000
	PA8303	n/a	n/a	1000
	PA8304	n/a	n/a	1000
	PA8305	n/a	n/a	1000
	PA8306	n/a	n/a	1000
	PA8307	n/a	n/a	1000
	PA8308	n/a	n/a	1000
PA8594	n/a	n/a	1000	

**Table B.2.:** Sensor List (continued)

	Sensor ID	$(x_{abs}, y_{abs}, z_{abs})$ [mm, mm, mm]	$(x_{rel}, y_{rel}, z_{rel})$ [mm, mm, mm]	$f_s$ [Hz]
	PA8595	n/a	n/a	1000
<b>Cavity Aft Bulkhead</b>	PA8385	[39493.0, -1759.1, 7626.1]	n/a	1000
	PA8406	[39493.0, -1041.9, 6910.7]	n/a	1000
	PA8412	[39493.0, -1400.5, 7268.4]	n/a	1000
	PA8413	[39493.0, -1583.0, 5498.0]	n/a	1000
	PA8580	[39493.0, 1041.9, 6910.7]	n/a	1000
	PA8581	[39493.0, 1779.0, 5765.0]	n/a	1000
	PA8582	[39493.0, 1042.0, 4825.0]	n/a	1000
	PA8583M	[39493.0, -1042.0, 4825.0]	n/a	1000
	PA8584	[39493.0, 0.0, 5865.5]	n/a	1000
	PA8585	[39493.0, -2122.0, 5765.0]	n/a	1000
<b>Cavity Forward Bulkhead</b>	PA8390	[35326.0, -2019.3, 7886.4]	n/a	1000
	PA8407	[35149.0, -1041.9, 6911.0]	n/a	1000
	PA8414	[35326.0, -562.0, 3662.0]	n/a	1000
	PA8575	[35149.2, 1043.3, 6910.7]	n/a	1000
	PA8576	[35149.2, 1475.0, 5867.4]	n/a	1000
	PA8577M	[35149.2, 1042.0, 4825.0]	n/a	1000
	PA8578	[35149.2, 0.0, 4392.4]	n/a	1000
	PA8579	[35149.0, -1042.0, 4824.2]	n/a	1000
<b>Cavity Walls</b>	PA8375	[39483.2, 2108.4, 7840.6]	n/a	1000
	PA8376	[35329.8, 2152.8, 7860.6]	n/a	1000
	PA8377	[39493.0, 2140.4, 3727.8]	n/a	1000
	PA8378	[35326.0, 2140.4, 3727.8]	n/a	1000
	PA8379	[39493.0, 2965.5, 5867.4]	n/a	1000
	PA8380	[35326.0, 2965.6, 5867.4]	n/a	1000
	PA8381	[35326.0, -1928.0, 3939.0]	n/a	1000
	PA8382	[39493.0, -1928.0, 3939.0]	n/a	1000
	PA8382M	[39493.0, -1928.0, 3939.0]	n/a	1000
	PA8383	[35326.0, 0.0, 3200.5]	n/a	1000
	PA8384	[39493.0, 0.0, 3200.5]	n/a	1000
	PA8386	[39493.0, 31.2, 8699.0]	n/a	1000
	PA8387	[35326.0, -2729.8, 5260.9]	n/a	1000
	PA8388	[37409.5, -2729.6, 5260.8]	n/a	1000
	PA8389	[39493.0, -2730.0, 5260.8]	n/a	1000
	PA8391	[35326.0, -2317.8, 4582.7]	n/a	1000
	PA8392	[37409.5, -2318.2, 4582.5]	n/a	1000
	PA8393	[35326.0, -1044.3, 3346.7]	n/a	1000
	PA8394	[37409.5, -1044.3, 3346.7]	n/a	1000
	PA8395	[35326.5, 1104.7, 3200.5]	n/a	1000
	PA8396M	[37409.5, 1104.5, 3200.5]	n/a	1000
	PA8397	[35326.0, 2704.2, 4747.3]	n/a	1000
	PA8398	[37409.5, 2704.0, 4747.3]	n/a	1000
	PA8399M	[39493.0, 2703.8, 4747.3]	n/a	1000
	PA8400	[35326.0, 2316.7, 6826.9]	n/a	1000

Table B.2.: Sensor List (continued)

	Sensor ID	$(x_{abs}, y_{abs}, z_{abs})$ [mm, mm, mm]	$(x_{rel}, y_{rel}, z_{rel})$ [mm, mm, mm]	$f_s$ [Hz]
	PA8401	[37409.5, 2364.5, 6846.7]	n/a	1000
	PA8402	[39493.0, 2378.2, 6852.2]	n/a	1000
	PA8403	[39493.0, 1081.2, 8477.6]	n/a	1000
	PA8404	[37409.5, 1098.2, 8518.5]	n/a	1000
	PA8405	[35348.1, 1053.2, 8536.0]	n/a	1000
	PA8408	[39493.0, 1104.8, 3200.5]	n/a	1000
	PA8409	[39493.0, -1043.9, 3346.5]	n/a	1000
	PA8566	[36339.3, 31.4, 8779.5]	n/a	1000
	PA8567	[38331.0, 34.8, 8754.8]	n/a	1000
	PA8568	[36367.8, 2965.6, 5866.2]	n/a	1000
	PA8569	[38451.3, 2965.5, 5866.2]	n/a	1000
	PA8570	[37409.5, 2159.0, 7855.0]	n/a	1000
	PA8571M	[37409.5, 2965.5, 5865.0]	n/a	1000
	PA8572	[37409.5, 2140.0, 3728.0]	n/a	1000
	PA8573	[37409.5, 0.0, 3200.5]	n/a	1000
	PA8574M	[37409.5, -1927.0, 3937.5]	n/a	1000
<b>LFD External</b>	PA8245	n/a	n/a	500
	PA8246	n/a	n/a	2000
	PA8247	n/a	n/a	500
	PA8248	n/a	n/a	2000
	PA8249	n/a	n/a	500
	PA8250	n/a	n/a	2000
	PA8251	n/a	n/a	500
	PA8252	n/a	n/a	500
	PA8253	n/a	n/a	500
	PA8254	n/a	n/a	2000
	PA8255	n/a	n/a	500
	PA8256	n/a	n/a	500
	PA8257	n/a	n/a	500
	PA8258	n/a	n/a	500
	PA8259	n/a	n/a	2000
	PA8260	n/a	n/a	500
PA8261	n/a	n/a	500	
<b>LFD Internal</b>	PA8262	n/a	n/a	500
	PA8263	n/a	n/a	2000
	PA8264	n/a	n/a	500
	PA8265	n/a	n/a	2000
	PA8266	n/a	n/a	500
	PA8267	n/a	n/a	2000
	PA8268	n/a	n/a	500
	PA8269	n/a	n/a	500
	PA8270	n/a	n/a	500
	PA8271	n/a	n/a	2000
	PA8272	n/a	n/a	500

**Table B.2.:** Sensor List (continued)

	<b>Sensor ID</b>	$(x_{abs}, y_{abs}, z_{abs})$ [mm, mm, mm]	$(x_{rel}, y_{rel}, z_{rel})$ [mm, mm, mm]	$f_s$ [Hz]
	PA8273	n/a	n/a	500
	PA8274	n/a	n/a	500
	PA8275	n/a	n/a	500
	PA8276	n/a	n/a	2000
	PA8277	n/a	n/a	500
	PA8278	n/a	n/a	500
<b>TA Primary Mirror</b>	PA8319	(10) [37086.0, 383.0, 4715.2]	[-182.0, 383.0, -1152.2]	1000
	PA8320	(11) [37768.0, 49.0, 4715.2]	[500.0, 49.0, -1152.2]	1000
	PA8321	(12) [37086.0, -383.0, 4715.2]	[-182.0, -383.0, -1152.2]	1000
	PA8322	(13) [36347.0, 509.0, 4754.0]	[-921.0, 509.0, -1113.4]	1000
	PA8323	(14) [37268.0, 1017.0, 4754.0]	[0.0, 1017.0, -1113.4]	1000
	PA8324	(15) [38164.0, 509.0, 4754.0]	[896.0, 509.0, -1113.4]	1000
	PA8325	(16) [38164.0, -509.0, 4754.0]	[896.0, -509.0, -1113.4]	1000
	PA8326	(17) [37268.0, -1017.0, 4754.0]	[0.0, -1017.0, -1113.4]	1000
	PA8327	(18) [36347.0, -509.0, 4754.0]	[-921.0, -509.0, -1113.4]	1000
<b>TA Rest</b>	PA8328	(21) [37268.0, 0.0, 5948.8]	[0.0, 0.0, 81.4]	1000
	PA8329	(22) [36042.0, 1202.0, 5084.0]	[-1226.0, 1202.0, -783.4]	1000
	PA8330	(23) [37268.0, 1585.7, 5084.0]	[0.0, 1585.7, -783.4]	1000
	PA8331	(24) [38536.0, 765.0, 5077.6]	[1268.0, 765.0, -789.8]	1000
	PA8332	(25) [38536.0, -765.0, 5077.6]	[1268.0, -765.0, -789.8]	1000
	PA8333	(26) [37268.0, -1585.7, 5084.0]	[0.0, -1585.7, -783.4]	1000
	PA8334	(27) [36042.0, -1202.0, 5084.0]	[-1226.0, -1202.0, -783.4]	1000
	PA8335	(28) [36101.0, 1102.0, 4721.6]	[-1167.0, 1102.0, -1145.8]	1000
	PA8336	(29) [37268.0, 1533.0, 4711.1]	[0.0, 1533.0, -1156.3]	1000
	PA8337	(30) [38550.0, 757.0, 4721.6]	[1282.0, 757.0, -1145.8]	1000
	PA8338	(31) [38550.0, -757.0, 4721.6]	[1282.0, -757.0, -1145.8]	1000
	PA8339	(32) [37268.0, -1533.0, 4711.1]	[0.0, -1533.0, -1156.3]	1000
	PA8340	(33) [36101.0, -1102.0, 4721.6]	[-1167.0, -1102.0, -1145.8]	1000
	PA8341	(34) [36532.0, 1740.0, 4898.5]	[-736.0, 1740.0, -968.9]	1000
	PA8342	(35) [36532.0, -1740.0, 4898.5]	[-736.0, -1740.0, -968.9]	1000
	PA8343	(36) [37209.2, -104.3, 4345.9]	[-58.8, -104.3, -1521.5]	1000
	PA8344	(37) [37389.4, 0.0, 4344.3]	[121.4, 0.0, -1523.1]	1000
	PA8345	(38) [37209.2, 104.3, 4345.9]	[-58.8, 104.3, -1521.5]	1000
	PA8346	(57) [37270.2, 0.0, 3863.2]	[2.2, 0.0, -2004.2]	1000
	PA8347	(55) [38958.7, 607.0, 5922.8]	[1690.7, 607.0, 55.4]	1000
	PA8348	(56) [38913.7, 607.0, 5922.0]	[1645.7, 607.0, 54.6]	1000
	PA8349	(19) [37268.0, 0.0, 8014.4]	[0.0, 0.0, 2147.0]	1000
	PA8350	(20) [37268.0, 0.0, 7715.5]	[0.0, 0.0, 1848.1]	1000
	PA8351	(39) [36278.0, 1371.0, 7023.4]	[-990.0, 1371.0, 1156.0]	1000
	PA8352	(40) [38496.0, 1070.0, 7023.4]	[1228.0, 1070.0, 1156.0]	1000
	PA8353	(41) [38496.0, -1070.0, 7023.4]	[1228.0, -1070.0, 1156.0]	1000
	PA8354	(42) [36278.0, -1371.0, 7023.4]	[-990.0, -1371.0, 1156.0]	1000
	PA8355	(43) [38258.0, 1371.0, 6817.4]	[990.0, 1371.0, 950.0]	1000
PA8356	(44) [38500.0, 1070.0, 6817.4]	[1232.0, 1070.0, 950.0]	1000	

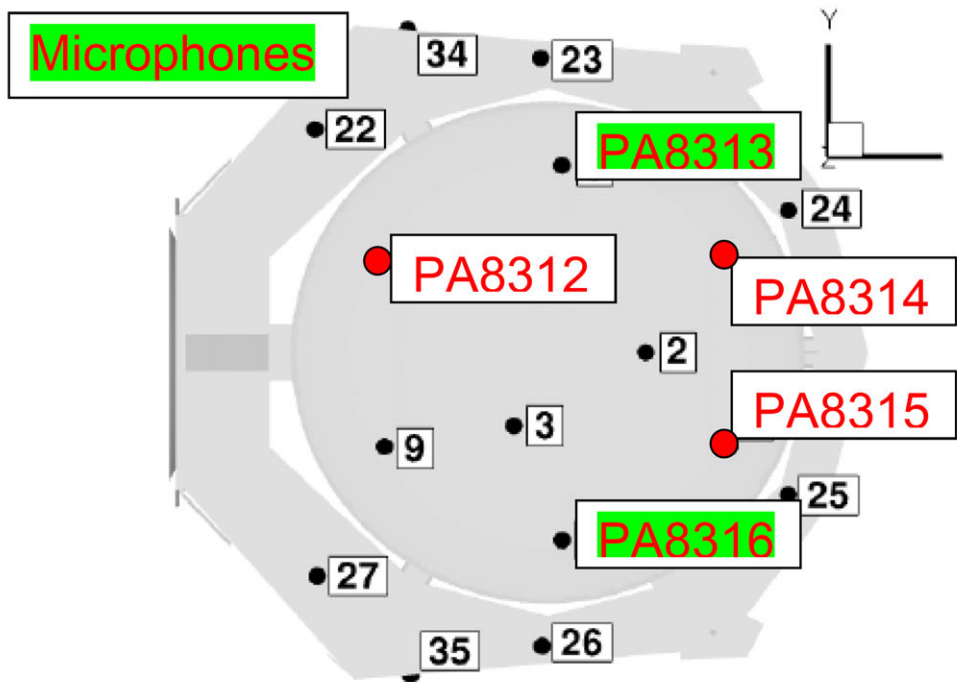


Table B.2.: Sensor List (continued)

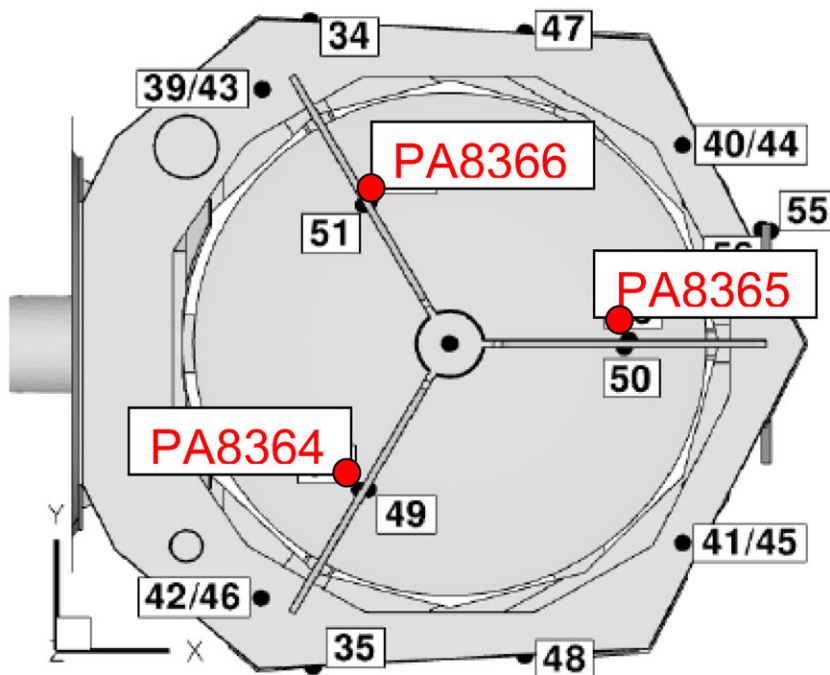
	Sensor ID		$(x_{abs}, y_{abs}, z_{abs})$ [mm, mm, mm]	$(x_{rel}, y_{rel}, z_{rel})$ [mm, mm, mm]	$f_s$ [Hz]
	PA8357	(45)	[38500.0, -1070.0, 6817.4]	[1232.0, -1070.0, 950.0]	1000
	PA8358	(46)	[38258.0, -1371.0, 6817.4]	[990.0, -1371.0, 950.0]	1000
	PA8359	(47)	[37664.0, 1676.3, 6535.0]	[396.0, 1676.3, 667.6]	1000
	PA8360	(48)	[37664.0, -1676.3, 6535.0]	[396.0, -1676.3, 667.6]	1000
	PA8367	(58)	[35277.0, 0.0, 7093.7]	[-1991.0, 0.0, 1226.3]	1000
	PA8368	(59)	[39038.1, 0.0, 7023.4]	[1770.1, 0.0, 1156.0]	1000
	PA8369	(60)	[35829.8, 0.0, 5565.9]	[-1438.2, 0.0, -301.5]	1000
<b>TA Spiderarms</b>	PA8361	(49)	[36823.7, -807.9, 7513.0]	[-444.3, -807.9, 1645.6]	1000
	PA8362	(50)	[38190.9, -19.0, 7513.0]	[922.9, -19.0, 1645.6]	1000
	PA8363	(51)	[36790.8, 788.9, 7513.0]	[-477.2, 788.9, 1645.6]	1000
	PA8364	(52)	[36790.4, -789.6, 7513.0]	[-477.6, -789.6, 1645.6]	1000
	PA8365	(53)	[38190.1, 19.0, 7513.0]	[922.1, 19.0, 1645.6]	1000
	PA8366	(54)	[36823.3, 808.6, 7513.0]	[-444.7, 808.6, 1645.6]	1000
<b>TA Suncover</b>	PA8309	(1)	[37040.0, 395.0, 4976.0]	[-228.0, 395.0, -891.4]	1000
	PA8310	(2)	[37734.0, 0.0, 4982.2]	[466.0, 0.0, -885.2]	1000
	PA8311	(3)	[37040.0, -395.0, 4976.1]	[-228.0, -395.0, -891.3]	1000
	PA8312	(4)	[36354.0, 508.0, 5039.2]	[-914.0, 508.0, -828.2]	1000
	PA8313M	(5)	[37268.0, 1009.0, 5040.8]	[0.0, 1009.0, -826.6]	1000
	PA8314	(6)	[38182.0, 508.0, 5053.2]	[914.0, 508.0, -814.2]	1000
	PA8315	(7)	[38182.0, -508.0, 5052.7]	[914.0, -508.0, -814.7]	1000
	PA8316M	(8)	[37268.0, -1009.0, 5041.4]	[0.0, -1009.0, -826.0]	1000
	PA8317	(9)	[36354.0, -508.0, 5038.9]	[-914.0, -508.0, -828.5]	1000
PA8318	(61)	[36540.0, 0.0, 5002.6]	[-728.0, 0.0, -864.8]	1000	
<b>URD External</b>	PA8001		n/a	n/a	2000
	PA8002		n/a	n/a	2000
	PA8003		n/a	n/a	2000
	PA8004		n/a	n/a	2000
	PA8005		n/a	n/a	2000
	PA8006		n/a	n/a	500
	PA8007		n/a	n/a	500
	PA8008		n/a	n/a	500
	PA8009		n/a	n/a	500
	PA8010		n/a	n/a	500
	PA8011		n/a	n/a	500
	PA8012		n/a	n/a	500
	PA8013		n/a	n/a	500
	PA8014		n/a	n/a	500
	PA8015		n/a	n/a	500
	PA8016		n/a	n/a	500
	PA8017		n/a	n/a	500
	PA8018		n/a	n/a	500
	PA8019		n/a	n/a	500
	PA8020		n/a	n/a	500
	PA8021		n/a	n/a	500

**Table B.2.:** Sensor List (continued)

	<b>Sensor ID</b>	$(x_{abs}, y_{abs}, z_{abs})$ [mm, mm, mm]	$(x_{rel}, y_{rel}, z_{rel})$ [mm, mm, mm]	$f_s$ [Hz]
	PA8022	n/a	n/a	500
	PA8023	n/a	n/a	500
	PA8024	n/a	n/a	500
	PA8025	n/a	n/a	500
	PA8026	n/a	n/a	500
<b>URD</b>	PA8027	n/a	n/a	1000
<b>Internal</b>	PA8028	n/a	n/a	1000
	PA8029	n/a	n/a	1000
	PA8030	n/a	n/a	1000
	PA8031	n/a	n/a	1000
	PA8032	n/a	n/a	500
	PA8033	n/a	n/a	500
	PA8034	n/a	n/a	500
	PA8035	n/a	n/a	500
	PA8036	n/a	n/a	500
	PA8037	n/a	n/a	500
	PA8038	n/a	n/a	500
	PA8039	n/a	n/a	500
	PA8040	n/a	n/a	500
	PA8041	n/a	n/a	500
	PA8042	n/a	n/a	500
	PA8043	n/a	n/a	500
	PA8044	n/a	n/a	500
	PA8045	n/a	n/a	500
	PA8046	n/a	n/a	500
	PA8047	n/a	n/a	500

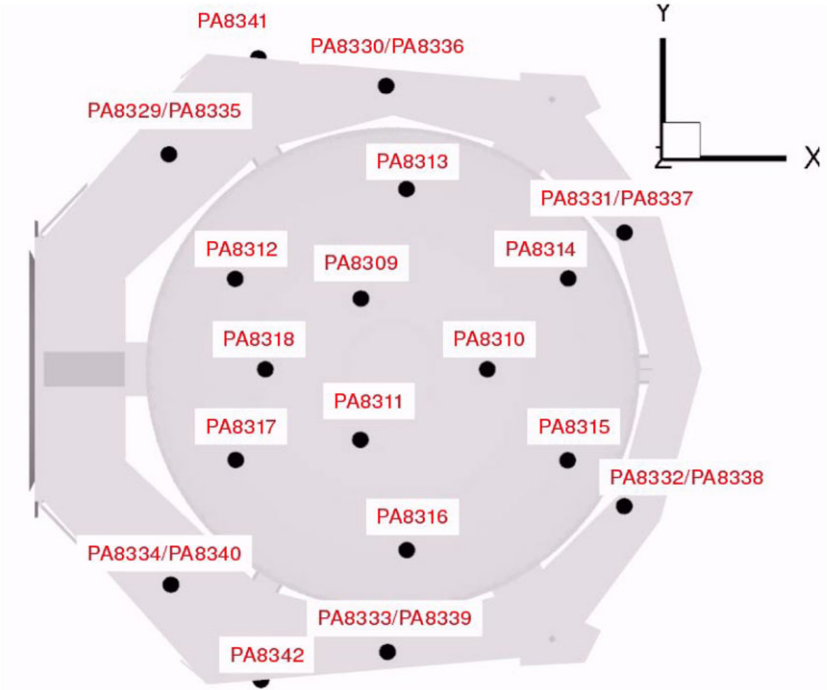


(a) TA top view on Shear Box and Suncover (less detailed). Sensor nomenclature accords to Schmid [22] (black) and the *Parameter Identification List* [18] (red). Microphones are highlighted in green.

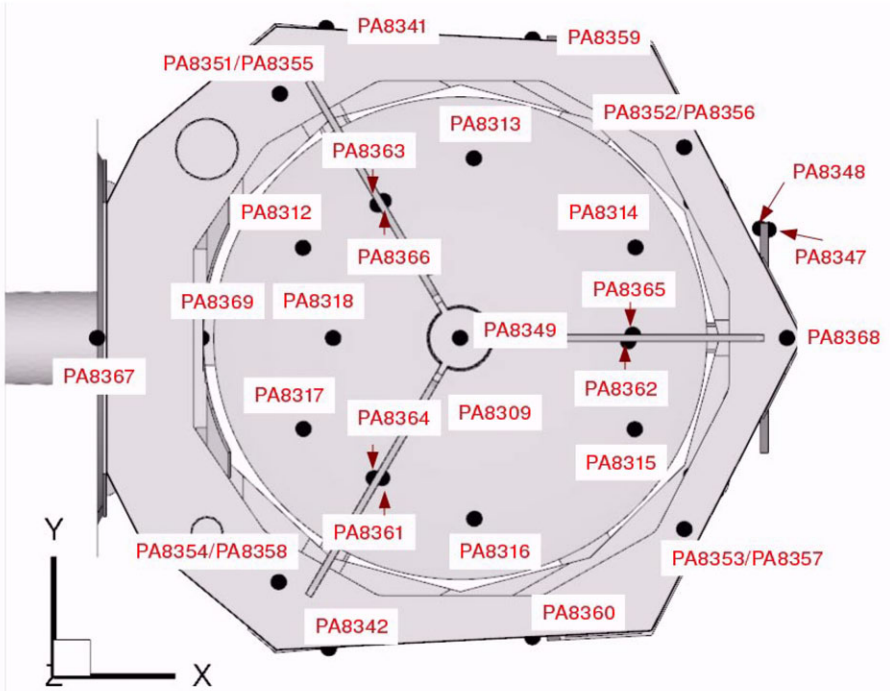


(b) TA top view (less detailed). Sensor nomenclature according to Schmid [22] (black) and the *Parameter Identification List* [18] (red).

**Figure B.1.:** Pressure sensor locations on the Telescope Assembly. All sensors feature a sampling rate of  $f_s = 1000$  Hz.  
© Schmid and Engfer [23]

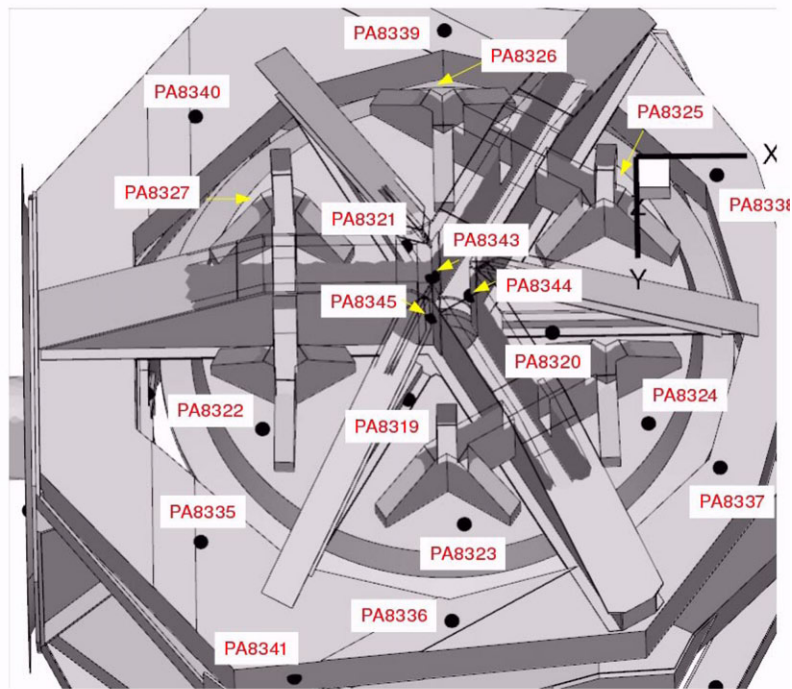


(c) TA top view on Shear Box and Primary Mirror Suncover. Sensor nomenclature according to the *Parameter Identification List* [18] (red).

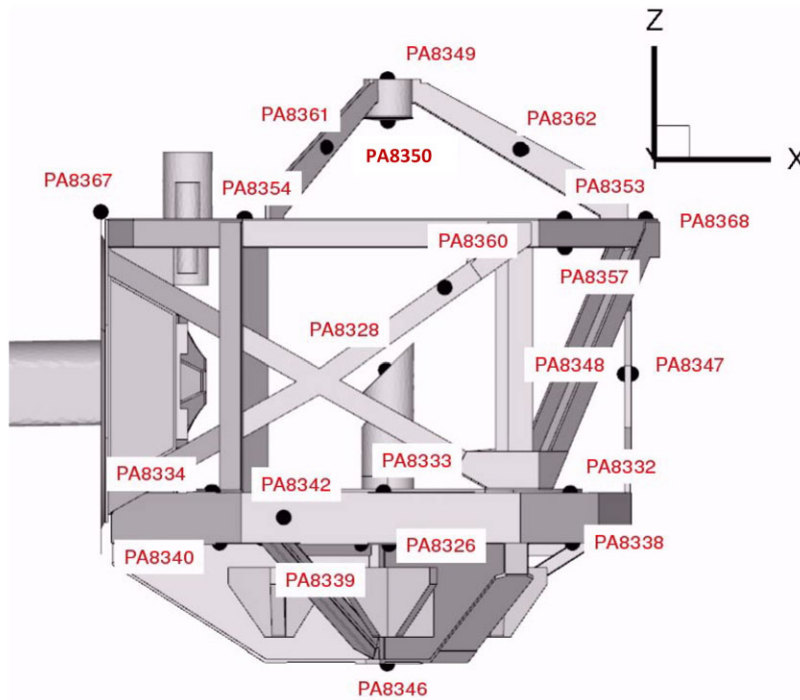


(d) TA top view. Sensor nomenclature according to the *Parameter Identification List* [18] (red).

**Figure B.1.:** Pressure sensor locations on the Telescope Assembly. All sensors feature a sampling rate of  $f_s = 1000$  Hz. © Schmid and Engfer [23]

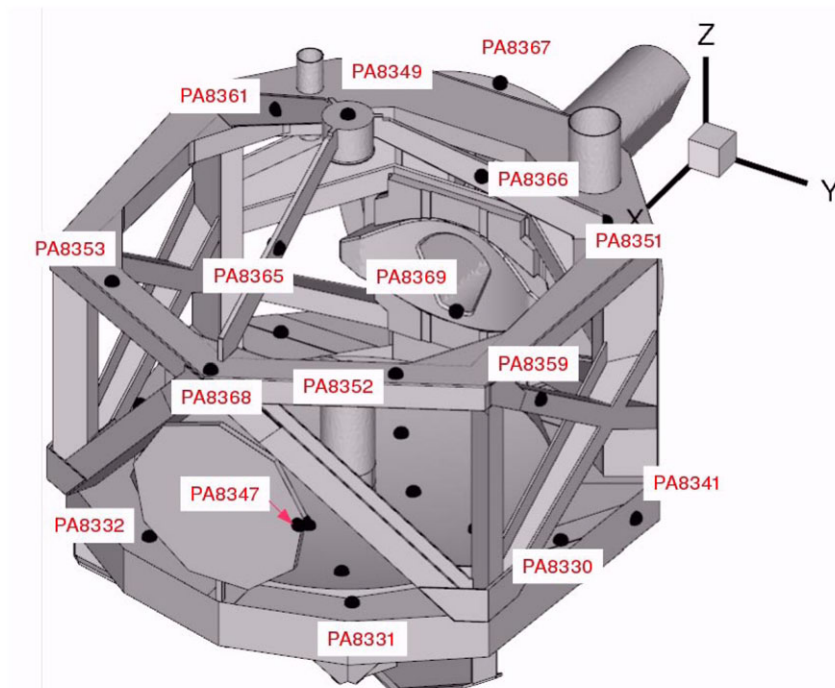


(e) TA bottom view on Primary Mirror Assembly (PMA). Sensor nomenclature according to the *Parameter Identification List* [18] (red).



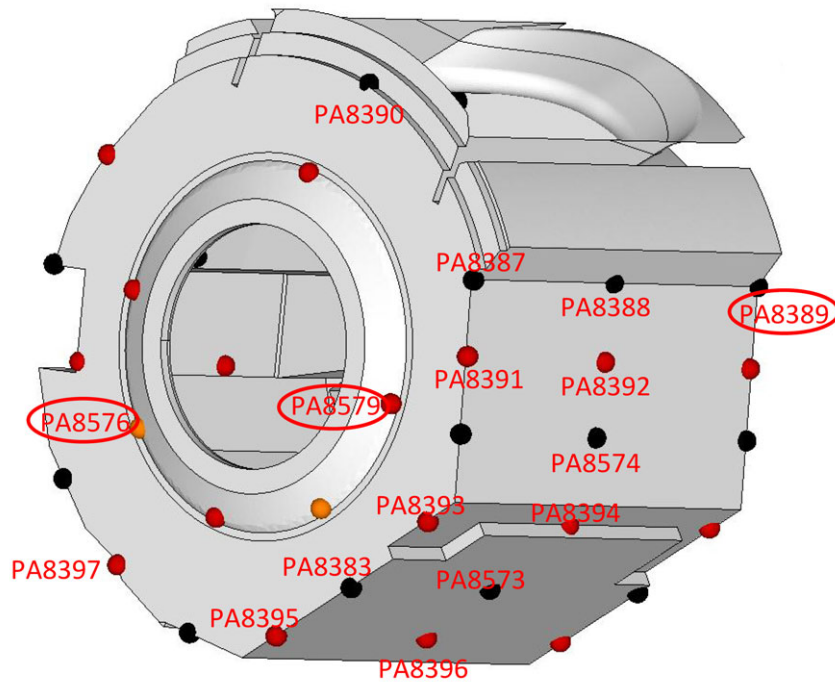
(f) TA front view. Sensor nomenclature according to the *Parameter Identification List* [18] (red).

**Figure B.1.:** Pressure sensor locations on the Telescope Assembly. All sensors feature a sampling rate of  $f_s = 1000$  Hz. © Schmid and Engfer [23]

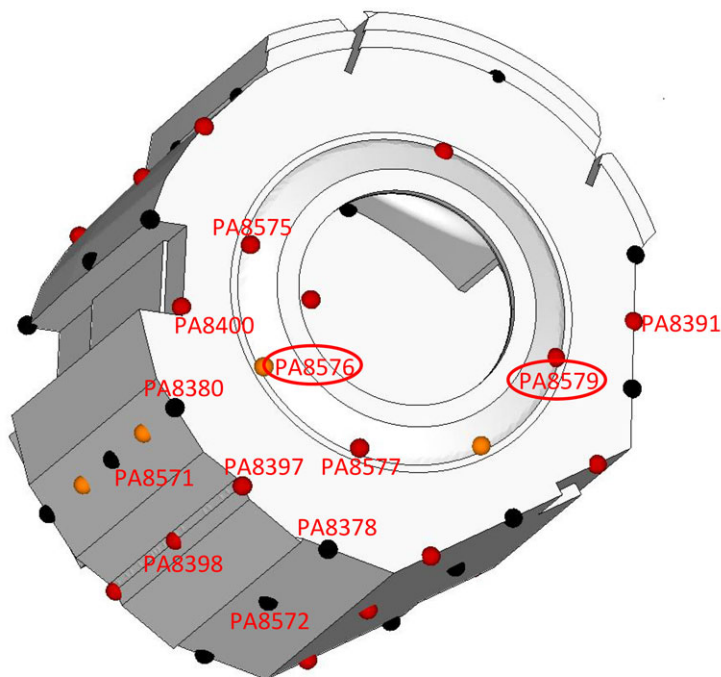


(g) TA 3D view. Sensor nomenclature according to the *Parameter Identification List* [18] (red).

**Figure B.1.:** Pressure sensor locations on the Telescope Assembly. All sensors feature a sampling rate of  $f_s = 1000$  Hz.  
© Schmid and Engfer [23]

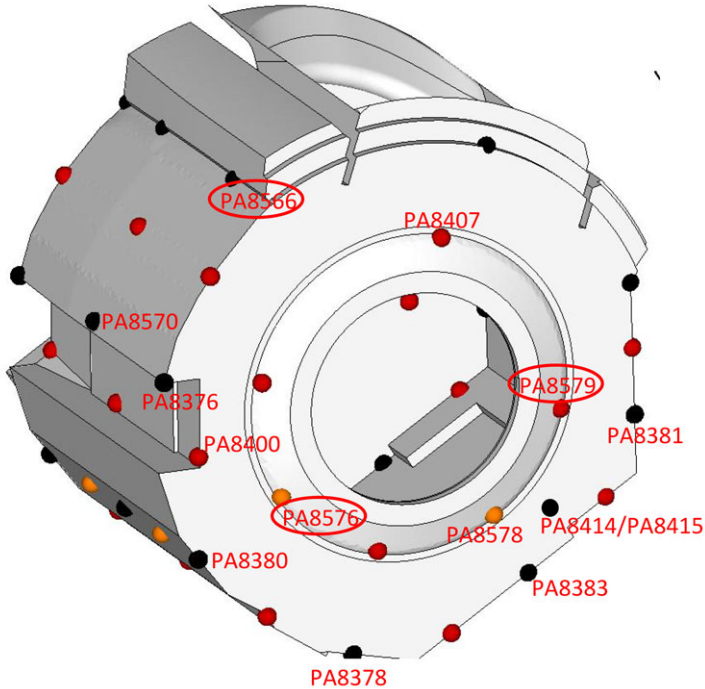


(a) Cavity 3D view № 1.

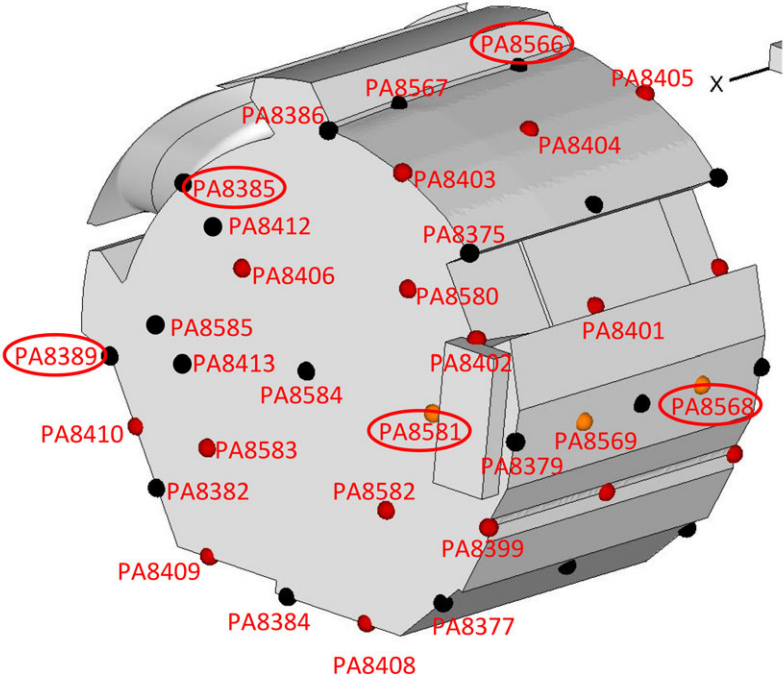


(b) Cavity 3D view № 2.

**Figure B.2.:** Pressure sensor locations on the the cavity surface. All sensors feature a sampling rate of  $f_s = 1000$  Hz.  
 © Schmid and Engfer [23]



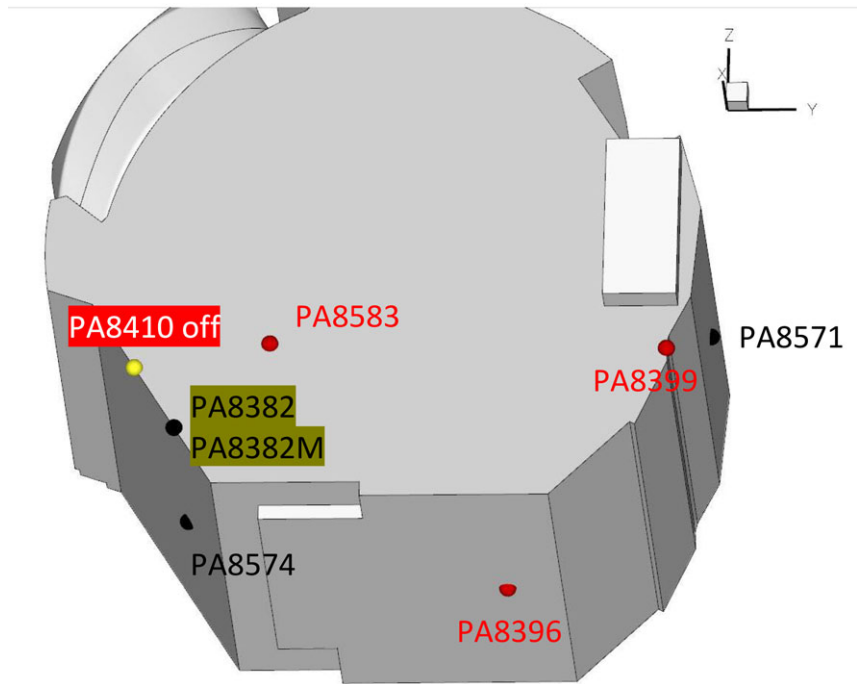
(c) Cavity 3D view № 3.



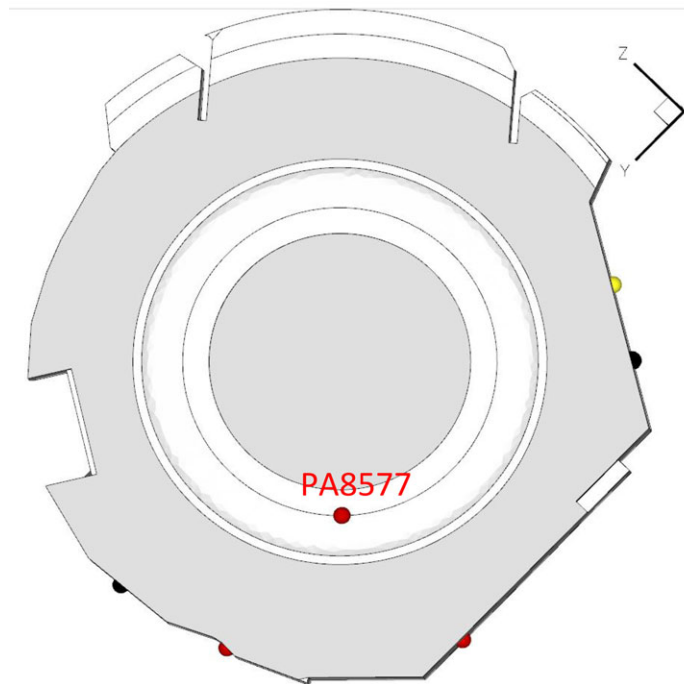
(d) Cavity 3D view № 4.

**Figure B.2.:** Pressure sensor locations on the the cavity surface. All sensors feature a sampling rate of  $f_s = 1000$  Hz. © Schmid and Engfer [23]





(e) Cavity 3D view № 5. Only microphones are displayed.



(f) Cavity side view. Only microphones are displayed.

**Figure B.2.:** Pressure sensor locations on the the cavity surface. All sensors feature a sampling rate of  $f_s = 1000$  Hz.  
© Schmid and Engfer [23]

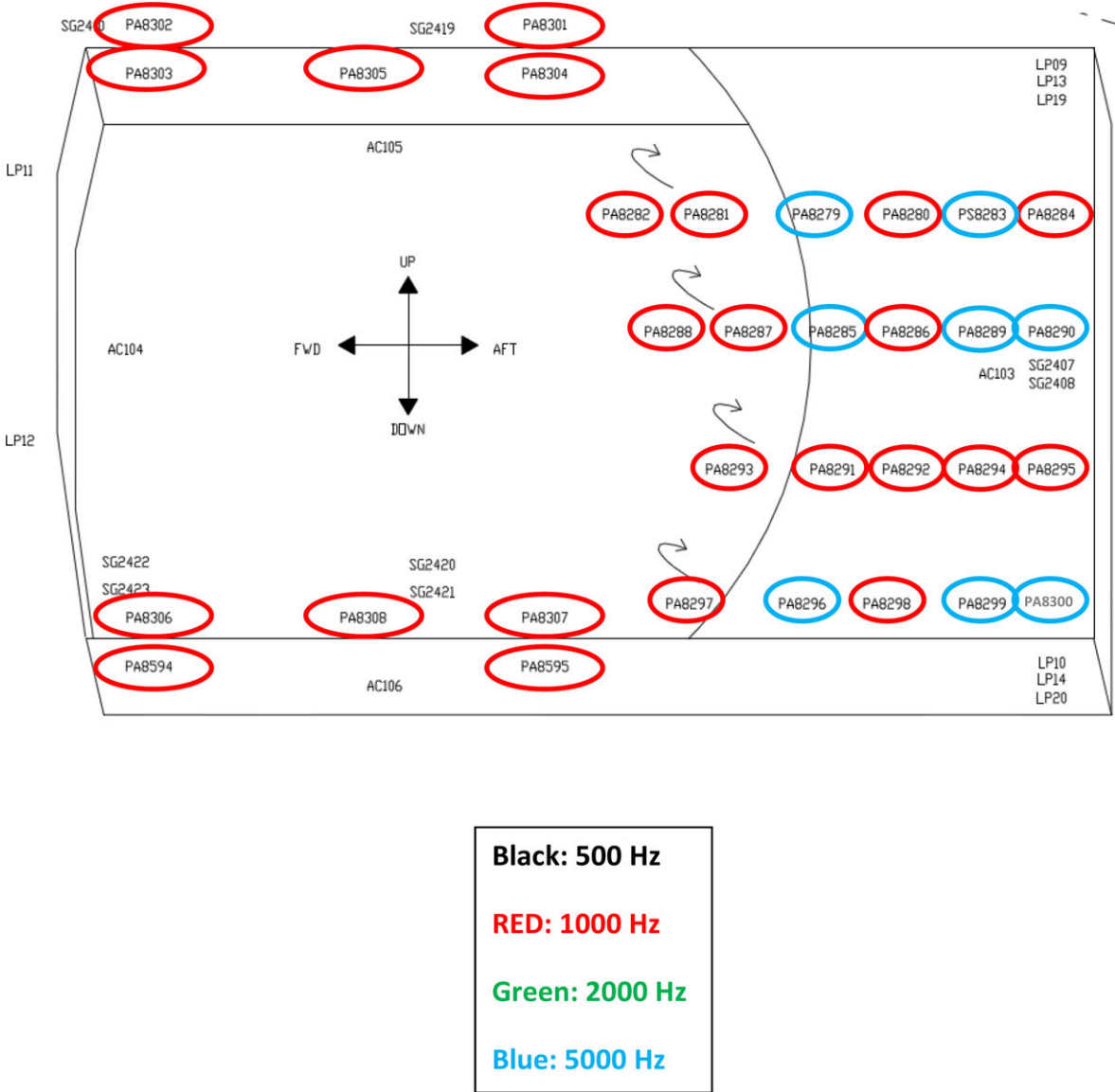


Figure B.3.: Pressure sensor locations on the Aperture Ramp and Sidewalls.

© Schmid and Engfer [23]

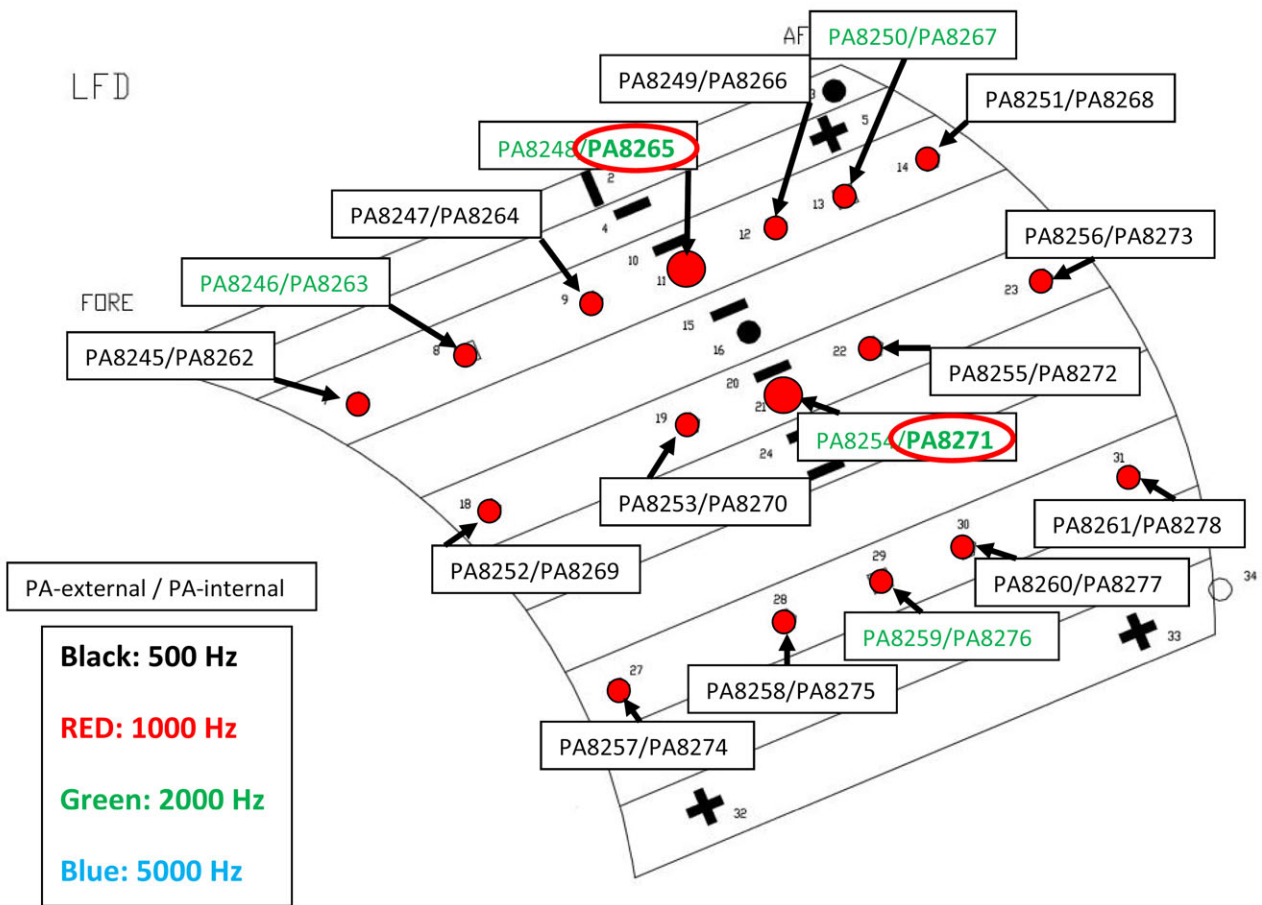


Figure B.4.: Pressure sensor locations on the Lower Flexible Door.

© Schmid and Engfer [23]

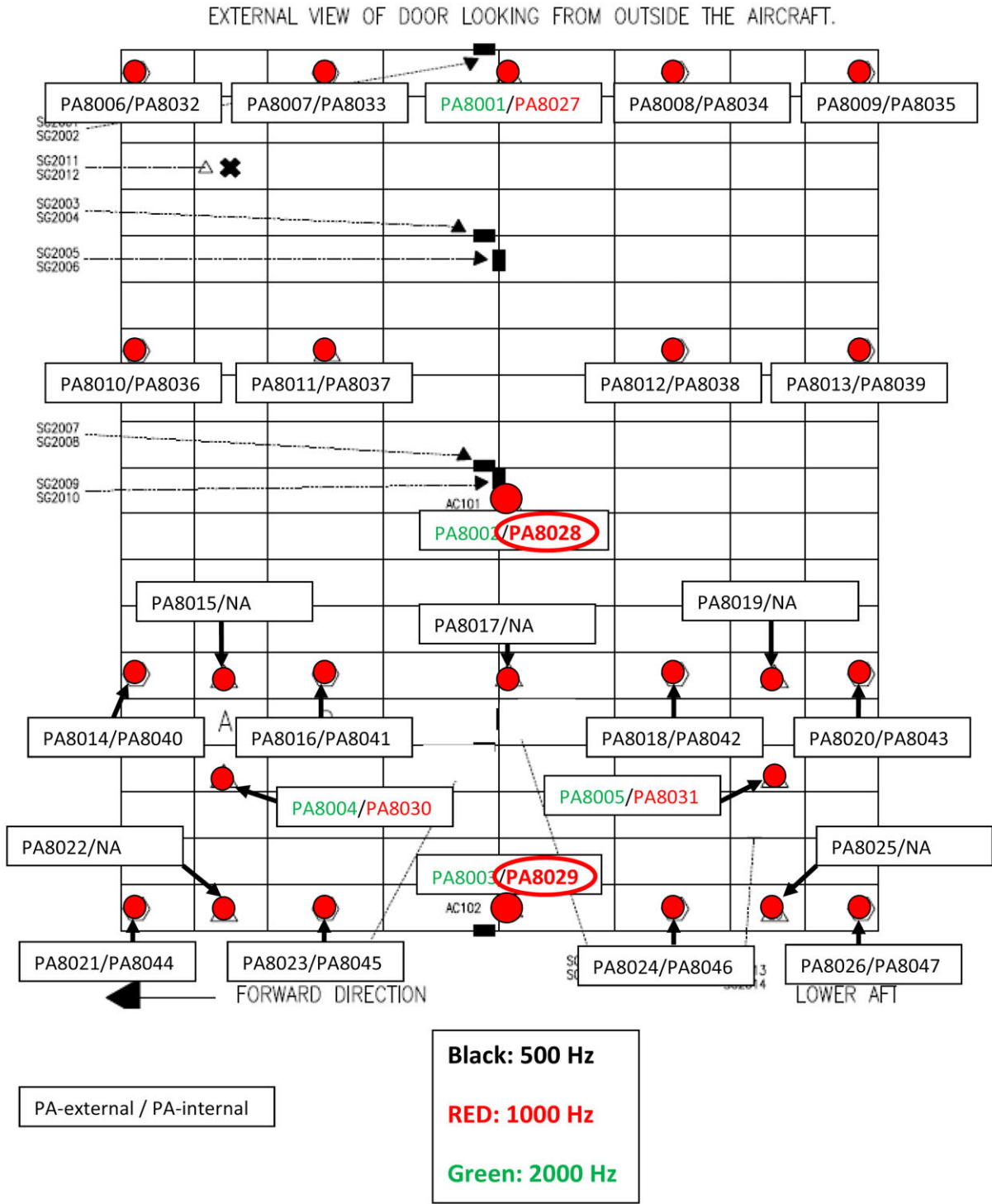
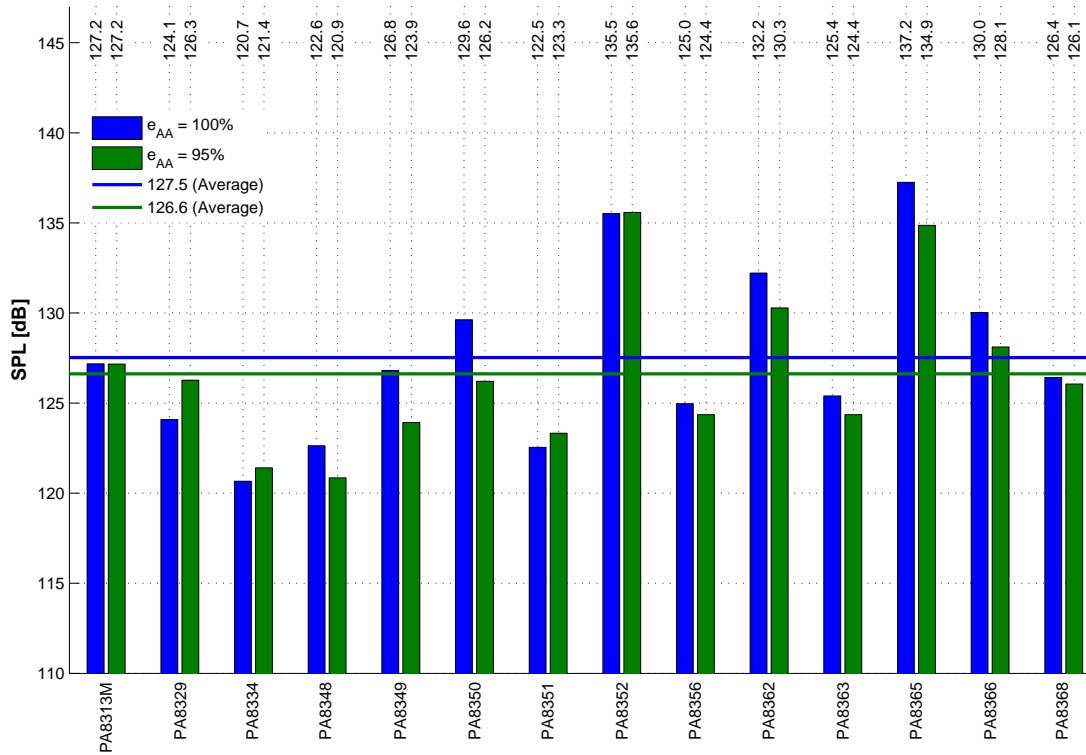


Figure B.5.: Pressure sensor locations on the Upper Rigid Door.

## C. Additional Aeroacoustic Analysis Plots



**Figure C.1.:** Comparison of the aperture exposures  $e_{AA} = 95^\circ$  and  $e_{AA} = 100^\circ$  for the TA hot spots (cp. [Figure 6.4](#) on p. 28) in baseline configuration. Due to the aperture exposure limitation (see [Chapter 3](#) on p. 7 f.), the test data set is slightly inconsistent. However, the influence of the difference between the two AA exposures does not seem to be significant. The most noticeable discrepancy occurs for the hot spots on the SMM, but this circumstance does not degrade the statements in [Chapter 6](#) (p. 21 ff.). The hot spot SPL values for an aperture exposure of  $e_{AA} = 100\%$  during a science mission can be expected to be slightly higher than the measure values for  $e_{AA} = 95\%$ . FLT033,35\_TC023,30\_AA40\_EXP95,100\_ALT35k\_Ma0.85.

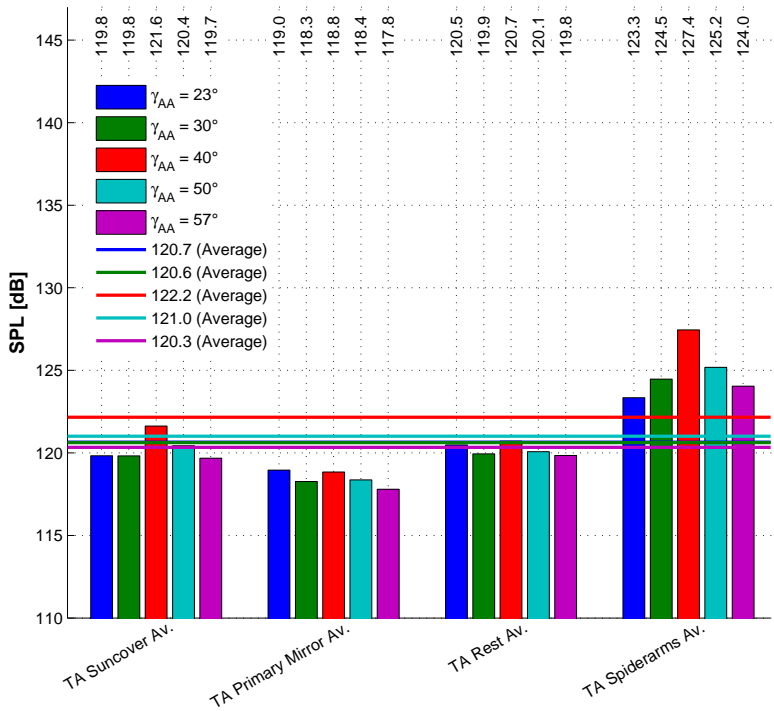
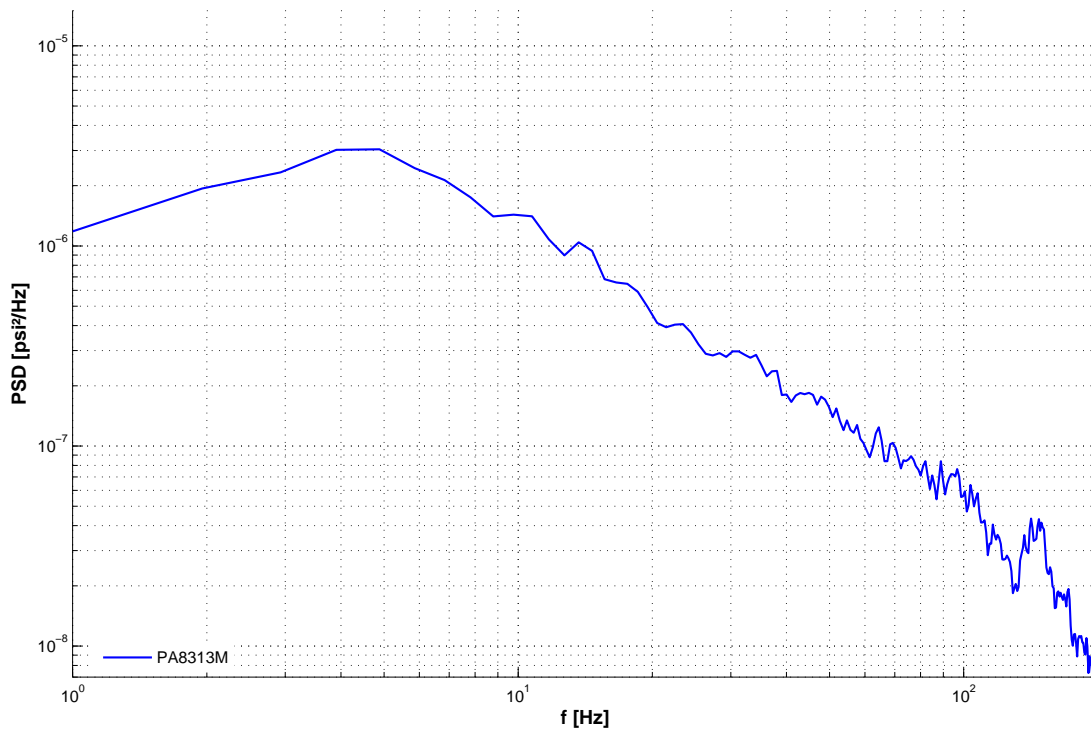
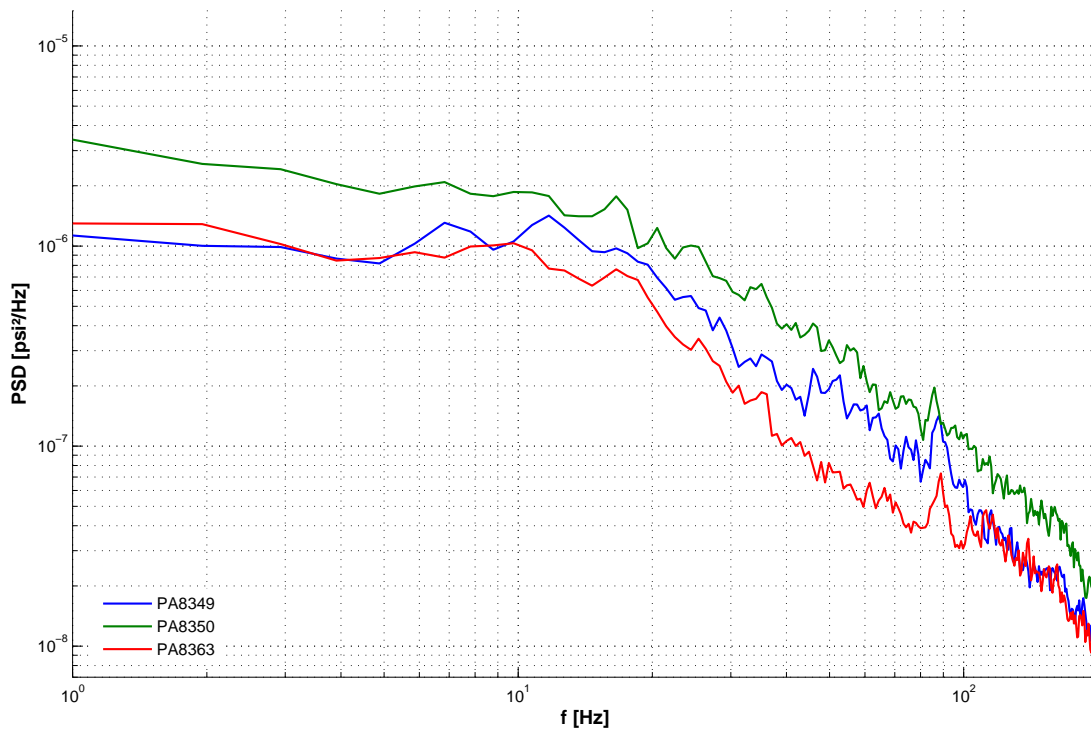


Figure C.2.: SPL plot of telescope sensor group averages for different aperture positions in baseline configuration. FLT026,35,41,41\_TC010,25,22,30\_AA40\_EXP95-100\_ALT35k\_Ma0.85.

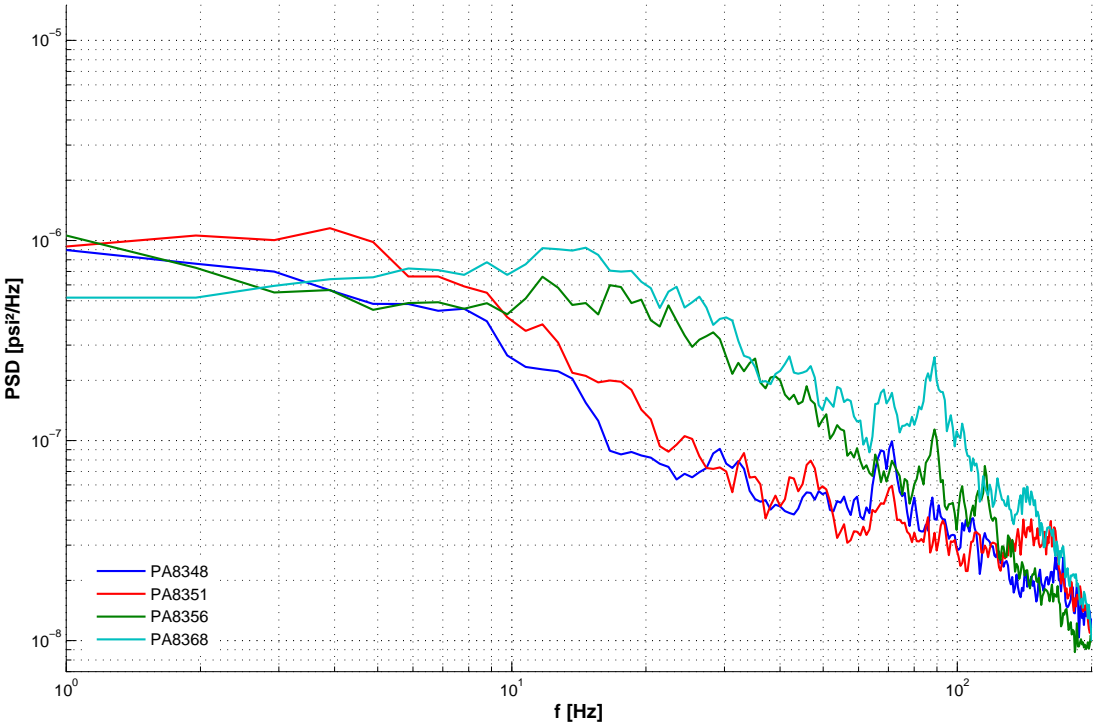


(a) Suncover sensor PA8313M featuring predominantly broadband characteristic.



(b) Sensors PA8349, -50, -63 featuring predominantly broadband characteristic.

**Figure C.3.:** PSD plot of hot spot sensors in baseline configuration with a spectral characteristics ranging between broadband (Figure 6.6.a on p. 29) and narrowband (Figure 6.6.b on p. 29).  
 FLT035\_TC030\_AA40\_TA40\_EXP100\_ALT35k\_MA0.85.



(c) Sensors PA8348, -51, -56, -68 featuring narrowband peaks.

**Figure C.3.:** PSD plot of hot spot sensors in baseline configuration with a spectral characteristic ranging between broadband (Figure 6.6.a on p. 29) and narrowband (Figure 6.6.b on p. 29).  
FLT035\_TC030\_AA40\_TA40\_EXP100\_ALT35k\_MA0.85.



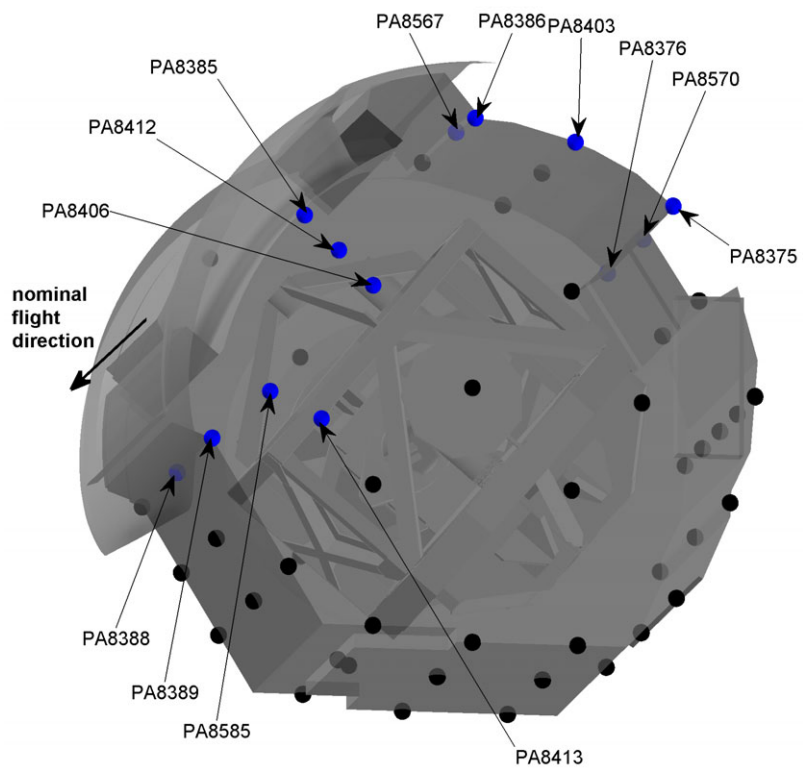
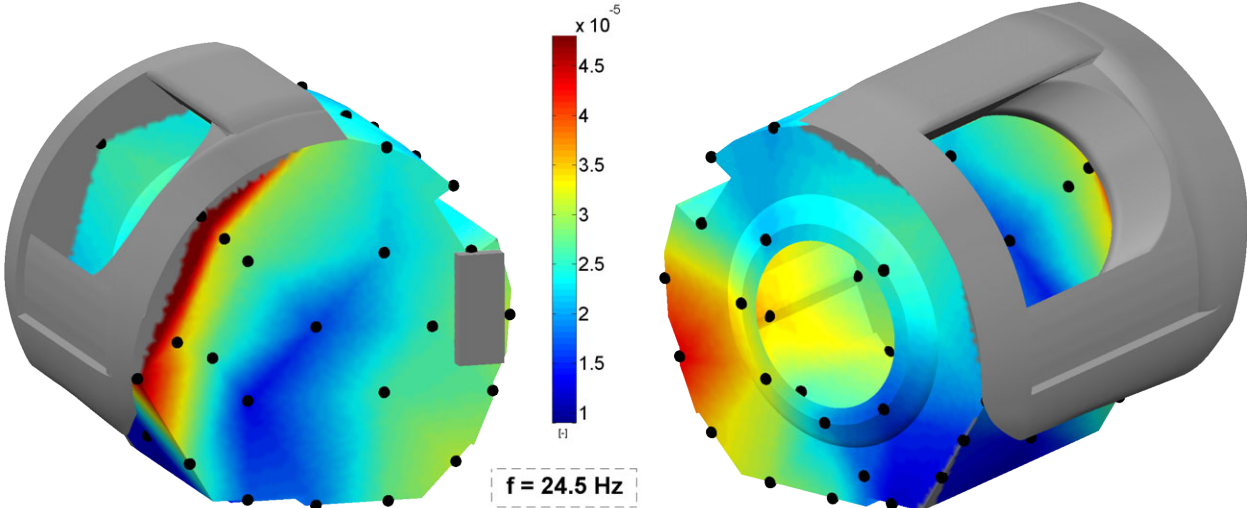
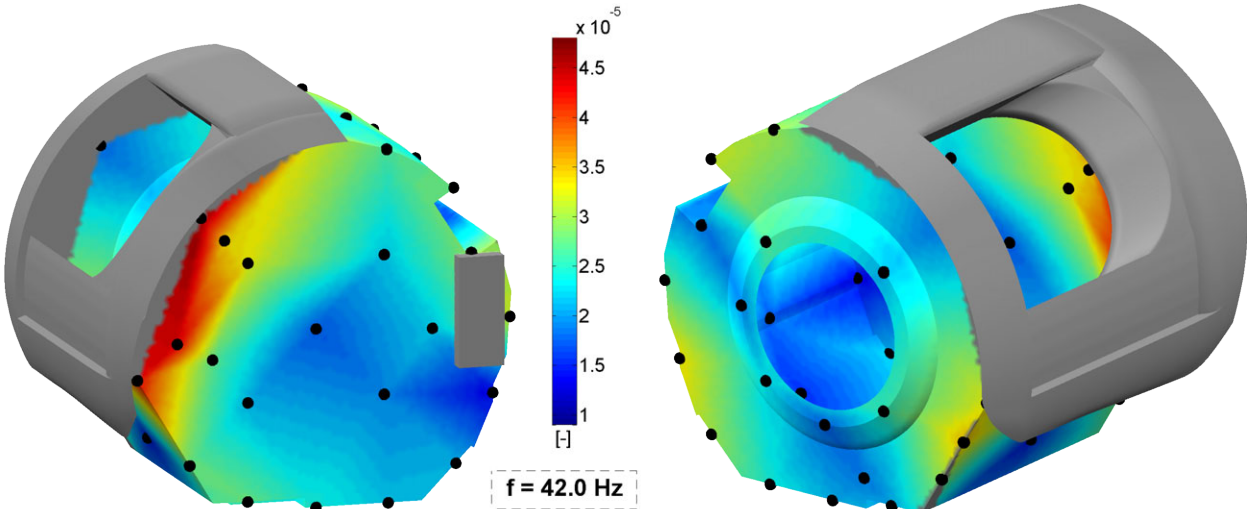


**Figure C.4.:** Overview of cavity hot spots (blue) for baseline configuration.  
 FLT026,35,35,41,41\_TC010,25,30,22,30\_AA23-57\_EXP95,100\_ALT35k\_Ma0.85.



(a) Peak at the frequency  $f = 24.5$  Hz.



(b) Peak at the frequency  $f = 42.0$  Hz.

**Figure C.5.:** Contour plot of  $c_{p,rms}$  on the cavity surface for the two acoustic peaks indicated in Figure 6.22 on p. 48. FLT033\_TC032\_AA40\_TA40\_EXP10\_ALT42k\_MA0.85.